

On Some Differences Between Wave Digital Models of Directional Couplers

Biljana P. Stošić, *Senior Member, IEEE*, Nebojša S. Dončov, *Senior Member, IEEE*,
and Marin Nedelchev

Abstract—The paper summarizes the development and applications of wave digital (WD) models for predicting the frequency response of four-port microwave passive circuits such as directional couplers. Models are developed and afterwards validated by commercial software tools. Differences between the equivalent circuit- and transmission line-based WD models are presented through analysis of multi-section couplers.

Index Terms—Directional coupler, wave digital models, equivalent circuit, transmission lines.

I. INTRODUCTION

ELECTROMAGNETIC (EM) simulation tools have become essential for circuit designers. Across industries and disciplines, simulation modeling solves real-world problems safely and efficiently and provides valuable solutions by giving clear insights into complex systems. It provides an important method of analysis which is easily verified, communicated, and understood. The designers have to be able to simulate and test their designs, and to provide accurate predictions of real-world performance of the design, before the design is fabricated in order to avoid major expenses committed to circuit construction and experimental verification.

Wave digital (WD) approach is based on A. Fettweis WD filter theory [1]-[2]. In recent years, it appears to be universal and has been successfully applied to digital modeling of a wider class of analog circuits (including microwave structures), systems and processes (including electromagnetic signals generation and radiation) [3]-[8].

On the one hand, this paper summarizes the development and applications of wave digital (WD) models for predicting the frequency response of four-port microwave passive circuits such as directional couplers. The advantage of the presented WD models is their ability to account for a wide frequency range very quickly, as well as to model different coupler geometries. Models are developed, built up in MATLAB/Simulink and afterwards validated by a commercial software tool. On the other hand, the agreement between suggested microwave device WD models is investigated.

The present paper is organized as follows. First, in Section II, an overview of WD models based on an equivalent circuit

Biljana P. Stošić and Nebojša S. Dončov are with the Faculty of Electrical Engineering, University of Niš, Aleksandra Medvedeva 14, 18000 Niš, Serbia (e-mails: biljana.stosic@elfak.ni.ac.rs, nebojsa.doncov@elfak.ni.ac.rs, ORCID: 0000-0002-4144-6506, 0000-0002-9057-6737).

Marin Nedelchev is with the Faculty of Telecommunications, Technical University of Sofia, 8 Kliment Ohridski blv, 1756 Sofia, Bulgaria (e-mail: mnedelchev@tu-sofia.bg, ORCID: 0000-0003-3926-0048).

network that have been used to simulate frequency response in different four-port microstrip structures is given. Second, in Section III, WD models based on transmission lines (TLs) for the multiport structures are described. Third, in Section IV, a list of coupler models and their simulated frequency performance is provided and compared. The covered range is from two- or tri-section couplers to tri- and five-section wideband couplers with the defected ground structures (DGS). Finally, concluding remarks are included in Section V.

II. NUTSHELL OF THE EQUIVALENT CIRCUIT-BASED WAVE DIGITAL MODELS

Over the past years, for the purpose of the application of the WD modeling method, the authors have been generated WD models of different couplers based on their equivalent circuit networks [9]-[12]. All these models have been implemented with an in-house MATLAB algorithm. Simulink environment let one drag-and-drop blocks from its library and predifine modeling elements, connect them and create complex WD models.

The equivalent circuit parameters are not quoted at the beginning, therefore the initial step in the proposed technique is to synthesize the values of inductors and capacitors based on the frequency and the characteristic impedances of the individual coupler branches. The lumped equivalent circuit model for the conventional branch-line coupler is proposed in [13]. During modeling process, i.e. model synthesis, parts of the system representing multiport networks with inductors and capacitors in the equivalent circuit are replaced with their wave digital counterpart. One sub-block in the generated WD counterpart models a specific part of coupler layout; it represents one wave digital element (WDE). The main attention in the papers [11]-[12] is focused on generating so-called basic two-dimensional symmetric and asymmetric WDEs. So, a WD model of the device under consideration is based on basic multi-port WDEs and two-port adaptors for port impedance matching. Therefore, the developed WD model will be completely characterized by its parameters: port resistances and adaptor coefficients.

III. TRANSMISSION LINE-BASED WD MODELS (DEVELOPMENT OF NEW MODELS)

A transmission line-based wave digital model of the directional coupler is derived from its circuit diagram. A starting point for creation of a WD model of the observed four-port structure is to look on that structure as a connection of several individual arms (transmission lines) as shown in [14]. Interconnection networks are used to interconnect

identified TL segments. So, a TL-based WD model is synthesized by making use of basic wave digital building blocks. The boxes in the WD model contain the arithmetic operations and represent the interconnection network or contain the delay elements corresponding to the TL models.

A. Basic Wave Digital Building Blocks

Basic building blocks in the proposed TL-based WD model are unit elements (Fig. 1), circuit elements (like resistor shown in Fig. 2) and interconnection networks (Fig. 3) [5], [15]. Therefore, we describe the wave-flow equivalents to circuit elements and interconnection networks used in WD models.

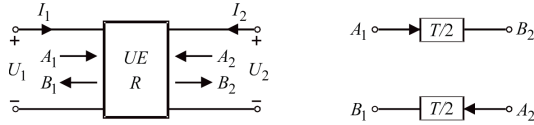


Fig. 1. Unit element and the corresponding wave-flow graph.

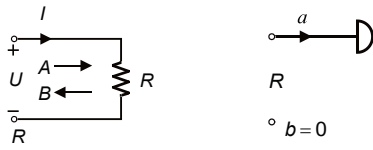


Fig. 2. Wave-flow equivalent for resistor, $Z_{in} = R$.

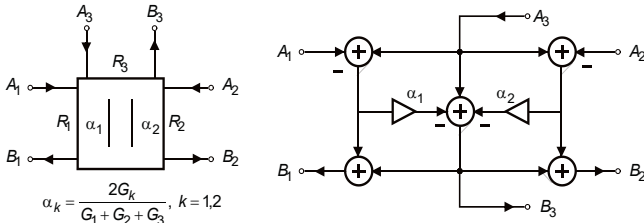


Fig. 3. Interconnection network: Three-port parallel adaptor with port 3 as the dependent port.

IV. LIST OF COUPLER MODELS (COMPARISON)

One of the most popular passive circuits used for various microwave and millimeter-wave applications is a branch-line directional coupler. In this section, digital models of several coupler structures are presented and discussed. Simple wave digital models are generated and simulated by use of MATLAB/Simulink environment. Also, the commercial Keysight Pathwave Advanced Design System (ADS) simulation software is used to generate ideal TL models of the designed couplers for comparison purposes.

To investigate the validity of the described WD models, comparison of the magnitude performance is given. The results of the illustrated examples in the frequency domain are presented here. The covered example range is from two- and tri-section couplers to tri- and five-section wideband couplers with DGS structures.

B. Case 1: A Single-Band Two-Section Coupler

The simplest coupler structure is composed of four quarter-wavelength transmission lines with different impedances. One such structure, i.e. a symmetric single-band coupler, which circuit diagram is shown in Fig. 4, with characteristic

impedance of the main line $Z_1 = Z_0 / \sqrt{2}$, and for the branch line $Z_2 = Z_0 = 50 \Omega$, is observed in [9], [12]. The electrical lengths of the TL segments are $\theta = \pi/2$. The operating frequency is 2.45 GHz. Its model in ADS based on ideal transmission line is shown in [12]. That paper contains also its equivalent circuit-based WD model described in detail.

TL-based WD model is shown in Fig. 5 together with adaptor coefficients putted in Table I. Delays of all TLs are equal because of their equal electrical lengths and amounts to 102 ps. Simulated magnitudes are compared in Fig. 6. The comparison shows a coincidence between the S-parameter results obtained by EC-based WDM, TL-based WDM and ideal ADS model.

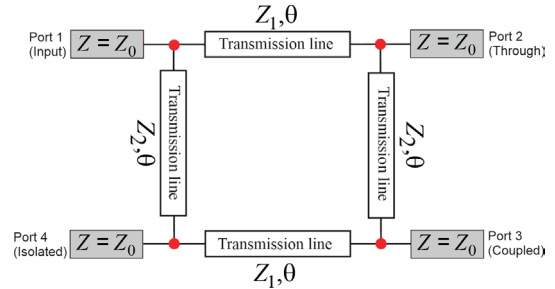


Fig. 4. Circuit diagram of a single-band two-section directional coupler. (Red dots show the locations of three-port parallel adaptors in the WD model).

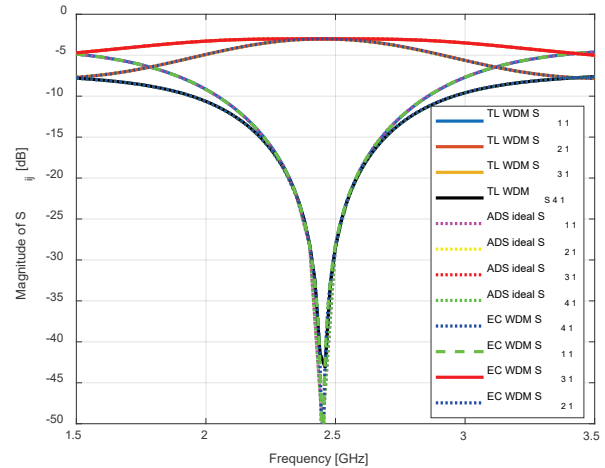


Fig. 6. Simulated magnitude performance of a single-band two-section coupler (TL-based WDM versus EC-based WDM and ADS ideal TL model).

TABLE I
PORT SIGNAL ORDERING FOR INTERCONNECTION NETWORKS

Three-port adaptors	Port 1	Port 2	Coeff. α_1	Coeff. α_2
ADP-Z0Z1Z2	Z0	Z1	$\alpha_1=2/Z_0/SG$	$\alpha_2=2/Z_1/SG$
			$SG=1/Z_0+1/Z_1+1/Z_2$	
ADP-Z1Z0Z2	Z1	Z0	$\alpha_1=2/Z_1/SG$	$\alpha_2=2/Z_0/SG$
Two-port adaptors	Port 1	Port 2	Coefficient α	
ADP-S	Rg	Z0	$(Rg-Z_0)/(Rg+Z_0)$	
ADP-L	Z0	RL	$(Z_0-RL)/(Z_0+RL)$	

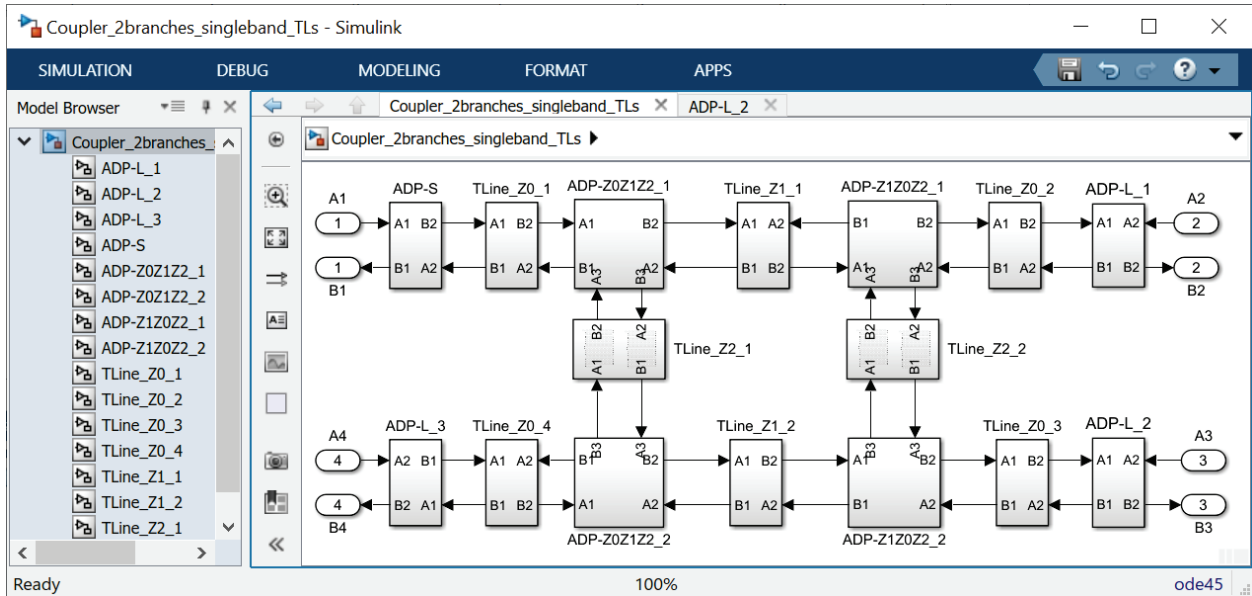


Fig. 5. Simulink model of TL-based WDM of a single-band two-section coupler.

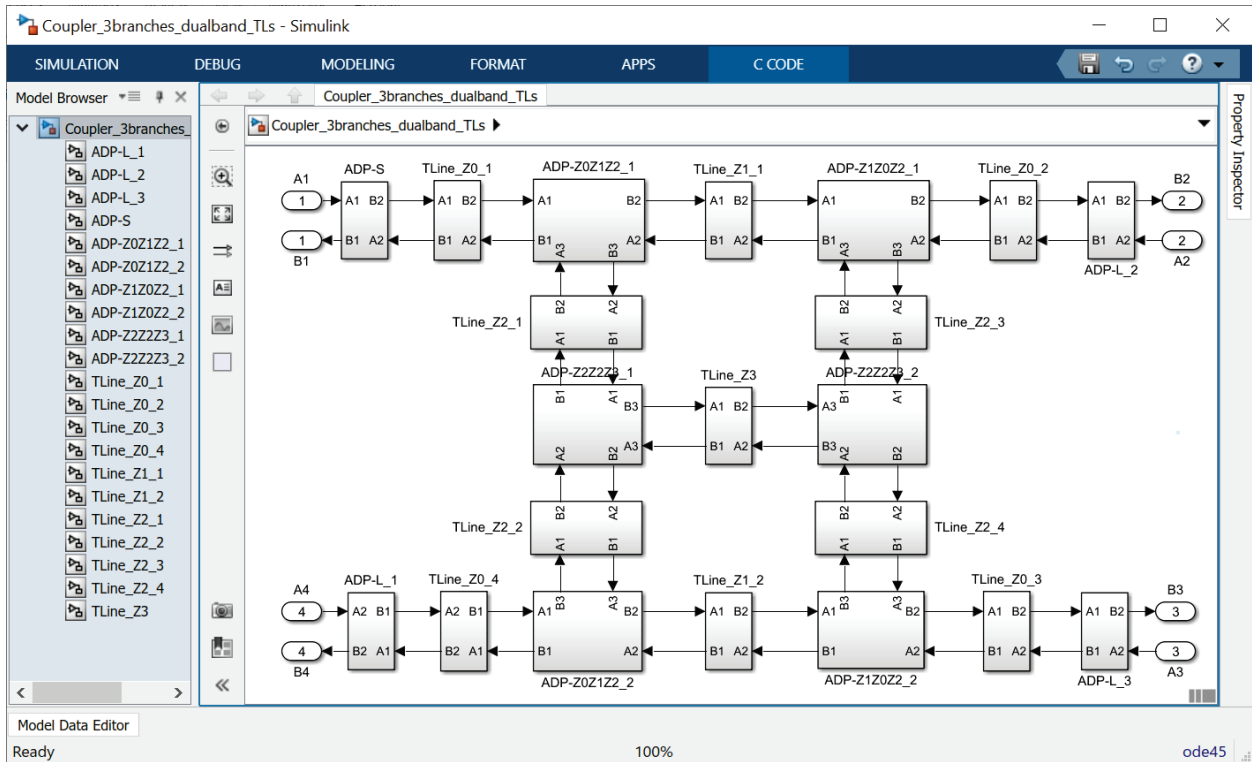


Fig. 8. TL-based WDM of a dual-band tri-section coupler.

C. Case 2: A Dual-Band Tri-Section Coupler

A dual-band branch-line coupler structure with three parallel lines which schematic diagram can be found in Fig. 7 is analyzed in [12]. It is design to operate at 1.0/2.5 GHz. For the characteristic impedance Z_0 set to 50Ω , the calculated line impedances are $Z_1 = 49.48 \Omega$, $Z_2 = 79.21 \Omega$, and $Z_3 = 132.66 \Omega$ having the power ratio of 3dB. This example is specific, because of different electrical lengths of transmission lines, $\theta = 51.43^\circ$ and 2θ .

TL-based model of this structure is shown in Fig. 8. The blocks corresponding to individual TLs are assigned as $TLine_Z_x$ ($x=0,1,2,3$). Delay of the corresponding TLs with the electrical length θ is 143 ps, and for 2θ is 286 ps at the frequency of 1 GHz. Ordering of port signals for used interconnection networks (two- and three-port parallel adaptors) and relations for multiplier coefficients are presented in Table I. Additional adaptor ADP-Z2Z2Z3 has two equal multiplier coefficients $\alpha_1 = \alpha_2 = (2/Z_2)/SG$, where $SG = 2/Z_2 + 1/Z_3$.

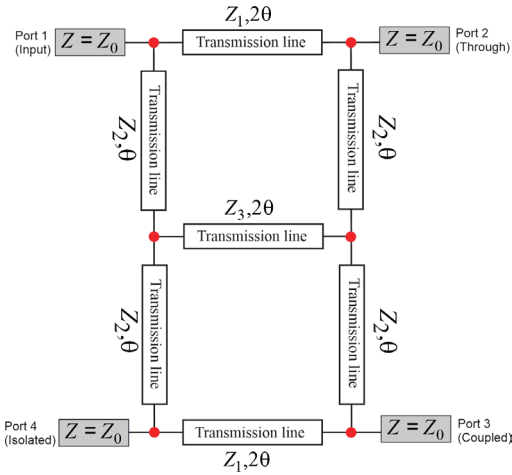


Fig. 7. Circuit diagram of a dual-band tri-section coupler. (Red dots show the locations of three-port parallel adaptors in the WD model).

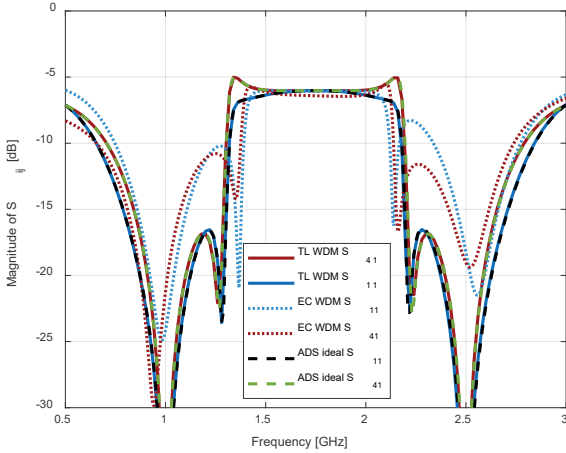


Fig. 9. Comparison of the simulated magnitudes of S_{11} and S_{41} parameters.

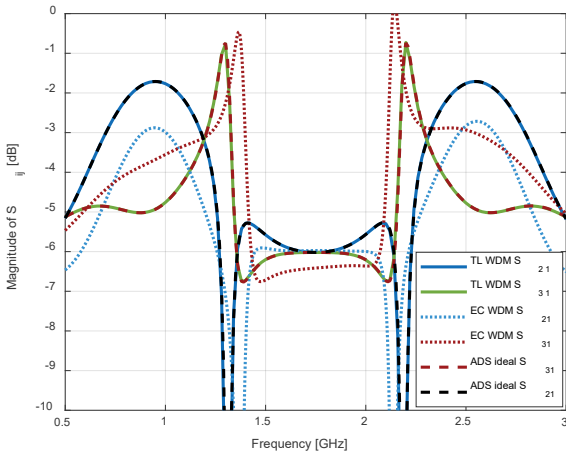


Fig. 10. Comparison of the simulated magnitudes of S_{21} and S_{31} parameters.

Comparison of simulated magnitudes of the S -parameters obtained by WD models (EC-based and TL-based) and ADS model are given in Figs. 9 and 10. TL-based model curves from MATLAB and ADS are barely distinguishable. There is a slight disagreement with results from EC-based model.

D. Case 3: A Tri-Section Wideband DGS Coupler

An example of a tri-section wideband branch-line hybrid for operating at center frequency of 2.4 GHz has been design and fabricated by authors in [10]. The characteristic

impedances of the stubs are $Z_s = 99.86\Omega$, $Z_{s1} = 41.13\Omega$ and the main line impedance is $Z_1 = 34.74\Omega$. All TLs are $\lambda/4$ long (λ is the wavelength at the operating frequency). Their delays are calculated as 104 ps. Fig. 11 contains layout of DGS coupler and Fig. 12 its circuit diagram.

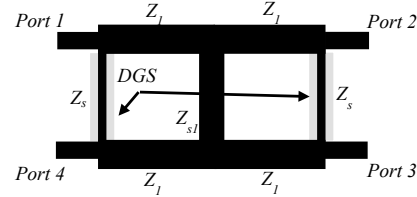


Fig. 11. Layout of a tri-section wideband DGS hybrid designed in [10].

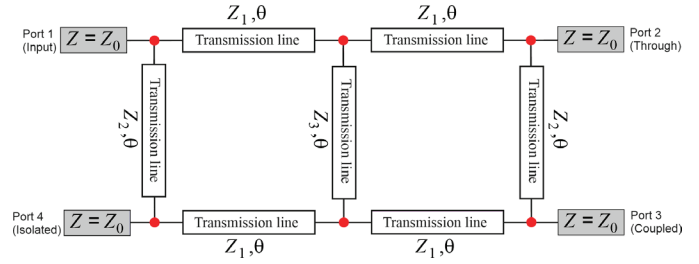


Fig. 12. Circuit diagram of a tri-section wideband DGS hybrid. (Red dots show the locations of three-port parallel adaptors in the WD model).

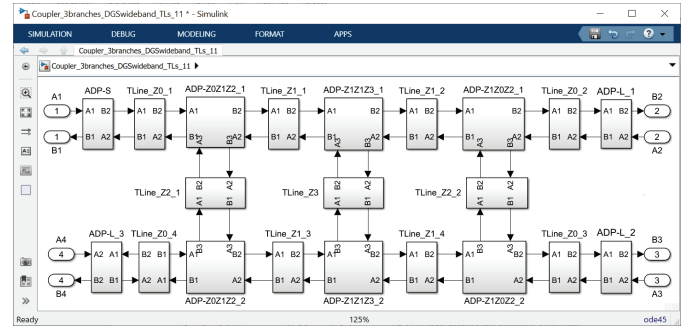


Fig. 13. TL-based WDM of a DGS wideband tri-section coupler.

Coefficient relations in three-port parallel adaptors used as interconnection networks in TL-based WDM drawn in Fig. 13 are presented in Table I. Additional adaptor ADP-Z1Z1Z3 has the multiplier coefficients with equal value calculated by relation $\alpha_1 = \alpha_2 = (2 / Z_1) / SG$, where $SG = 2 / Z_1 + 1 / Z_3$.

The simulated magnitude responses of this coupler example are compared in Fig. 14. Slight disagreement between EC-based model and other models is evident. The corresponding equivalent circuit-based model is validated by measurements and full-wave simulation results in [10].

E. Case 4: A Five-Section Wideband DGS Coupler

Different aspects of five-section wideband 3 dB branch-line hybrid with 90° phase difference which operates at center frequency of 2.5 GHz are presented in [11]. The proposed hybrid configuration, shown in Fig. 15, having symmetric nature with defected ground structures is designed and fabricated. The hybrid is also simulated and measured, and its wave digital model based on multimethod technique and an equivalent circuit is created there.

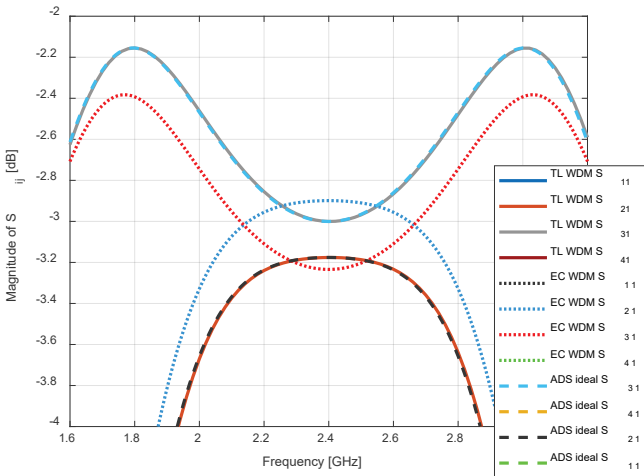
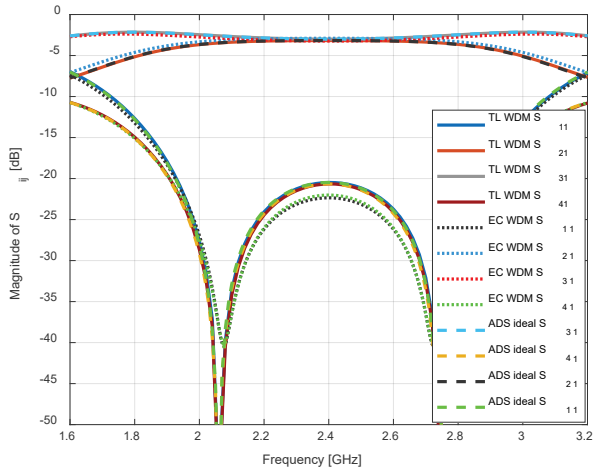


Fig. 14. Simulated magnitude performances of a tri-section wideband DGS coupler (TL-based WDM versus EC-based WD and ADS ideal TL models): (a) all S -parameters and (b) zoom on S_{21} and S_{31} parameters.

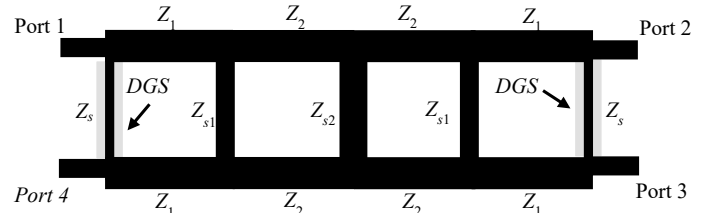


Fig. 15. Layout of a five-section wideband DGS hybrid designed in [11].

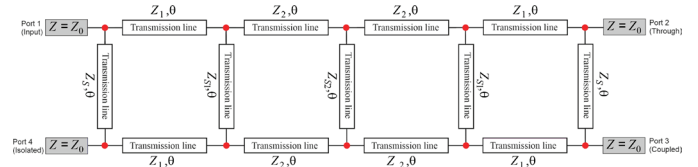


Fig. 16. Circuit diagram of a five-section wideband DGS hybrid. (Red dots show the locations of three-port parallel adaptors in the WD model).

TABLE II
PORT SIGNAL ORDERING FOR THREE-PORT ADAPTORS

Three-port adaptors	Port 1	Port 2	Coeff. α_1	Coeff. α_2
ADP-Z0Z1Zs	Z0	Z1	$\alpha_1=2/Z0/SG$	$\alpha_2=2/Z1/SG$
			$SG=1/Z0+1/Z1+1/Zs$	
ADP-Z1Z0Zs	Z1	Z0	$\alpha_1=2/Z1/SG$	$\alpha_2=2/Z0/SG$
ADP-Z1Z2Zs1	Z1	Z2	$\alpha_1=2/Z1/SG$	$\alpha_2=2/Z2/SG$
			$SG=1/Z1+1/Z2+1/Zs1$	
ADP-Z2Z1Zs1	Z2	Z1	$\alpha_1=2/Z2/SG$	$\alpha_2=2/Z1/SG$
ADP-Z2Z2Zs2	Z2	Z2	$\alpha_1=\alpha_2=2/Z2/SG$	
			$SG=2/Z2+1/Zs2$	

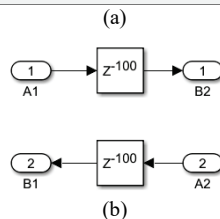
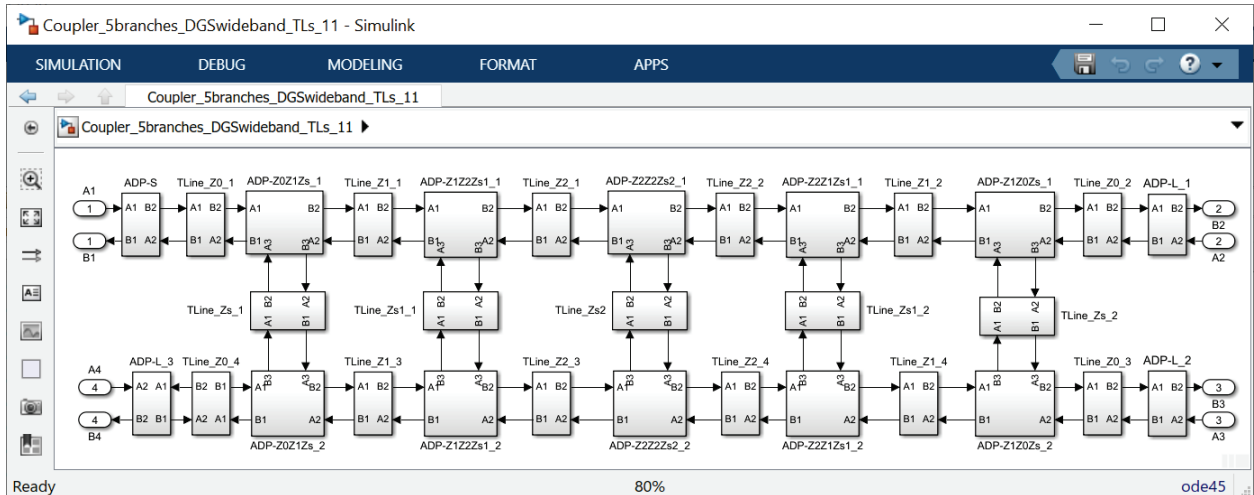


Fig. 17. (a) TL-based WDM of a five-section wideband DGS coupler and (b) model of one TL segment with used Delay block from Simulink Library.

ACKNOWLEDGMENT

This paper has been supported by project “Twinning for Enhancing Capacity and Research Excellence in Holographic Telepresence Systems as a Catalyst of Digitalization” – HOLOTWIN of the Ministry of Education and Science, Republic of Bulgaria, and by the Ministry of Education, Science and Technological Development of the Republic of Serbia.

REFERENCES

- [1] A. Fettweis, “Digital circuits and systems”, *IEEE Transactions on Circuits and Systems*, vol. CAS-31, no. 1, January, 1984, pp. 31-48.
- [2] A. Fettweis, “Wave digital filters: Theory and practice”, *Proc. IEEE*, vol. 74, 1986, pp. 270-327.
- [3] S. Bilbao, *Wave and Scattering Methods for Numerical Simulation*, Wiley, Hoboken, New Jersey, 2004.
- [4] J. A. Russer, Y. Kuznetsov, and P. Russer, “Discrete-time network and state equation methods applied to computational electromagnetics”, *Microwave Review*, vol. 16, no. 1, pp. 2-14, 2010.
- [5] B. P. Stošić and N. S. Dončov, “Combined wave digital/full-wave approach in modeling and analysis of microstrip structures with examples in MATLAB/Simulink”, Chapter 4 in book: *Advances in Engineering Research*, Nova Science Publishers, Inc., 2016, vol. 12, pp. 75-140.
- [6] P. Belforte and G. Guaschino, *DWS 9.0 Digital Wave Simulator, User’s Manual*, January 2020, doi: 10.13140/RG.2.2.11489.66407/1
- [7] P. Belforte, D. Spina, G. Antonini, L. Lombardi, and T. Dhaene, “Time-domain piecewise-linear fitting method based on digital wave processing of S-parameters”, doi: 0.13140/RG.2.2.34124.36481/2
- [8] A. Bernardini, E. Bozzo, F. Fontana, and A. Sarti, “A wave digital Newton-Raphson method for virtual analog modeling of audio circuits with multiple one-port nonlinearities”, *IEEE/ACM Transactions on Audio, Speech, and Language Processing*, doi: 10.1109/TASLP.2021.3084337
- [9] B. P. Stošić, “Comparative assessment of wave digital model of directional coupler”, 14th International Conference on Applied Electromagnetics - IIEC 2019, August 26-28, 2019, Niš, Serbia, Poster session P1-17.
- [10] M. Nedelchev, B. P. Stošić, N. Dončov, and A. Kolev, “Tri-section wideband branch-line hybrid: Design, simulation technique and measurement”, 2019 42nd International Conference on Telecommunications and Signal Processing (TSP), Hungary, Budapest, July 1-3, 2019, pp. 94-97, doi: 10.1109/TSP.2019.8768866
- [11] B. P. Stošić, M. Nedelchev, J. A. Russer, N. S. Dončov, and Z. Stanković, “Stochastic signal propagation in five-section wideband branch-line hybrid”, 2019 International Conference on Electromagnetics in Advanced Applications (ICEAA), Granada, Spain, 2019, pp. 0754-0759.
- [12] B. P. Stošić, “Wave-based digital models of different branch-line couplers”, *Serbian Journal of Electrical Engineering*, vol. 17, no. 2, June 2020, pp. 149-169, doi: 10.2298/SJEE2002149S
- [13] Y. Zhou and Y. Chen, “Lumped-element equivalent circuit models for distributed microwave directional couplers”, 2008 International Conference on Microwave and Millimeter Wave Technology, April 21 - 24, 2008.
- [14] B. P. Stošić, M. Nedelchev, and P. Belforte, “Wave digital frameworks for simulation of microwave couplers: Transmission line versus equivalent lumped circuit”, 2021 15th International Conference on Advanced Technologies, Systems and Services in Telecommunications (TELSIKS), Serbia, Niš, October 20-22, 2021, pp. 175-178, doi: 10.1109/TELSIKS52058.2021.9606374
- [15] L. Wanhammar and T. Saramaki, *Digital Filter using MATLAB*, Springer Nature Switzerland AG, 2020.

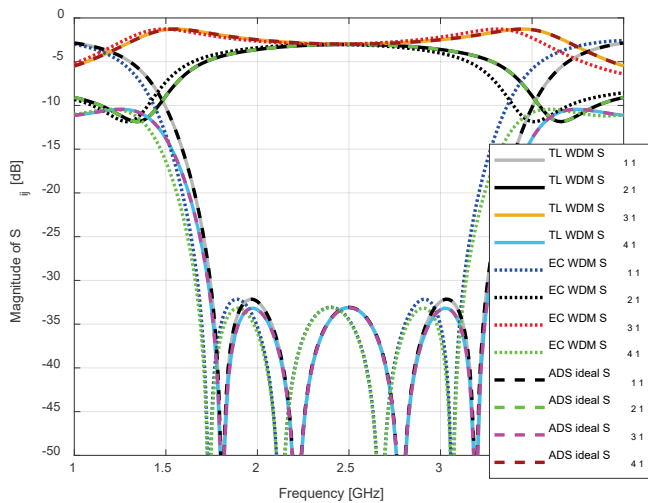


Fig. 18. Simulated magnitude performances of a five-section wideband DGS coupler (differences among TL-based WD, EC-based WD and ADS ideal TL models).

A circuit diagram of the analyzed DGS coupler is presented in Fig. 16. This circuit diagram contains some red dots which show places where three-port parallel adaptors are used in a TL-based WDM given in Fig. 17. Each TL block is presented by 100 UEs corresponding to 100 ps delay, Fig. 17b. Ordering of port signals for three-port adaptors is given in Table II.

Once again, comparison in Fig. 18 confirms matching of TL-based model results from WDM and ADS, and slight non-matching of EC-based model results. The corresponding equivalent circuit-based model is validated by measurements and full-wave simulation results in [11].

V. CONCLUSION

The paper confirms potential of a WD approach for the simulation of given directional couplers. We have investigated the differences between equivalent circuit-based and transmission line-based WD models of these four-port microwave devices. The simulations demonstrate that the proposed TL-based WD model behaves exactly the same as model generated in ADS by ideal TLs. The differences between EC-based models and abovementioned models are evident except in the case of the simplest coupler design. To conclude, there is progress, but still more to do in this WD modeling approach. The next step is to find a way to include losses in the models in order to get closer to real measurements.

On the other hand, comparing the circuit diagrams with the TL-based WDMs clearly shows their great similarity. Due to the advantages of the nature of generating the TL-based model, this approach can be easily adopted by researchers for simulation purposes of wide range of branch-line couplers. In comparison with the equivalent circuit-based modeling approach a TL-based approach is more intuitive.

Doherty PA Linearization by Injection of the 2nd order Digitally Processed Signals for 5G FBMC modulation

Aleksandar Atanasković¹, Nataša Maleš-Ilić¹, Biljana Stošić¹ and Djuradj Budimir²

Abstract – In this paper, the analysis of the linearization effects of the 2nd order digitally processed signal for the linearization that modulates the 2nd harmonic of the fundamental carrier has been performed on the Doherty power amplifier for 5G modulation form. In the first method, linearization signals are injected at the input and output of the main Doherty amplifier, whereas in the second method, they are inserted at the outputs of the Doherty main and auxiliary amplifiers.

Keywords – 5G, FBMC, Doherty power amplifier, baseband signal, second harmonic, linearization.

I. INTRODUCTION

Fifth generation (5G) mobile communication systems represent one of the most important segments of the overall digital transformation of society based on the concept of Industry 4.0. The importance of 5G systems for the global development of the economy and society has been widely recognized, so that the coordinated introduction of 5G mobile networks in many countries has become part of the strategy of complete social and economic development. New technologies such as artificial intelligence (AI) and machine learning, cloud computing, augmented and virtual reality (AR / VR), IoE (Internet of Everything) and IoT (Internet of Things) and billions of connected devices are pushing boundaries and setting new demands on connectivity and mobile communication network performance. 5G mobile networks are expected to provide ultra-fast connectivity with low latency, not only to individual users, but also to a large number of connected facilities, as well as to create an ambient for expansion of technological and business innovations in different industrial sectors (agriculture, energy, trade, health, education, public safety, tourism, media, etc.). The frequency bands provided for 5G systems can be divided into three groups: High band (frequencies from 24 GHz to 60 GHz and above), mid band (which can be divided into two parts, from 1 GHz to 2.6 GHz and from 3.5 GHz to 6 GHz), and low band (below 1 GHz). Each of these bands has comparable advantages and disadvantages. The 5G systems operating in the low band will provide large cells but with a slight improvement in performance compared to 4G systems. In the high band range, all the advantages of the 5G systems in terms of performance compared to 4G systems will be expressed, with transfer speeds from 1 to 3 Gbps and even higher. The

disadvantage of high band is shown in the fact that due to the large attenuation of the signal as a result of millimeter wave propagation and potential interference from various obstacles (such as vegetation and buildings) it is necessary to provide very small cells. Mid band spectrum is considered ideal for 5G because it can carry plenty of data while also traveling significant distances.

The most important limitations that existed in previous generations of communication systems with OFDM modulation schemes are loss of spectral efficiency due to the use of cyclic prefix (CP) and needs for fine time and frequency synchronization to ensure the orthogonality of the carriers. To overcome these limitations, several alternative modulation schemes for 5G systems, known as 5G candidates, have been introduced over the past few years, such as filter bank multicarrier (FBMC), universal filtered multi carrier (UFMC), generalized frequency division multiplexing (GFDM) and filtered orthogonal frequency division multiplexing (FOFDM).

The results of Doherty power amplifier (DPA) linearization in simulation by applying a method that uses second-order digital signals processed in the baseband are presented in this paper. After adjusting for the amplitude and phase in the baseband, the second order digital signals modulate the second harmonic of the fundamental carrier and then are injected into the gate and drain (input and output) of the PA transistor [1]. The results obtained by applying this linearization method in simulation or experiments have already been published in [2-4] for single-stage PA and two-way DPA, which operate at a frequency of about 1 GHz and tested for QAM and OFDM modulation schemes. In this paper, we analyzed the behavior of the DPA when source signal is 5G FBMC signal.

The paper is organized in the following manner: after introduction, the second section is devoted to the 5G FBMC signal, and the results of the linearization are illustrated in the third section. Conclusion and list of used literature are given at the end of paper.

II. 5G FBMC SIGNAL

FBMC is a type of multi carrier modulation scheme based on OFDM. It represents an improvement of OFDM with the aim of eliminating certain shortcomings at the cost of increasing the complexity of signal processing. It consists of a set of data that are broadcast through a bank of modulation filters that filter each subcarrier. The prototype of the used filter can be chosen in a suitable way, so that there is very little leakage into the adjacent channels. FBMC has significantly better utilization of channel capacity and can offer higher data throughput in a given bandwidth, which

¹Aleksandar Atanasković, Nataša Maleš Ilić and Biljana Stošić are with the Faculty of Electronic Engineering, University of Nis, A. Medvedeva 14, Nis, Serbia (e-mails: aleksandar.atanaskovic; natasa.males.ilic; biljana.stosic@elfak.ni.ac.rs)

²Djuradj Budimir is with the University of Westminster, 115 New Cavendish Street, London, UK, (e-mail: d.budimir@wmin.ac.uk)

means it provides better spectral efficiency. Also, the FBMC has eliminated one of the main disadvantages of OFDM, which is the use of the cyclic prefix (CP) [5]. The cyclic prefix is essentially a copy of part of a transmitted symbol in OFDM that is appended at the beginning of the next symbol. This leads to a reduction in signal speed as well as unnecessary loss of transmitted power.

create the appropriate FBMC signal. This software was chosen because it provides a simple interface in which parameters related to the FBMC signal can be easily adjusted, and the impact of changing the appropriate parameters on the FBMC signal itself can be monitored, either in time or in the spectral domain. Figure 1 shows the interface for creating FBMC signals in the SystemVue environment, as well as a set of parameters that control the signal characteristics and signal appearance in the frequency domain.

III. RESULTS

Symmetrical two-way DPA that operates at 5G mid band was designed according to the instructions given in [6]. The DPA was designed by using CGH40010F GAN HEMT transistor. The drain voltage is 28 V, whereas the gate voltage of the main and auxiliary amplifier is -2.8 V, and -5.7 V, respectively. Main characteristics of DPA in simulation at 3.5 GHz are: 12.6 dB gain and 1-dB compression point at 31 dBm output power.

The designed DPA was linearized in ADS simulation using two linearization methods: 1) the first - standard method that leads linearization signals at the gate and drain of the transistor in the main cell of the DPA and 2) the second - modified method, where the linearization signals are put at the drain of the main and auxiliary amplifier transistors in the DPA [7]. The signal used for testing DPA was 5G FBMC signal at carrier frequency 3.5 GHz with useful signal frequency bandwidth of 50 MHz and two output power levels: around 30 dBm (1 dB below 1-dB compression point) and near 24 dBm (roughly 7 dB below 1-dB compression point).

The Figs. 2 and 3 show the output spectrum before and after application of the proposed linearization technique. Summarized results for ACP (Adjacent Channel Power) at ± 50 MHz offset over 5 MHz band are presented in Tables I and II. We can observe for 24 dBm output power, that the ACP is improved about 15 dB for both linearization methods, whereas for 30 dBm output power they become better by 5 dB for the 1st method and almost 8 dB for the 2nd method. A slight asymmetry can be noted in results for linearization between lower and upper adjacent channel.

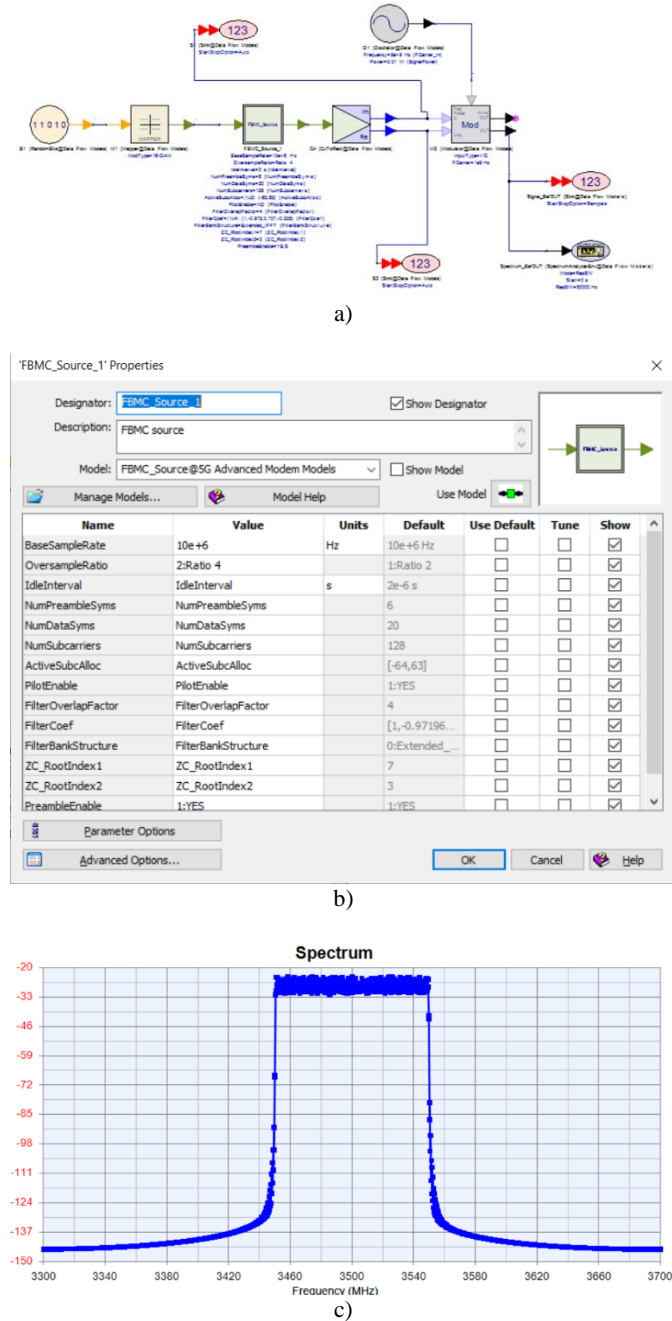


Fig 1. FBMC signal generation in Keysight SystemVue: a) FBMC transmitter; b) FBMC signal parameters; c) FBMC signal spectrum

FBMC signals for simulation purposes can be created using various software packages (Matlab, Keysight SystemVue, ...) or using general purpose programming languages (Python, C/C++, ...). In this paper, we used Keysight SystemVue to

TABLE I

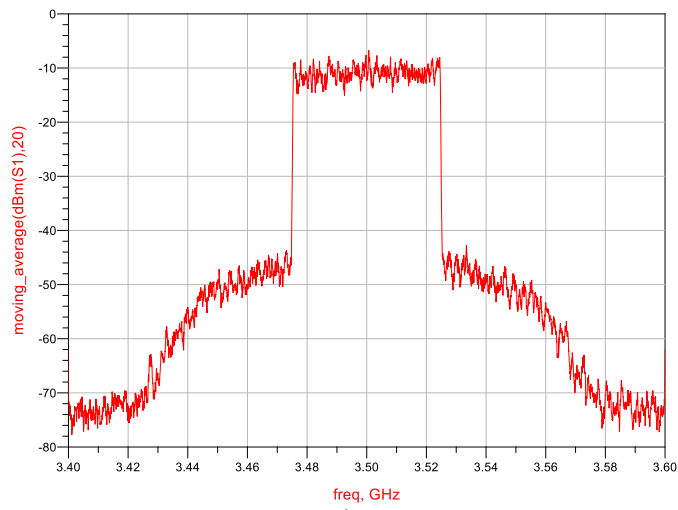
RESULTS OF LINEARIZATION FOR 24 DBM OUTPUT POWER

	Pout [dB]	ACP lower [dB]	ACP upper [dB]
Before lin.	24.1	-25.6	-26.5
Lin. by method 1	24.5	-41.0	-38.8
Lin. by method 2	24.4	-40.9	-39.1

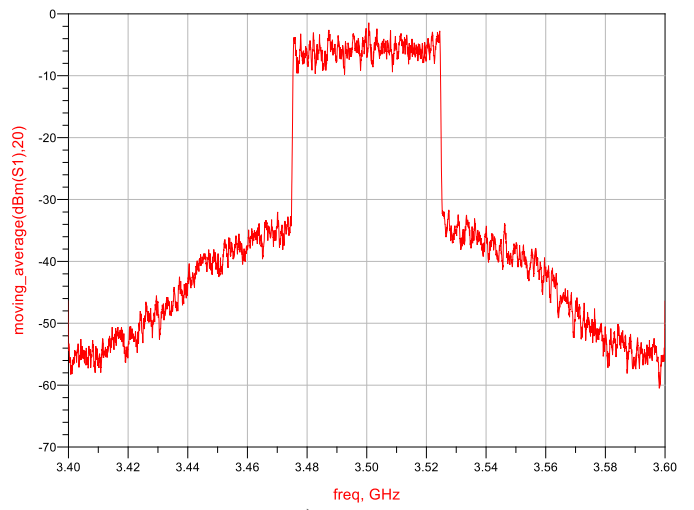
TABLE II

RESULTS OF LINEARIZATION FOR 30 DBM OUTPUT POWER

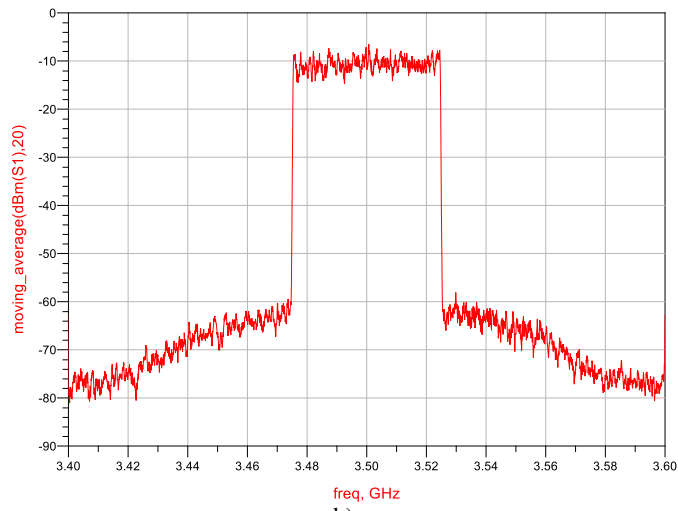
	Pout [dB]	ACP lower [dB]	ACP upper [dB]
Before lin.	29.4	-14.6	-14.5
Lin. by method 1	30.1	-19.2	-18.8
Lin. by method 2	30.2	-22.2	-20.7



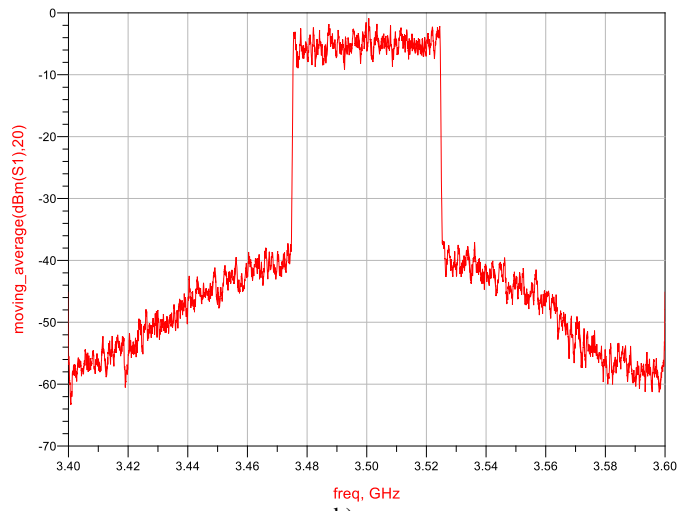
a)



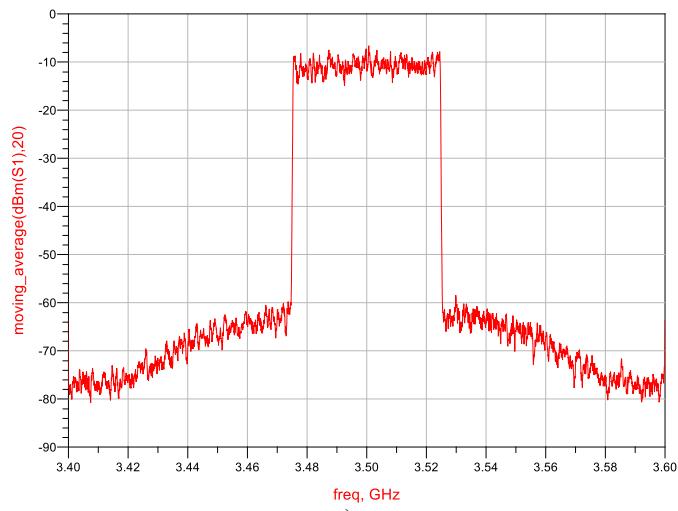
a)



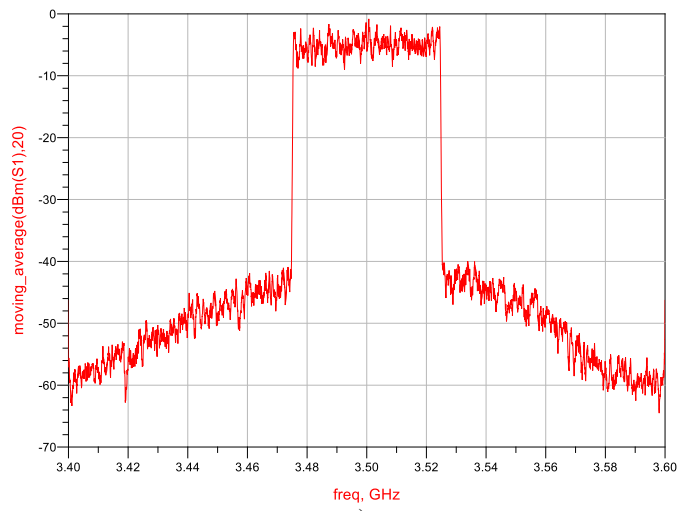
b)



b)



c)



c)

Fig. 2. Output spectrum for FBMC signal of 50 MHz useful signal frequency bandwidth for output signal power 24 dBm: a) before linearization; b) after linearization by method 1; c) after linearization by method 2

Fig. 3. Output spectrum for FBMC signal of 50 MHz useful signal frequency bandwidth for output signal power 30 dBm: a) before linearization; b) after linearization by method 1; c) after linearization by method 2

IV. CONCLUSION

We analyzed the effect of the linearization technique that uses baseband signals of the 2nd order nonlinearity adequately shaped and processed in magnitude and phase in baseband and then modulate the 2nd harmonic of the fundamental useful signal carrier. The linearization signals formed in this way are then inserted at the input and output of the main amplifier of DPA (linearization method 1) as well as at the output of the main and auxiliary amplifier of DPA (linearization method 2). The linearization was performed for the 5G FBMC signal.

It can be concluded that very acceptable improvement in adjacent channels power was achieved by applying the proposed linearization technique. On the bases of the obtained results, it can be noticed that the 2nd method provides slightly better results for higher power than the application of the 1st method.

ACKNOWLEDGEMENT

This work was supported by the Ministry of Education, Science and Technological Development of Republic of Serbia (Grant No. 451-03-68/2022-14/200102) and Science Fund of the Republic of Serbia (Grant No. 6398983 - Serbian Science and Diaspora Collaboration Program: Vouchers for Knowledge Exchange – project name: Digital Even-Order Linearization of 5G Power Amplifiers in Bands below 6GHz - DELFIN).

REFERENCES

- [1] Atanasković, N. Males-Ilić, K. Blau, A. Đorić and B. Milovanović, "RF PA Linearization using Modified Baseband Signal that Modulates Carrier Second Harmonic", *Microwave Review*, vol. 19, no.2, pp. 119-124, December 2013.
- [2] Đorić, A. Atanasković, N. Maleš-Ilić, M. Živanović: "Linearization of RF PA by Even-order Nonlinear Baseband Signal Processed in Digital Domain", *International Journal of Electronics*, Taylor & Francis, Vol.106, Issue No.12, pp.1904-1918, December 2019.
- [3] N. Maleš-Ilić, A. Atanasković, K. Blau, M. Hein, "Linearization of Asymmetrical Doherty Amplifier by the Even-Order Nonlinear Signals", *International Journal of Electronics*, Taylor & Francis, Vol.103, Issue No.8, pp.1318-1331, August 2016.
- [4] A. Atanasković, N. M. Ilić, A. Djorić and D. Budimir, "Doherty Amplifier Linearization in Experiments by Digital Injection Methods", *Proceedings of 15th International Conference on Advanced Technologies, Systems and Services in Telecommunications - TELSIS 2021*, Niš, Serbia, October 20-22, 2021, pp. 82-85.
- [5] M. Bozic, M. Cabarkapa, D. Barjamovic and D. Budimir, (2018), *Waveform Comparison and PA Nonlinearity Effects on CP-OFDM and 5G FBMC Wireless Systems*, *Microwave and Optical Technology Letters*, Vol. 60, No. 8, pp: 1952-1956, August 2018.
- [6] Z. Zhang, Z. Cheng, and G. Liu, "A Power Amplifier with Large High-Efficiency Range for 5G Communication", *Sensors*, 2020; 20(19):5581.
- [7] A. Đorić, A. Atanasković, B. Alorda, N. Maleš-Ilić: "Linearization of Doherty Amplifier by Injection of Digitally Processed Baseband Signals at the Output of the Main and Auxiliary Cell", *Proceedings of the 14th International Conference on Advanced Technologies, Systems and Services in Telecommunications - TELSIS 2019*, Niš, Serbia, October 23-25.

Planar Archimedean Spiral Antenna Resonant Frequency and Bandwidth Estimation using MLP Neural Network

Zoran Stanković, *Member, IEEE*, Maja Sarevska, Nebojša Dončov, *Senior Member, IEEE*, Ksenija Pešić

Abstract— This paper presents a neural model for fast estimation of the resonant frequency and bandwidth of a planar Archimedean spiral antenna based on MultiLayer Perceptron (MLP) network. The input parameters of the model are the number of turns of the spiral, the inner radius of the spiral and the outer radius of the spiral, while the output parameters of the model are resonant frequency, minimum operating frequency and maximum operating frequency of the Archimedean spiral antenna. The proposed neural model was applied in the process of modeling a planar self-complementary Archimedean spiral antenna with two arms.

Index Terms— Archimedean spiral antenna, neural network, neural model.

I. INTRODUCTION

Planar Archimedean spiral antennas, due to their low weight, simplicity of construction, low manufacturing cost and approximately frequency-independent characteristics in a wide frequency range, have significant applications in broadband communication systems (*Ultra-Wide Band (UWB)* communication systems, satellite communication systems, ground penetrating radars, military aircraft radars and other broadband systems) [1],[2].

The classic approach in the analysis of characteristics, modeling and design of such antenna structures is the use of EM simulators based on numerical EM modeling techniques such as Method of Moments (MoM), Finite Element Method (FEM), Transmission Line Matrix (TLM) method, Finite Difference Time Domain (FDTD) and others [3],[4]. The main disadvantages of this approach are the need for strong hardware resources and long computation times.

An alternative approach that can overcome the above problems is the use of artificial neural networks to model planar spiral antennas. For this purpose, a good candidate in

Zoran Stanković is with the Faculty of Electronic Engineering, University of Niš, A. Medvedeva 14, 18000 Niš, Serbia (e-mail: zoran.stankovic@elfak.ni.ac.rs).

Maja Sarevska is with American University of Europe-FON, str. Kiro Gligorov bb, 1000 Skopje, North Macedonia (e-mail: maja.sarevska@fon.edu.mk).

Nebojša Dončov is with the Faculty of Electronic Engineering, University of Niš, A. Medvedeva 14, 18000 Niš, Serbia (e-mail: nebojsa.doncov@elfak.ni.ac.rs).

Ksenija Pešić is with the Faculty of Electronic Engineering, University of Niš, A. Medvedeva 14, 18000 Niš, Serbia (e-mail: ksenija.pesic@elfak.ni.ac.rs)

the modeling process is the MultiLayer Perceptron (MLP) network [5],[6], which has shown good results in modeling planar antenna structures [7],[8].

As part of the research covered by this paper, the "ASA_design_MT software" was first implemented for the analysis of the characteristics and design of the planar Archimedean spiral antenna with two arms. Then, a neural model of this antenna was developed, which is based on the MLP network and which is presented in this paper. Data generated by ASA_design_MT software was used to develop this model.

II. PLANAR ARCHIMEDEAN SPIRAL ANTENNA

The architecture of the planar Archimedean spiral antenna with two arms is shown in Figure 1. The basic geometric parameters of the antenna are: inner radius of the spiral antenna r_i , outer radius of the spiral antenna r_o , arm width w , space between arms s , and feed point f .

The Archimedean spiral curve is determined by the equation

$$r = a\theta + r_i \quad (1)$$

where r is the radius of curve, a is the growth rate, θ is the winding angle, and r_i is the inner radius of spiral [2]. Accordingly, the outer radius of the spiral is defined in a way

$$r_o = 2\pi ta + r_i \quad (2)$$

where t is the number of spiral turns. Two edge curves of c_1 and c_2 describe one spiral arm as

$$\begin{aligned} c_1 &= a\theta + r_i \\ c_2 &= a(\theta + \theta_{off}) + r_i \end{aligned} \quad (3)$$

where θ_{off} is the offset angle. The metal (arm) width w and the metallization ratio χ of spiral antenna can then be defined as [2]

$$\begin{aligned} w &= |c_1 - c_2| = a\theta_{off} \\ \chi &= \frac{w}{w + s} = \frac{\theta_{off}}{\pi} \end{aligned} \quad (4)$$

In this paper, the case where the Archimedean spiral antenna is a self-complementary antenna is considered. This case is obtained when the condition $w = s$ is met. In this case

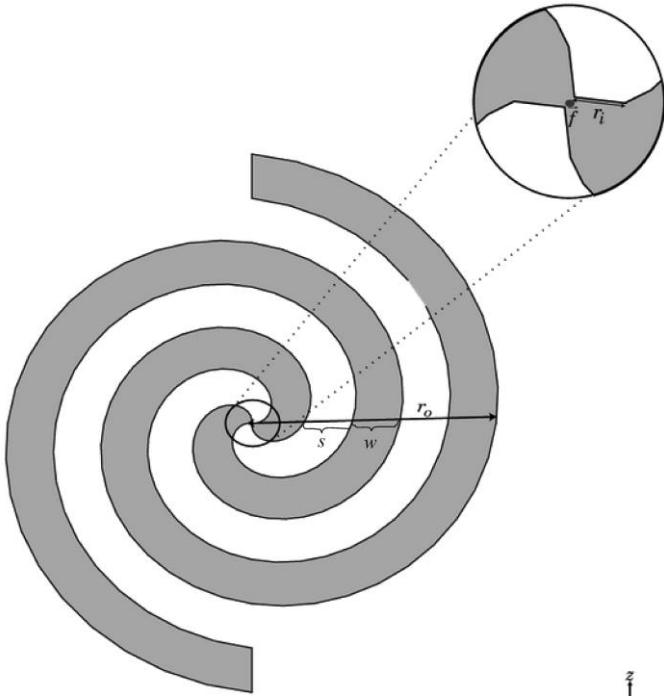


Fig. 1. Architecture of the planar Archimedean spiral antenna with two arms (r_i - inner radius of the spiral antenna, r_o - outer radius of the spiral antenna, w - arm width, s - space between arms, f - feed point).

the metallization ratio, offset angle, growth rate and arm width can be determined by equations

$$\begin{cases} \chi = \frac{1}{2} \\ \theta_{off} = \frac{\pi}{2} \\ a = \frac{2w}{\pi} \\ w = \frac{r_o - r_i}{4t} \end{cases} \quad (5)$$

By applying Babinet's principle [1]

$$z_{metal} z_{air} = \frac{\eta_0^2}{4} \quad (6)$$

where η_0 is the characteristic impedance of free space, to an ideal planar self-complementary Archimedean spiral antenna ($r_i \rightarrow 0$, $r_o \rightarrow \infty$), the input impedance of the antenna can be calculated [1]

$$z_{in} = \frac{\eta_0}{2} \approx 188 \Omega \quad (7)$$

In this case the antenna has infinite bandwidth and all primary characteristics (input impedance, antenna efficiency) and secondary characteristics of the antenna (radiation characteristics, directivity, polarization) are frequency independent. If the planar self-complementary Archimedean spiral antenna has limited physical dimensions then its bandwidth is wide but limited and its impedance deviates to

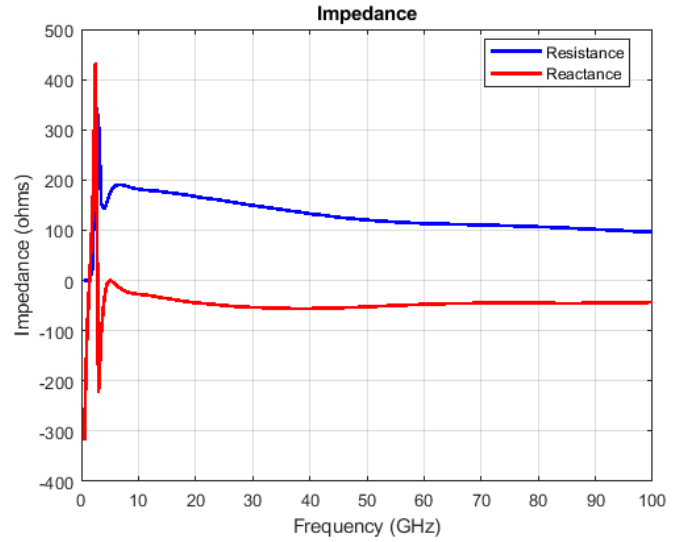


Fig 2. Impedance of the planar self-complementary ASA vs frequency ($t = 1$, $r_i = 2$ mm $r_o = 2$ cm)

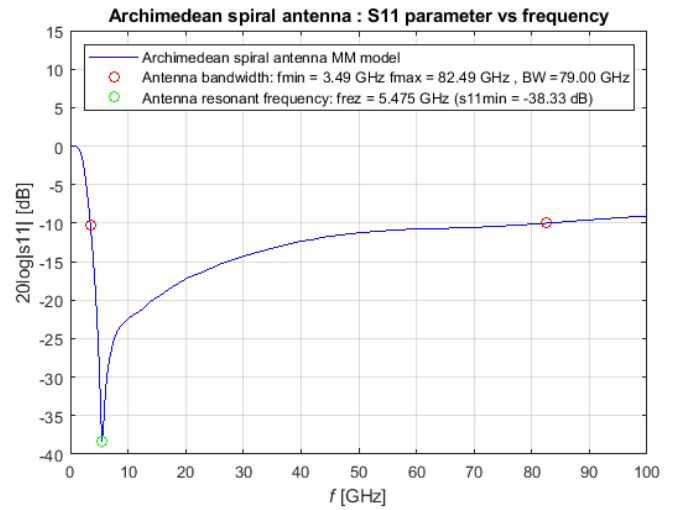


Fig. 3. S_{11} parameters of the planar self-complementary ASA vs frequency ($t = 1$, $r_i = 2$ mm $r_o = 2$ cm)

some extent from 188Ω . In this case, the approximate theoretical formula for determining the lower bound of bandwidth is [1]

$$f_{min} = \frac{c}{2\pi r_o} \quad (8)$$

In practice, the lower bound of bandwidth will be greater than predicted by Eq.8 due to reflections from the end of the arm.

If the antenna does not use a tapered feed region in the spiral center, the upper bound of bandwidth can be determined by the approximate theoretical formula [1]

$$f_{max} = \frac{c}{2\pi r_i} \quad (9)$$

In practice, the upper bound of bandwidth differs from the theoretical value due to the influence of the real physical geometry of the feed region.

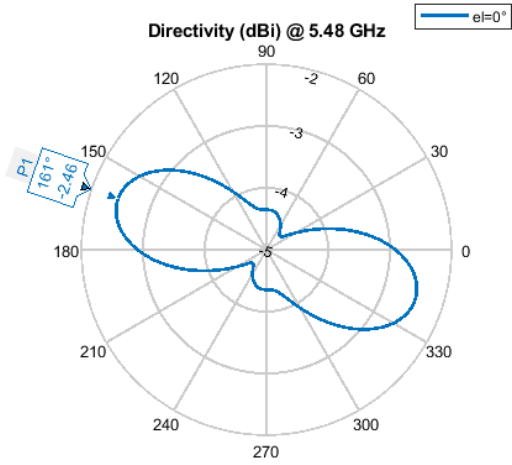


Fig. 4. Directivity of the planar self-complementary ASA in the azimuthal plane at $f_r = 5.475$ GHz ($t = 1$, $r_i = 2$ mm $r_o = 2$ cm)

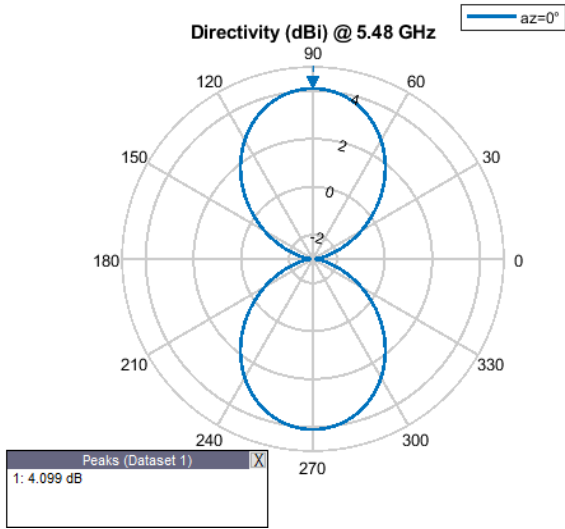


Fig. 5. Directivity of the planar self-complementary ASA in the elevation plane at $f_r = 5.475$ GHz ($t = 1$, $r_i = 2$ mm $r_o = 2$ cm)

III. EM MODELING OF A PLANAR ASA USING “ASA_DESIGN_MT” SOFTWARE

In order to perform EM analysis and modeling of primary and secondary characteristics of the planar self-complementary Archimedean spiral antenna (ASA), “ASA_design_MT” software was developed. This software is based on Method of Moments (MoM) and is implemented using the MATLAB Antenna toolbox.

Figures 2 and 3 show the impedance and s_{11} parameter as a function of frequency for a planar self-complementary ASA with physical parameters $t = 1$, $r_i = 2$ mm and $r_o = 2$ cm. It can be seen that the antenna at the resonant frequency $f_r = 5.475$ GHz has a resistance of 188 Ω . As the frequency increases, the impedance takes on a slightly capacitive character, while the resistance slowly decreases compared to 188 Ω .

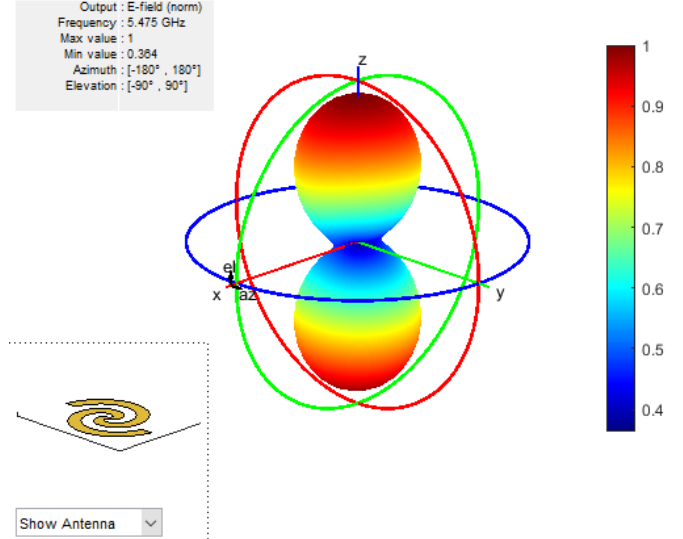


Fig. 6. 3D radiation pattern of the planar self-complementary ASA at $f_r = 5.475$ GHz ($t = 1$, $r_i = 2$ mm $r_o = 2$ cm)

Figures 4, 5 and 6 show the directivity of the planar self-complementary ASA in the azimuthal plane, the directivity of the planar self-complementary ASA in the elevation plane and the 3D radiation pattern of the planar self-complementary ASA at resonant frequency, respectively.

IV. MLP MODEL OF THE PLANAR SELF-COMPLEMENTARY ASA

The MLP model of the planar self-complementary ASA (MLP_ASA) consists of a single MLP network and its architecture is shown in Figure 7. MLP_ASA models the dependence of lower bound of bandwidth, resonant frequency and upper bound of bandwidth on the following physical parameters: number of spiral turns, inner radius of spiral and outer radius of spiral. Therefore, MLP_ASA can be functionally described by the following expression

$$[f_{\min} \ f_r \ f_{\max}]^T = f_{MLP_ASA}([t \ r_i \ r_o]^T) \quad (10)$$

MLP networks consist of a single input layer, a single output layer, and multiple hidden layers of neurons. In accordance with Eq. 10, the input layer has three neurons, the output layer has three neurons, while the hidden layers have N_1, N_2, \dots, N_H neurons respectively, where H is the total number of hidden layers. For MLP network with a specific number of layers and neurons in them, notation was used $MLPH-N_1 \dots -N_H$, $1 \leq i \leq H$.

The outputs of the hidden layers are given by the expression

$$\mathbf{y}_l = F(\mathbf{w}_l \mathbf{y}_{l-1} + \mathbf{b}_l) \quad l = 1, 2, \dots, H \quad (11)$$

where \mathbf{y}_0 represents the output of the input layer and vectors \mathbf{y}_l and \mathbf{y}_{l-1} represent the output of l -th and $(l-1)$ -th hidden layer, respectively. Weight matrix for connections between neurons in $(l-1)$ -th and l -th layers is denoted by \mathbf{w}_l , while biases of l -th hidden layer neurons are represented by vector \mathbf{b}_l . Neurons in

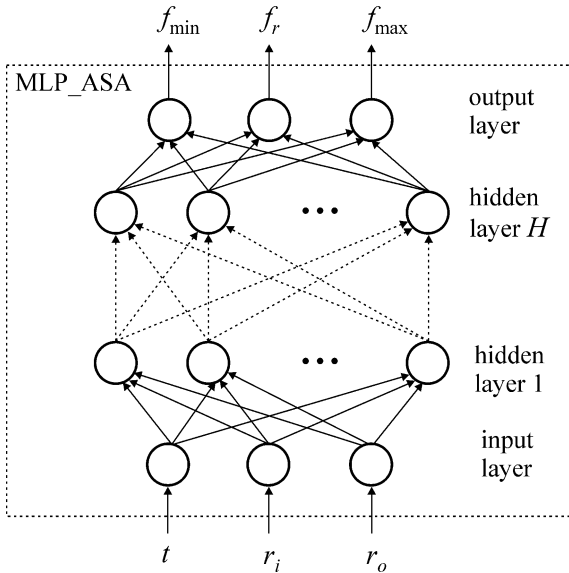


Fig. 7. The MLP neural model of the planar self-complementary Archimedean spiral antenna

hidden layers have the hyperbolic tangent sigmoid activation function $F(\cdot)$ defined by the expression

$$F(u) = \frac{e^u - e^{-u}}{e^u + e^{-u}} \quad (12)$$

The neurons in the output layer use a linear activation function so that their output is defined in a way

$$\begin{bmatrix} f_{\min} & f_r & f_{\max} \end{bmatrix}^T = \mathbf{w}_{H+1} \mathbf{y}_H + \mathbf{b}_{H+1} \quad (13)$$

where \mathbf{w}_{H+1} is a weight matrix for connections between neurons of the last hidden layer and output layer neurons.

During the training of the MLP network, the weight matrices $\mathbf{w}_1, \mathbf{w}_2, \dots, \mathbf{w}_H, \mathbf{w}_{H+1}$ and bias vectors $\mathbf{b}_1, \mathbf{b}_2, \dots, \mathbf{b}_H, \mathbf{b}_{H+1}$ are optimized in order to achieve the desired mapping accuracy defined by the expression Eq. 10.

V. MODELING RESULTS

Using the “ASA_design_MT” software 1000 samples are generated for training and 300 samples for testing having random distribution.

With the aim to develop a model with better accuracy the training was done for various $MLPH-N_1 \dots -N_r \dots -N_H$ networks while only networks with two hidden layers were used ($H = 2$). For the number of neurons in the hidden layer, the values that were used are $6 \leq N_1, N_2 \leq 22$.

The MLP training is done using Levenberg – Marquardt algorithm with given goal mean squared error of training $MSE_{target} = 10^{-4}$ and maximal number of iterations $N_{max} = 500$. Before training the neural connection weights and biases are initialized with random values in the range [-1 1]. Also input network data are scaled and output data are descaled in the range [-1 1]. After the training each network is tested using test data in order generalization capabilities to be evaluated. For the evaluation of the generalization capabilities of the

network and its accuracy the following test metrics are used: mean squared error (RMSE) and Pearson product moment correlation coefficient (r^{PPM}) [6].

The Table I shows the testing results for eight MLP networks that showed best testing results after training. It may be seen that the networks have small RMSE in the lower bandwidth limit and resonant frequency, while in the estimation of the upper bandwidth limit they have much higher RMSE.

For the realization of the MLP model of the planar self-complementary Archimedean spiral antenna MLP2-9-8 is chosen as this network in the testing procedure had largest value for the Pearson product moment correlation coefficient.

TABLE I
TEST RESULTS FOR EIGHT MLP MODELS WITH THE HIGHEST r^{PPM} VALUE

MLP networks	RMSE (f_{\min})	RMSE (f_r)	RMSE (f_{\max})	r^{PPM}
MLP2-9-8	0.1628	0.3345	6.4747	0.9939
MLP2-10-9	0.1537	0.3628	6.4915	0.9938
MLP2-8-8	0.1584	0.3144	6.5339	0.9937
MLP2-8-11	0.1590	0.3980	6.5706	0.9937
MLP2-8-10	0.1606	0.3747	6.6170	0.9936
MLP2-11-10	0.1568	0.3223	6.5715	0.9936
MLP2-12-8	0.1569	0.3174	6.6360	0.9936
MLP2-8-15	0.1622	0.3517	6.6686	0.9935

On Fig.8 the scattering diagram of MLP2-9-8 model output is shown. It may be noticed the good match for the lower bandwidth limit and resonant frequency with the referent values. Also it may be noticed that for the values of the upper bandwidth limit the match is not so good as for the two previously mentioned parameters. This may be explained with fact that EM simulator while training sample generation had difficulty to accurately determine the upper limit of the bandwidth. The reason for that is that for higher frequencies the function of parameter s_{11} almost asymptotically approach the bound of -10 dB so the indetermination of the cross point estimation between that function and the horizontal line $s_{11} = -10$ dB is very large.

For above explained situation MLP model of the planar self-complementary ASA may be used only for rough estimation of the upper bound of the bandwidth. But this does not decrease the useful application of the proposed model because in real life the detremination of the lower bound of the bandwidth is more important than for the upper bound. The reason for this is that upper bound frequency is much higher than the maximal working frequency for emission and reception.

MLP model of the planar self-complementary ASA is implemented on a modest referent hardware platform (Intel Core i3-2350M@2.3 GHz, 4GB RAM). This model, the estimation of the resonant frequency, the minimum operating

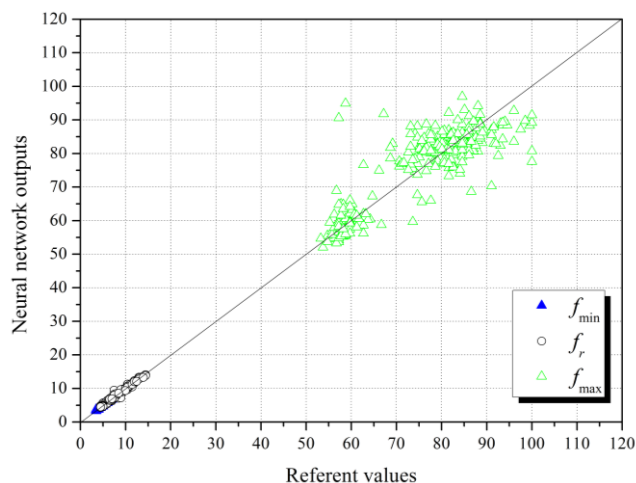


Fig. 8. Scattering diagram for MLP2-9-8 network

frequency and the maximum operating frequency of the antenna, has performed in 300 points defined with testing set for only 0.03 s. This speaks about the high speed of the MLP model.

VI. CONCLUSION

Today planar spiral antennas attract more and more attention because they are convenient for the application in the modern portable broadband communication devices. The modeling of these antenna structures with the help of EM simulators that are based on MoM techniques presents classical approach in EM characteristics modeling. Because of intensive numerical estimations this kind of EM simulators demand strong hardware platform and estimations itself may last very long, that is main disadvantage of the EM simulator approach. Alternative approach for the spiral antenna modeling is using of artificial neural networks.

This paper presents the MLP model of the planar self-complementary Archimedean spiral antenna that is implemented on a modest hardware platform. MLP model has shown exceptional speed in the estimation of resonant frequency, minimum operating frequency and maximum operating frequency for this antenna structure. Currently developed model supports estimation of the resonant frequency and minimum operation frequency with high accuracy and rough (low accuracy) estimation of high operating frequency for the antenna.

Further investigations will be steered to the increased MLP model accuracy for the planar self-complementary Archimedean spiral antenna in the maximum operating frequency estimation.

ACKNOWLEDGMENT

This work was supported by the Ministry of Education, Science and Technological Development of Republic of Serbia (Grant No. 451-03-9/2021-14/200102).

REFERENCES

- [1] Balanis, C. A., *Antenna Theory: Analysis and Design*, Wiley, New York, 2005.
- [2] Teng-Kai Chen and Gregory H. Huff, "Travelling Wave Mechanism and Novel Analysis of the Planar Archimedean Spiral Antenna in Free Space," *Progress In Electromagnetics Research*, Vol. 145, 287-298, 2014, doi:10.2528/PIER14011901.
- [3] Matthew N. O. Sadiku, *Numerical techniques in electromagnetics*, 2nd edition, CRC Press LLC, 2001.
- [4] Levent Sevgi, *Electromagnetic Modeling and Simulation*, First Edition.. The Institute of Electrical and Electronics Engineers, Inc. Published by John Wiley & Sons, Inc., 2014
- [5] S. Haykin, *Neural Networks*, New York, IEEE, 1994.
- [6] Q. J. Zhang, K. C. Gupta, *Neural networks for RF and microwave*
- [7] K. Pesic, Z. Stankovic and N. Doncov, "ANN-EM Model of Dual Band Square Patch Antenna with a Floating Rectangular Slot," 2021 15th International Conference on Advanced Technologies, Systems and Services in Telecommunications (TELSIKS), 2021, pp. 153-156, doi: 10.1109/TELSIKS52058.2021.9606409.
- [8] M. Milijić, Z. Stanković and B. Milovanović, "Efficient model of slotted patch antenna based on neural networks," *2009 9th International Conf. on Telecommunication in Modern Satellite, Cable, and Broadcasting Services*, Nis, 2009, pp. 384-387.

Analysis of Feeding Methods for High-Gain Crossed Slot Antenna Arrays

Marija Milijic, *Member, IEEE*, Branka Jokanovic, *Senior Member, IEEE*

Abstract— In this paper we present the influence of different feeding methods on performances of the dual polarized antenna array. Antenna array consists of 14 identical crossed slots serially fed by coplanar waveguide (CPW) and positioned at equal distances forming a linear array. Three proposed feeding methods are compared with the ideal case when two antenna sub – arrays are fed by two generators to achieve the highest possible gain. The CPW-T junction, CPW rat-race coupler and modified CPW rat-race coupler are engaged for feeding 2D crossed slots array to analyze its performances for use in 5G and radar applications.

Index Terms—Antenna array; CPW-fed antenna; CPW T-junction; CPW rat-race coupler; crossed slot antenna.

I. INTRODUCTION

FOR operation at millimeter waves, antenna arrays are very attractive candidates considering high-gain and beamforming characteristic. However, the feed network, its necessary part that enables suitable amplitude and phase distributions for a large number of radiating elements in array, increases both design complexity and size of antenna. Otherwise, antennas in printed circuit technology have aroused more and more attention as one of vital components in modern 5G wireless communication system thanks to their planar structure, compact design, inexpensive and uncomplicated manufacture [1]. The printed antennas as elements in an array are usually fed by corporate-feed network, when there are a multiple lines for feeding array elements, or by series-feed network, when elements are fed by a single line. A series-feed network can be easily modeled and cheaply fabricated using simultaneous photolithography for both the radiating elements and the feed network [2,3]. However, a corporate-feed network is widely used to provide desired power splits necessary to synthesize a required radiation pattern or to achieve high side lobe suppression [4,5]. Some research has employed the combination of series and corporate feed methods to obtain the desired antenna characteristics.

There are some considerable losses typical for high operating frequency of mm-waves antennas as free-space path loss and propagation loss due to atmospheric absorption. They are both lower at the frequencies below 28 GHz wherefore the

Marija Milijic is with the Faculty of Electronic Engineering, University of Ni, Aleksandra Medvedeva 14, 18000 Nis, Serbia, E-mail: marija.milijic@elfak.ni.ac.rs

Branka Jokanovic is with the Institute of Physics, University of Belgrade, Pregrevica 118, 11080 Pregrevica, Serbia, and The Academy of Engineering Sciences of Serbia, Kraljice Marije 16, Belgrade, Serbia E-mail:brankaj@ipb.ac.rs

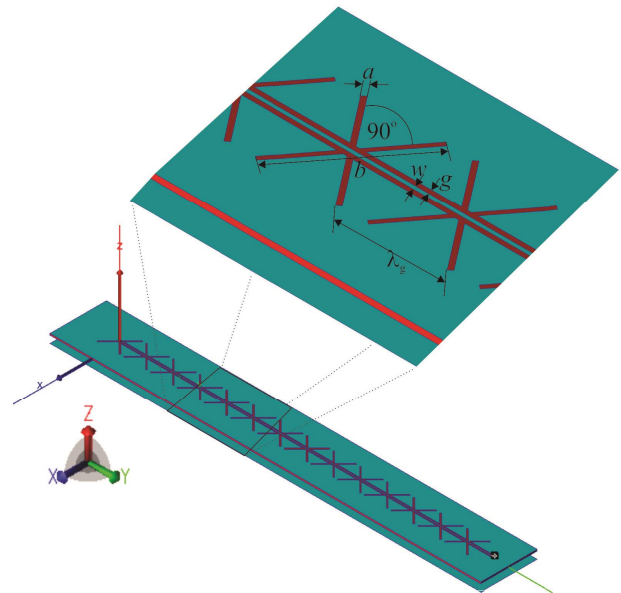


Fig. 1. Linear CPW-fed crossed slot array.

frequencies between 24.25 ó 27.5 GHz are tag as a promising operation bandwidth for the next-generation 5G networks and technologies [6]. Therefore, the antennas proposed in this paper are model and simulated for the center frequency $f_c=25.875$ GHz calculated as the central value of that band. This is an extension of the research presented in [7,8] that modeled the advanced high-gain rectangular slot antenna arrays fed by CPW feeding line.

This paper analyzes firstly a linear array of identical 14 crossed slots, positioned symmetrically relative to the CPW feeding line. The crossed slot antennas, whose two rectangular parts are positioned at right angle, are dual polarized antenna with identical radiation patterns for both vertical and horizontal polarization [9]. Further, the linear crossed slot array has replicated forming CPW-fed 2D array. The following types of feeding methods are investigated: feeding by two generators for every sub ó array, CPW óT junction, CPW rat-race coupler and modified CPW rat-race coupler. The simulated results, especially gain and bandwidth, obtained by WIPL-D Pro CAD [10] software are discussed and compared.

II. LINEAR CPW-FED CROSSED SLOT ARRAY

The radiating element in proposed antennas is a crossed slot that consists of two rectangular parts with dimensions $a \times b$ - slot width \times slot length, positioned at right angle to each other [9]. The identical fourteen crossed slots are combined to form an array (Fig 1). A series feed is in a form of coplanar

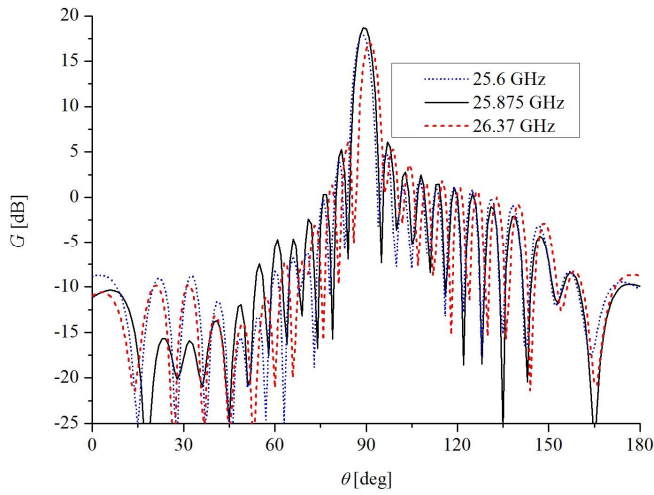


Fig. 2. Radiation patterns in the yOz plane ($\varphi=90^\circ$) of the proposed 14 crossed slots antenna array.

waveguide (CPW) transmission line with strip and gap (w and g) of 0.3 mm and 0.375 mm, respectively resulting in characteristic impedance around 120 Ω . The slots are positioned symmetrically along to the CPW feeding line at the mutual distance $\lambda_g=9$ mm where λ_g is CPW line wavelength at the center frequency f_c . Their dimension $a=0.44$ mm and $b=10.84$ mm are optimized at an operating frequency f_c [9]. The proposed antenna design is built on a substrate that has a dielectric constant (ϵ_r) of 2.54 and the dimensions 145 mm x 19 mm x 0.508mm. At the distance $\lambda_0/4 = 2.89$ mm from the array there is a reflector plate whose dimension are the same as the substrate's dimensions (λ_0 is the wavelength in vacuum at the center frequency $f_c=25.875$ GHz). Unlike the microstrip antennas with a backside ground plane, slot antennas require the reflector plane to be at a distance equal to the quarter of the free space wave-length. It should ensure that the antenna radiates only in half the space.

Fig. 2 shows the radiation patterns of the proposed 14 crossed slot antenna array at three frequencies: center f_c , lower (25.6 GHz) and higher (26.37 GHz) edge frequencies. The edge frequencies are determined by the criteria that the maximum gain at an edge frequency does not vary more than 10% of the maximum gain at the center frequency and that its side lobe suppression (SLS) is bigger than 10 dB. The maximum gain of the proposed 14 crossed slots antenna array at the center frequency f_c is 18.7 dBi while it is 18 dBi at the lower and 17 dBi at the higher edge frequency. The antenna has its maximum gain for $\theta=89^\circ$ at lower edge frequency, for $\theta=90^\circ$ at center frequency f_c and for $\theta=91^\circ$ at higher edge frequency. Moreover, its SLS is 12.5 dB at the center frequency while it is 13 dB at the lower and 11 dB at the higher edge frequency. Its S_{11} parameter, normalized to the impedance of CPW feeding line (120 Ω), is depicted in Fig. 3. It is less than -10 dB for the frequency range between 25.6 GHz and 26.74 GHz which is more than range determined by radiation pattern.

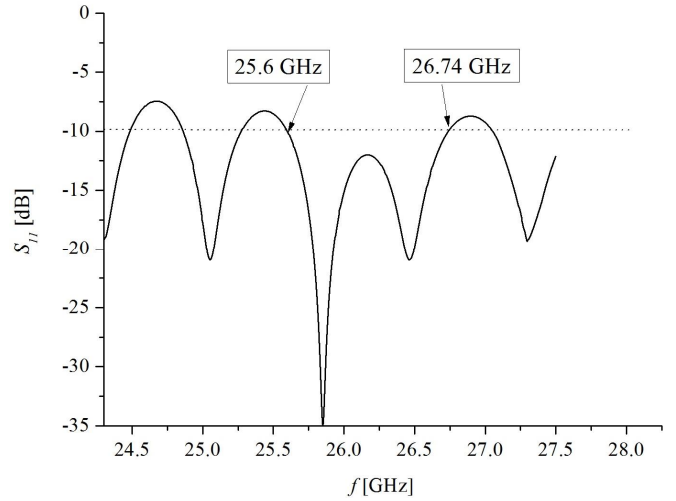


Fig. 3. S_{11} parameter versus frequency of the proposed 14 crossed slots antenna array. S-parameters are normalized to the 120 Ω impedance of CPW feeding line.

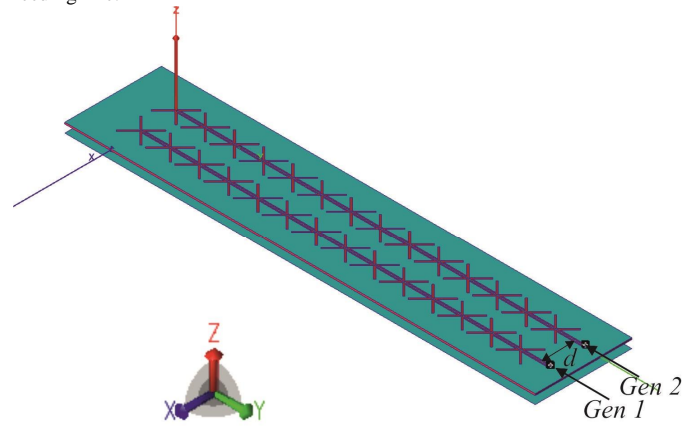


Fig. 4. 2D CPW-fed crossed slot array fed by two independent generators.

III. 2D CPW-FED CROSSED SLOT ARRAY

Two identical linear 14 crossed slot sub-arrays, presented in previous section, are associated together at the mutual distance $d=10.8$ mm building a 2D array (Fig. 4). It is situated on the substrate with dimensions 145 mm x 29.8 mm x 0.508 mm while the equal reflector plate is at the distance $\lambda_0/4$.

The feed structure, required to enable equal amplitude and phase distribution for both subarrays, must be designed in order to achieve the best radiation and bandwidth properties. Therefore, different feeding techniques are modeled and studied: feeding by two generators for every sub-array, CPW δ T junction, CPW rat-race coupler and modified CPW rat-race coupler.

A. Feeding by Two Generators

In the first study, the two sub-arrays are fed by two generators placed at the end of CPW lines (Fig. 4). Due to the influence of the mutual coupling between sub-array in x-axis direction, the dimensions of crossed slot antennas are optimized to the different values $a=0.53$ mm and $b=10.78$ mm in the respect to the linear array. The radiation patterns of 2D crossed slots antenna fed by two generators is depicted in Fig. 5.

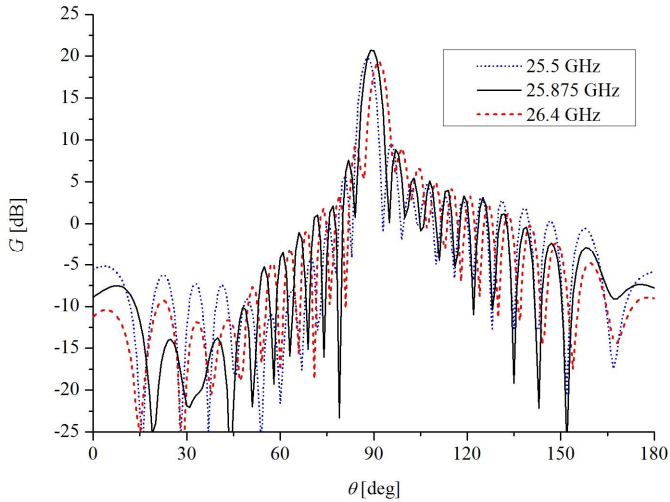


Fig. 5. Radiation patterns in the yOz plane ($\phi=90^\circ$) of the 2D CPW-fed crossed slots array fed by two independent generators.

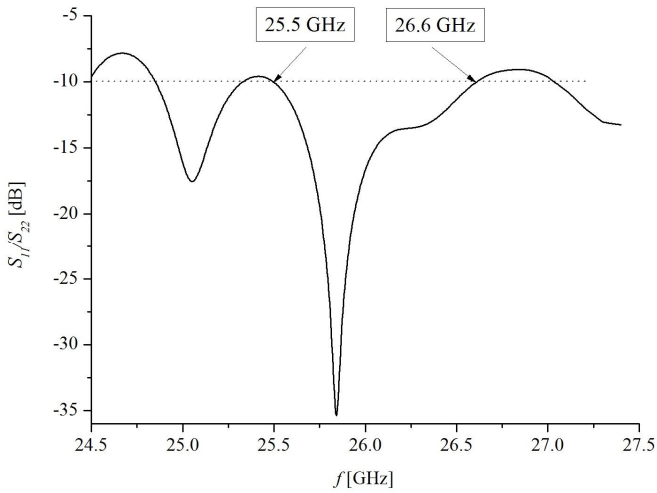


Fig. 6. S_{11} and S_{22} parameter versus frequency of the 2D CPW-fed crossed slots array fed by two generators. S-parameters are normalized to the $120 \text{ } \Omega$ - impedance of CPW feeding lines.

Because there are two sub-arrays of 14 crossed slots, the gain at the center frequency f_c is 20.7 dBi ($\theta=90^\circ$). At the edge frequencies the gain drops off a bit: it is 19.9 dBi ($\theta=88^\circ$) at lower edge frequency (25.5 GHz) and 19.3 dBi ($\theta=92^\circ$) at higher edge frequency (26.4 GHz). SLS is 12 dB at the center frequency f_c while it falls to 10 dB at the edge frequencies. However, as the previously discussed linear 14 crossed slots antenna, the proposed 2D CPW-fed crossed slots antenna has the bigger range where its S_{11} parameters (Fig. 6), normalized to the $120 \text{ } \Omega$ -impedance of CPW feeding line, is less than -10 dB (25.5 GHz ó 26.6 GHz) then the range of the satisfying radiation patterns (25.5 GHz ó 26.4 GHz). Besides very good radiation properties of the proposed 2D crossed slots antenna fed by two generators, it is necessary to design the unique feed to enable the uniform amplitude and phase distribution for both arrays and therefore CPW T-junction and CPW race couplers are introduced.

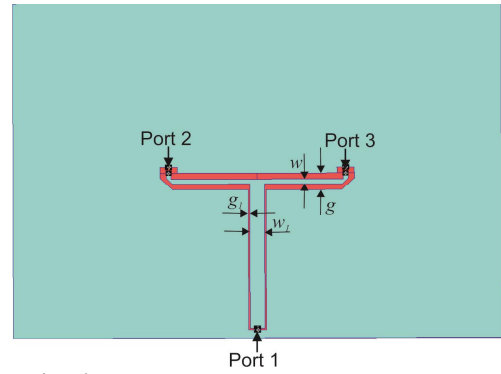


Fig. 7. CPW-T junction.

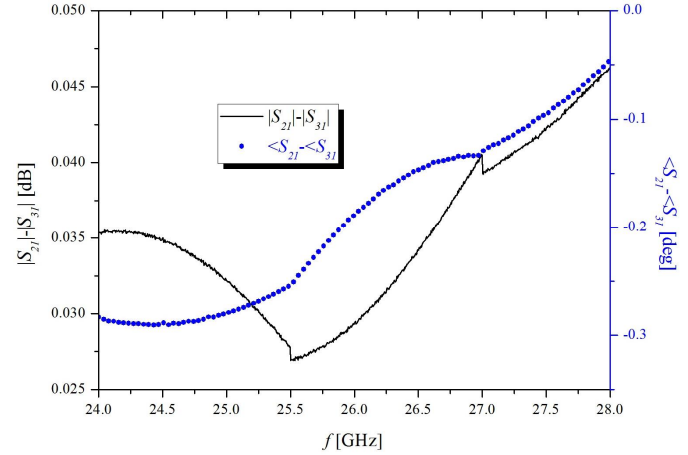


Fig. 8. The difference between insertion losses calculated at ports 2 and 3 of CPW T-junction. S-parameters are normalized to the impedance of CPW feeding line ($120 \text{ } \Omega$).

B. CPW-T junction

Further, the 2D array is fed by the T junction power divider implemented with coplanar waveguide transmission lines (CPW ó T junction). Configuration of the proposed CPW power divider is shown in Fig. 7. The CPW feed line is $60 \text{ } \mu\text{m}$ - CPW line (featuring the strip $w_1=0.9 \text{ mm}$ and gap $g_1=0.1 \text{ mm}$), that enables equal feeding for both sub - arrays dividing power into two $120 \text{ } \mu\text{m}$ CPW feed lines featuring the strip $w=0.3 \text{ mm}$ and gap $g=0.375$.

The difference between S-parameters (magnitudes ($|S_{ij}|$) and phases ($\angle S_{ij}$) of S_{21} and S_{31} S scattering (S-) parameters for left and right subarrays) is presented in Fig. 8. Analyzing shown results, it can conclude that proposed CPW T junction provides necessary equal feeding for both subarrays for range between 24-28 GHz. Therefore, CPW T-junction is used to feed the 2D crossed slots array. The whole structure, 2D array and CPW T-junction, is situated on the substrate with dimensions $150 \text{ mm} \times 29.8 \text{ mm} \times 0.508 \text{ mm}$ while the equal reflector plate is at the distance $\lambda_0/4$ (Fig. 9).

The Fig. 10 presents the radiation pattern of 2D crossed slots array fed by CPW T-junction. The radiation pattern at the center frequency f_c features with gain of 18.45 dBi at $\theta=90^\circ$ and SLS of 12 dB. At the lower edge frequency (25.49 GHz) the gain is 18.16 dBi at $\theta=88^\circ$. At the higher edge frequency (26.45 GHz) the gain is 17.48 dBi at $\theta=92^\circ$. SLS for both edge frequencies is 10 dB. S_{11} parameter is less than -10 dB for the frequency above 25.49 GHz (Fig. 11).

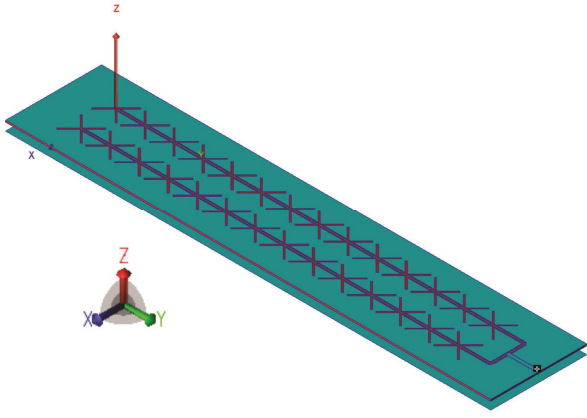


Fig. 9. 2D CPW-fed crossed slot array fed by CPW T-junction.

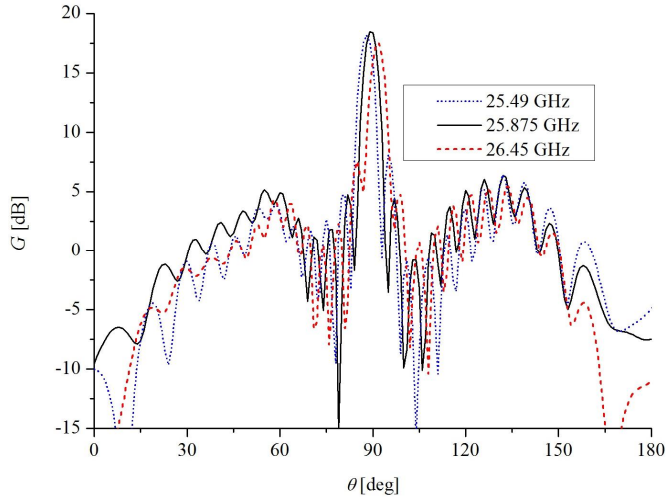


Fig. 10. Radiation patterns in the yOz plane ($\varphi=90^\circ$) of the 2D CPW-fed crossed slots array fed by CPW T-junction.

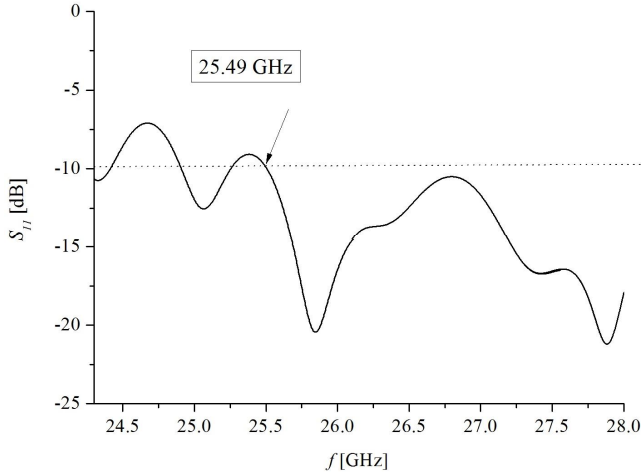


Fig. 11. S_{11} parameter versus frequency of the 2D CPW-fed crossed slots array fed by CPW T-junction. S-parameter is normalized to the impedance of CPW feed line 60Ω .

C. CPW rat-race coupler

The additional research employs CPW rat-race coupler, with the shape of a ring/circle, to provide required feeding for both sub-arrays. Rat race couplers have been very attractive for use in many applications such as mixers, multipliers, amplifiers, beamformers, etc. [11]. One of its disadvantages is that its big circumference ($3\lambda_g/2$) requests too much space increasing the overall size of antennas.

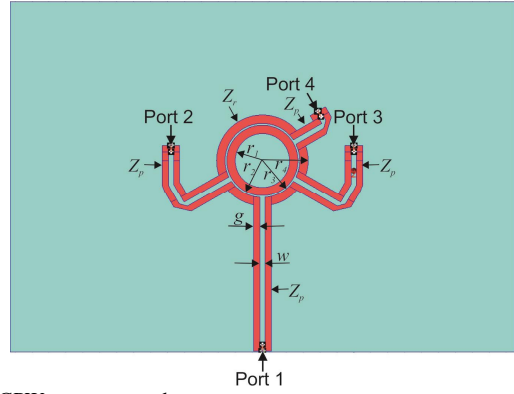


Fig. 12. CPW rat-race coupler.

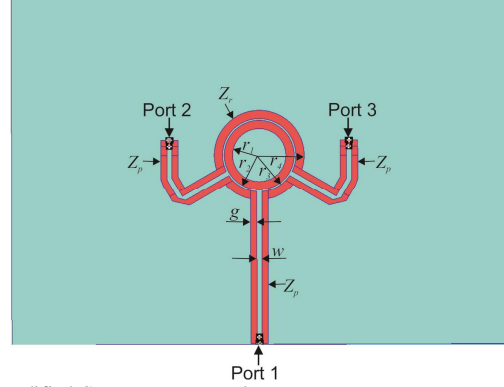


Fig. 13. Modified CPW rat-race coupler.

The proposed CPW rat-race coupler has 4 ports with $Z_p=120 \Omega$ impedance as numbered in Fig. 12, each of which is presented by CPW feed line featuring the strip $w=0.3 \text{ mm}$ and gap $g=0.375$. Each port is placed at a distance of one-quarter wavelength (λ_g) away from the other around the one half of the ring. The CPW forming the ring has a impedance $Z_r=\zeta^2 Z_p=\zeta^2 \cdot 120=169.7 \Omega$ with gap $g_r=0.5 \text{ mm}$ and strip width $w_r=0.105 \text{ mm}$. The CPW rat-race ring features the following radius: $r_1=1.6 \text{ mm}$, $r_2=2.1 \text{ mm}$, $r_3=2.205 \text{ mm}$ and $r_4=2.705 \text{ mm}$.

An input signal is fed from port 1 resulting in two equal amplitude in-phase signals at ports 2 and 3. Port 4 is isolated in this case. Therefore, ports 2 and 3 are used to feed two identical linear 14 crossed slot sub arrays while port 4 is connected to the ground through the impedance of 120Ω . Although there are two sub-arrays, we model likewise a modified CPW rat-race that does not contain port 4 (Fig. 13) in order to investigate its role and necessity in rat-race coupler.

The imbalance between S-parameters (magnitudes ($|S_{ij}|$) and phases ($\angle S_{ij}$) of S_{21} and S_{31} S scattering (S-) parameters referring Port 2 and Port 3 of both CPW rat-race coupler and modified CPW rat-race coupler for feeding left and right subarrays) for frequency range from 24 GHz to 28 GHz is presented in Fig. 14. Analyzing shown results, it can see that maximum difference between magnitudes of S_{21} and S_{31} parameters of rat-race coupler with 4 ports is less than 0.5 dB while the maximum variation between their phases is less than 2.5 degrees. Modified rat-race coupler enables equal amplitude in-phase signals at ports 2 and 3 concerning results shown in Fig. 14.

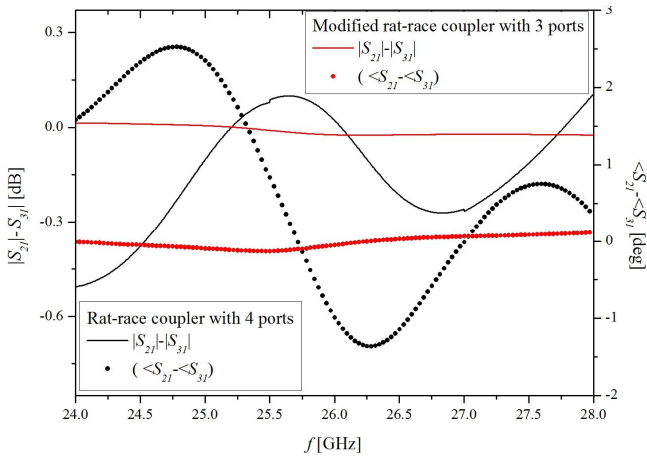


Fig. 14. The difference between insertion losses calculated at ports 2 and 3 of CPW rat-race coupler and of modified CPW rat-race coupler. S-parameters are normalized to the impedance Z_p (120 Ω).

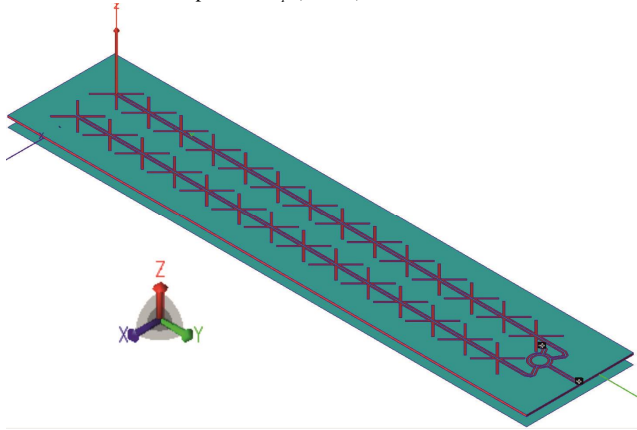


Fig. 15. 2D CPW-fed crossed slot array fed by CPW rat race coupler.

It can be concluded that proposed both CPW rat-race coupler and modified CPW rat-race coupler provide necessary feeding for both subarrays for range between 24-28 GHz. Therefore they are employed to feed 2D crossed slots array (Fig. 15). 2D crossed slots array and CPW rat-race coupler are both situated on the substrate with dimensions 145 mm x 29.8 mm x 0.508mm while the equal reflector plate is at the distance $\lambda_0/4$.

The radiation patterns of 2D CPW-fed crossed slots array fed by CPW rat-race coupler with 4 ports is presented in Fig. 16. The maximum gain at the center frequency f_c is 19.6 dBi at the position $\theta=90^\circ$. At the lower edge frequency 25.6 GHz, the maximum gain is 18.8 dBi at the position $\theta=89^\circ$. At the higher edge frequency 26.8 GHz, the maximum gain is 18.65 dBi at the position $\theta=93^\circ$. SLS is 12.5 dB at the center frequency f_c and 10 dB at the both edge frequencies.

However, the radiation pattern of the 2D CPW-fed crossed slots array fed by modified CPW rat-race coupler with 3 ports has less gain for all considered frequencies (Fig. 17): 18.85 dBi at the center frequency f_c , 18.4 dBi at the lower edge frequency 25.6 GHz and 18.6 dBi at the higher edge frequency 26.6 GHz. The maximum gain spreads from $\theta=89^\circ$ for the lower edge frequency 25.6 GHz, through $\theta=90^\circ$ for f_c to $\theta=93^\circ$ for the higher edge frequency 26.6 GHz. SLS is 12 dB at the center frequency f_c and it drops to 10 dB at the edge frequencies.

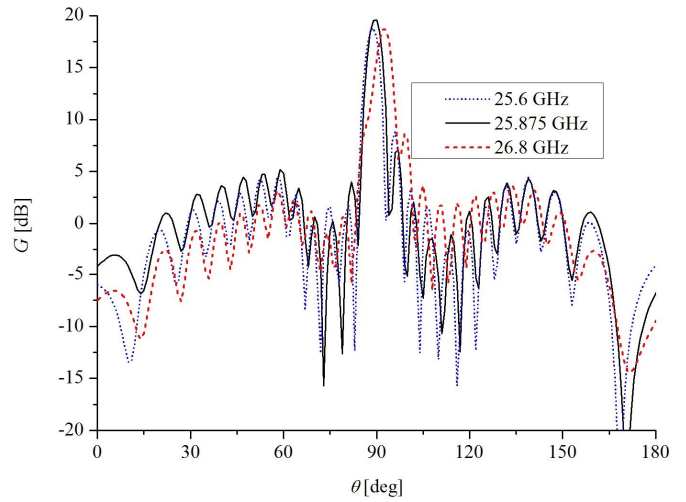


Fig. 16. Radiation patterns in the yOz plane ($\phi=90^\circ$) of the 2D CPW-fed crossed slots array fed by CPW rat-race coupler.

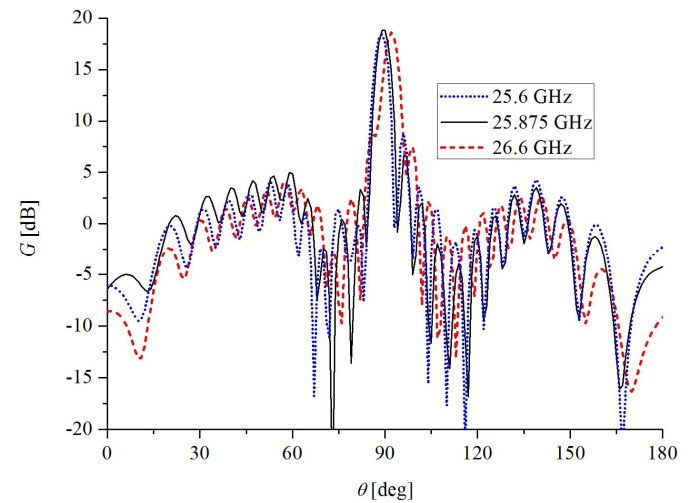


Fig. 17. Radiation patterns in the yOz plane ($\phi=90^\circ$) of the 2D CPW-fed crossed slots array fed by modified CPW rat-race coupler.

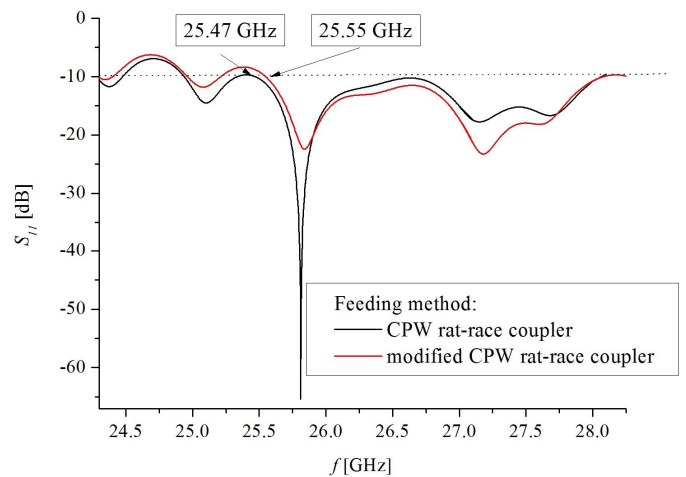


Fig. 18. S_{11} parameter versus frequency of the 2D CPW-fed crossed slots array fed by CPW rat-race coupler and by modified CPW rat-race coupler. S-parameter is normalized to the impedance $Z_p=120 \Omega$.

The S_{11} parameter of 2D CPW-fed crossed slots array fed by CPW rat-race coupler and by modified CPW rat-race coupler is shown in Fig. 18.

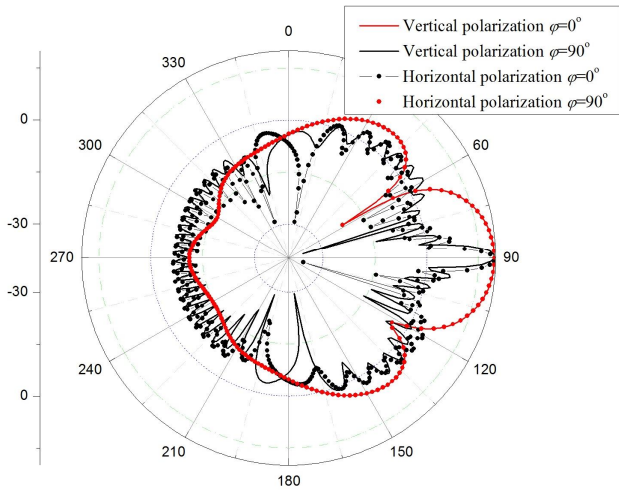


Fig. 19. Radiation pattern of the 2D CPW-fed crossed slots array fed by CPW rat-race coupler in X-Z ($\varphi=0^\circ$) and Y-Z ($\varphi=90^\circ$) plane at the frequency f_c .

TABLE I

THE GAIN AND BANDWIDTH DEFINED BY RADIATION CHARACTERISTICS AND BY S_{11} PARAMETERS OF THE PROPOSED LINEAR AND 2D CPW-FED CROSSED SLOT ARRAYS

Array and feed	Gain [dBi]	Bandwidth by radiation pattern/by S_{11} [GHz]
14 slots	18.7	0.77/1.14
2x14 slots by 2 generators	20.7	0.9/1.1
2x14 slots by CPW T-junction	18.45	0.96/>2.51
2x14 slots by CPW rat-race	19.6	1.2/>2.53
2x14 slots by modified CPW rat-race	18.85	1/>2.45

It is less than -10 dB for frequency above 25.47 GHz for feeding by CPW rat-race and for frequency above 25.55 GHz when the modified CPW rat-race is used. It can notice that 2D CPW-fed crossed slots array fed by CPW rat-race coupler has the biggest frequency range defined by both criteria: by satisfying radiation characteristics and by condition that $S_{11} < -10$ dB. Also, the latter criterion gives greater frequency range than the former.

Although the single crossed slot antenna is dual polarized [9], the simulated radiation patterns in both X-Z and Y-Z planes for two orthogonal polarizations (vertical and horizontal) of the 2D CPW-fed crossed slots array fed by CPW rat-race coupler are presented in Fig. 19. It can conclude that it is also a dual polarized antenna.

All obtained results of comparison between feeding methods and antenna arrays are shown in Table I.

IV. CONCLUSION

This paper presents the antenna arrays of crossed slot antenna fed by CPW transmission line. The first proposed antenna is a linear array of 14 crossed slots that features with gain of 18.7 dBi at the center frequency f_c . It has the satisfying radiation patterns from the frequency range from 25.6 GHz to 26.37 GHz. Also, its S_{11} parameter is less than -10 dB for the frequencies between 25.6 GHz to 26.74 GHz.

After that we investigate feeding networks for two planar arrays of 14 crossed slots and employ four feeding methods. First method is two generators that enable great gain of 20.7 dBi of the proposed 2D crossed slot array. The gain and SLS have the allowed variation for the frequency range from 25.5 GHz to 26.4 GHz. Moreover, S_{11} parameter stays below -10 dB for the frequencies between 25.5 GHz to 26.6 GHz.

CPW T-junction, CPW rat-race coupler and modified CPW rat-race coupler are proposed. The comparison among the simulated results of investigated three feeding methods gives the advantage to the CPW rat-race coupler. The gain is the greatest when CPW rat-race coupler is used (19.6 dBi). Additionally, the radiation pattern keeps the satisfying gain and SLS values in the largest frequency range when 2D array is fed by CPW rat-race coupler (25.6 GHz - 26.8 GHz). However, S_{11} parameter of 2D array fed by CPW rat-race coupler is less than -10 dB for the similar frequency range above 25.47 GHz as S_{11} parameter of 2D array fed by CPW T-junction and S_{11} parameter of 2D array fed by modified CPW rat-race coupler.

ACKNOWLEDGMENT

This work was supported by the Ministry of Education, Science and Technological Development of the Republic Serbia. The authors would like to thank prof. Natasa Males Ilic and dr. Aleksandar Atanaskovic for their useful suggestions concerning the rat-race coupler modelling.

REFERENCES

- [1] V. Milosevic, B. Jokanovic, O. Boric-Lubecke, V. M. Lubecke, "Key Microwave and Millimeter Wave Technologies for 5G Radio," in *Powering the Internet of Things with 5G Networks*, V. Mohanan, R. Budiartu, I. Aldmour, Eds. IGI Global, July 2017,
- [2] Y. Chang, Y. Jiao, L. Zhang, G. Chen and X. Qiu, "A K-band series-fed microstrip array antenna with low sidelobe for anticollision radar application," 2017 Sixth Asia-Pacific Conference on Antennas and Propagation (APCAP), pp. 1-3, 2017.
- [3] S. J. Chen, W. Withayachumnankul, Y. Monnai and C. Fumeaux, "Linear Series-Fed Patch Array with Dual Circular Polarization or Arbitrary Linear Polarization," 2019 International Conference on Electromagnetics in Advanced Applications (ICEAA), pp. 0365-0369, 2019.
- [4] D.. Guan, C. Ding, Z. Qian, Y. Zhang, W. Cao and E. Dutkiewicz, "An SIW-Based Large-Scale Corporate-Feed Array Antenna," in *IEEE Transactions on Antennas and Propagation*, vol. 63, no. 7, pp. 2969-2976, July 2015.
- [5] A. G. Toshev, "Synthesized shaped beam flat array antenna for digital beam-forming radar applications, utilizing printed technology," 2017 IEEE International Conference on Microwaves, Antennas, Communications and Electronic Systems (COMCAS), pp. 1-4, 2017.
- [6] W. Hong, K. Baek, S. Ko "Millimeter-Wave 5G Antennas for Smartphones: Overview and Experimental Demonstration," *IEEE Trans. Antennas Propag.*, vol. 65, no. 12, pp. 6250 ó 6261, December 2017.
- [7] M. Miliji , B. Jokanovi , "High-gain Slot Antenna Arrays for 5G and Radar Applications," 2019 27th Telecommunications Forum (TELFOR), Belgrade, Serbia, pp. 381-384, November, 26-27, 2019.
- [8] M. Milijic, B. Jokanovic, "Advanced High-Gain Slot Antenna Arrays for 5G and Radar Applications," *Telfor Journal*, Vol.13 No.1 (2021), pp. 29-34.
- [9] M. Milijic, B. Jokanovic, L. Lazovic, "Comparative Analysis of K-band Crossed Slot and Crossed Dipole Antennas," 15th Intern. Conf. TELSIS, Nis, Serbia, pp. 9-12, October 20-22, 2021.
- [10] WIPL-D Pro CAD 2020.
- [11] A. Omar, N. Dib and A. AlBdrashiny, "Miniaturized CPW Rat-Race Coupler Using the Superformula," 2018 18th Intern. Sym. on Antenna Technology and Applied Electromagnetics (ANTEM), pp. 1-2, 2018.

Cost-Effective Standing Wave Ratio Meter

Ana Đ. Ćupurdija, *Member, IEEE*, and Slobodan V. Savić, *Member, IEEE*

Abstract—This paper presents a cost-effective and compact realization of a standing wave ratio (SWR) meter designed with commercially available low-cost components. The SWR meter was tested by measuring voltage standing wave (VSW) and complex impedance with slotted coaxial transmission line, and both results were in good agreement with the simulated circuit results and measurements done on professional equipment - HP SWR meter and vector network analyzer (VNA). The proposed system presents an affordable and precise SWR meter, but also a valuable educational platform for understanding electromagnetic field distribution along transmission lines.

Index Terms—complex impedance; electromagnetic waves; measuring instruments; slotted coaxial transmission line; standing wave ratio.

I. INTRODUCTION

SINCE their discovery, electromagnetic (EM) waves never lost their significance and the functionality of many modern devices would be unimaginable without them. These devices include mobile phones, laptops, wireless devices, radar systems, etc. Bluetooth and the internet would not exist were it not for EM waves. Therefore, today they represent an irreplaceable means for information transmission and a physical phenomenon whose number of applications will only increase in the future [1].

However, when propagating through different mediums (air, water, dielectrics, ionosphere, etc.) or when guided with different guiding-structures (transmission lines or waveguides), EM waves form certain patterns [2] that are not always quite intuitive and can be hard to visualize, even for an experienced RF engineer. An excellent starting point for analyzing this phenomenon is the graphical representation of standing waves along transmission lines (TLs).

To provide a way for students to better understand the concepts of electromagnetic field distribution, we have designed and realized a compact and affordable standing wave ratio (SWR) meter. This prototype, along with slotted coaxial TL, presents a working principle of SWR measurements in a simple and easy-to-understand manner and also provides relatively precise measuring equipment.

The rest of the paper is organized as follows. In the second chapter, the theory of standing waves is briefly introduced, and the requirements for a functional SWR meter are

Ana Đ. Ćupurdija is with the School of Electrical Engineering, University of Belgrade, 73 Bulevar kralja Aleksandra, 11020 Belgrade, Serbia, and with the Vlatocom Institute of High Technologies, Milutin Milanković Blvd. 5, Belgrade, Serbia (e-mail: anacupurdija96@gmail.com).

Slobodan V. Savić is with the the School of Electrical Engineering, University of Belgrade, 73 Bulevar kralja Aleksandra, 11020 Belgrade, Serbia (e-mail: ssavic@etf.bg.ac.rs).

discussed. In the third chapter, starting SWR meter model and its simulation results obtained via TINA simulator [3] are shown. In the fourth chapter, the design and realization of the SWR meter are presented, along with schematics and printed circuit board (PCB) layout. In the fifth chapter, voltage standing wave (VSW) measurements were done for a transmission line closed with different loads, and these results are compared with the results obtained with a professional SWR meter. In the sixth chapter, unknown load impedances are estimated from the SWR measurements and compared to the results obtained with AWR Design Environment [4] and vector network analyzer (VNA) measurements. Finally, in the seventh chapter, conclusions are drawn.

II. STANDING WAVES MEASUREMENT THEORY

Two-wire transmission line represents a pair of conductors carrying an EM wave. The theory of EM propagation along TLs is explained in detail in [2, 5].

When exciting a TL with a signal from a generator connected at its one end, voltage and current waves are formed along the TLs axis. In the steady state, when all excitations and all responses are single-frequency signals, on the transmission-line there are, generally, two waves traveling in opposite directions. These waves are progressive (traveling) waves, and their superposition forms the standing wave. The effective (rms) value of the standing wave is a function of the generator's power, the complex impedance of a load which ends TL on the other end, the characteristic impedance of the TL, and it (generally) changes along the TLs axis. When the TL is opened on its other end, all of the incident power is reflected from the open end. When the TL is ended with a lossy load, some of the excited power is dissipated in the load, making the reflected wave have less energy than the incident wave.

The parameter that integrally describes standing wave is SWR, defined as

$$SWR = \frac{U_{\max}}{U_{\min}}, \quad (1)$$

where U_{\max} and U_{\min} are the maximum and the minimum effective value of the VSW along TL's axis, respectively. The standing wave ratio can be in the range $[1, \infty)$. If SWR equals one, the load is matched to the TL, and there is no reflection. If SWR tends to infinity, all the energy of the incident wave is reflected.

One way to measure SWR is to use slotted coaxial TL and measure EM field or voltage along TL's slot with a short probe. The probe should be long enough to detect high enough voltage, and short enough not to (locally disturb) the

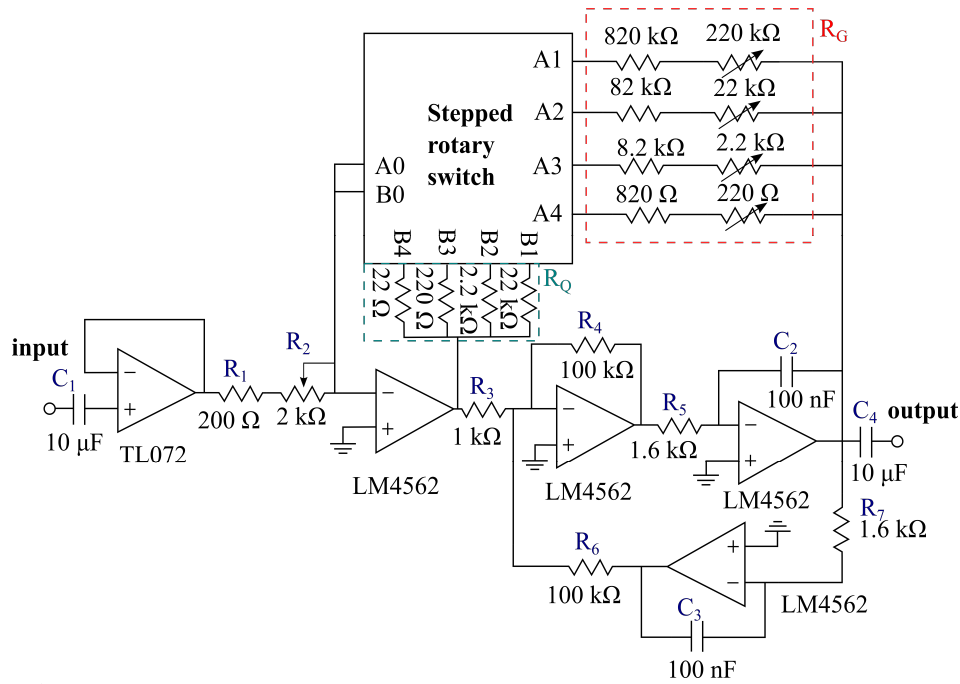


Fig. 1. SWR meter schematics.

EM field. The voltage measured with this probe is proportional to the electric field in the slotted coaxial TL and is connected to the square-law diode detector [6]. This diode is usually a germanium diode, which works in the quadrature region of the I-V (current-voltage) characteristics. Therefore, the signal obtained with this diode detector is proportional to the square of the VSW effective value. This signal is then further processed by the SWR meter. Keeping all of this in mind, we can define SWR meter functionalities and parameters of interest. Also, please note that in the measurement set up that we are using, shown in Fig. 5, incident voltage (field) is modulated with a signal of a fixed, preferably low, frequency (i.e., around 1 kHz), that represents an envelope of the high-frequency signal that form the standing wave. The incident signal is amplitude modulated because when working with an unmodulated signal, the output of the diode detector would be a DC voltage which is generally susceptible to high measurement errors due to the existence of the DC offset in systems. Since the amplitudes of the measured unmodulated signal are relatively small (about 1 mV), even a small DC offset could introduce significant measurement errors. By measuring the effective value of the detected 1 kHz envelope, the effective value of the high-frequency signal could also be measured. Expected values for the signals at the output of the probe are in the range 1-10 mV, so the designed SWR meter should have a significant gain. Based on all of this, we decided to design the SWR meter as an active bandpass filter, with the center frequency around 1 kHz. The proposed design has four gain stages (times 1, 10, 100, and 1000), while also having an option to fine-tune gain to any value in these ranges. Finally, the Q factor of the filter needs to be set accordingly, so the

circuit can filter unwanted harmonics and harmonic components, but also not be too selective. The Q factor needs to be independent of the set gain, and the gain and the Q factor of the system should be independent of impedances connected at its input and output.

III. SIMULATION RESULTS

The main part of the circuit (bandpass active filter) was designed starting from [7] and by using the operational amplifier LM4562. This chip is made by Texas Instruments, so simulation of the circuit was done in their TINA simulator [4]. The schematics used for simulation are shown in Fig. 1, while omitting the stepped rotary switch. This schematic is the main building block for the SWR meter.

The circuit shown in Fig. 1 is excited with an AC generator at 1 kHz. The gain is set with resistors R_1 , R_2 and R_G , and is given by the formula

$$G = \frac{R_G}{R_1 + R_2}. \quad (2)$$

The Q factor is set with the resistors R_G and R_Q , given by the formula

$$Q = \frac{R_G}{R_Q}. \quad (3)$$

In the mentioned configuration, without the stepped rotary switch, the Q factor depends on the gain (since they have a common factor of the resistor R_G). This is not a desirable feature, hence, stepped rotary switch was introduced in the PCB design step. The circuit is intended to operate in a single-frequency mode, just like the professional HP SWR

meter, which is used for comparison. This central bandpass frequency is set with capacitor C_2 and resistor R_5 (aka C_3 and R_7), given with the formula

$$f_c = \frac{1}{2\pi R_5 C_2} \quad (4)$$

Simulation results are shown in Table I, for four gain configurations. The resistor R_Q was changed along with R_G , so that the Q factor is constant, and is set to be around $Q=45$. These results confirmed that the designed circuit works as expected, so we proceeded with the board design and fabrication.

TABLE I
GAIN SIMULATION RESULTS

Resistor R_G	1 k Ω	10 k Ω	100 k Ω	1 M Ω
Theoretical gain	1	10	100	1000
Simulated gain	1.13	10.13	100.12	993.76

IV. SWR METER PROTOTYPE

Based on the schematics in Fig. 1, PCB layout was made and is shown in Fig. 2. The purpose of the buffer at the input stage is to make the input impedance of the circuit independent from the gain and Q factor. The output stage of the meter is not buffered. When the output current is below the maximum value stated in the datasheet (26 mA), practically there is no distortion in the output voltage. In order not to exceed the current limit, in the worst case scenario for output voltage of 1 V, the load impedance must be greater than 40 Ω , which is well below input impedances for all commercial multimeters.

The resistor R_2 is a potentiometer, so the gain can be fine-tuned to any value in the predefined ranges. Predefined ranges of 1, 10, 100, and 1000 are set using the stepped rotary switch, with three pins and four positions. This switch changes the resistors used for setting the gain (R_G in Fig. 1). Also, using this switch, the resistors used for setting the Q factor are simultaneously switched when setting the gain, so the Q factor would stay constant when the resistor R_G changes. For the measurements shown in Section V, the Q factor is set around $Q=45$.

The branches with resistors used for gain setting contain one fixed resistor and one trimmer potentiometer. This way, even with component tolerances, the gain can be fine-tuned to exactly match the predefined values (1, 10, 100, and 1000). The made prototype has its stage for power supply (converting the AC voltage of 230V into ± 5 V DC needed for the operational amplifiers) and also has added overcurrent protection, in a form of a fuse.

The final prototype is shown in Figs. 3 and 4, where it can be seen that the final prototype is compact and practical to use. With this design, we satisfied all of our requirements for a functional SWR meter, so we proceeded with the measurements.

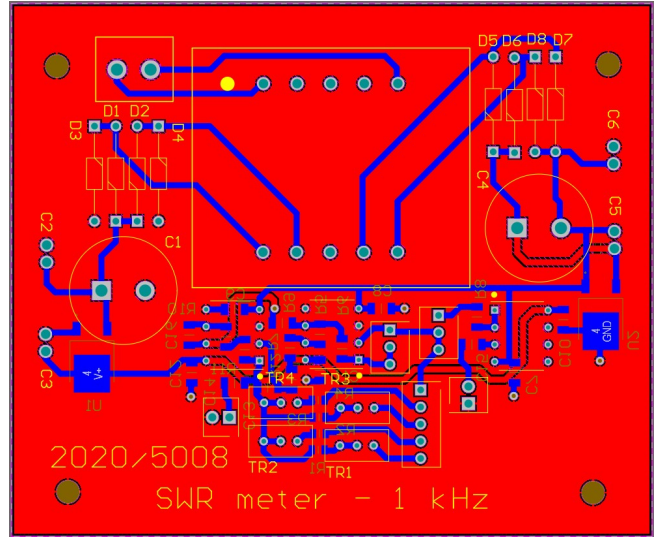


Fig. 2. Printed circuit board layout of the SWR meter.

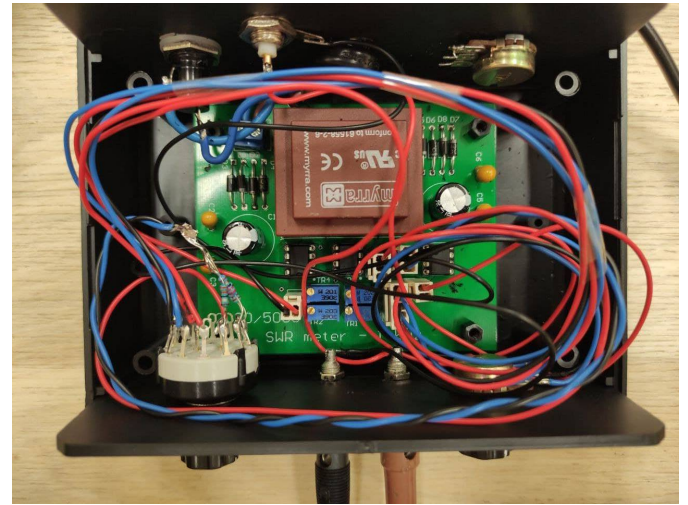


Fig. 3. The prototype of the SWR meter.

V. MEASUREMENTS ON A SLOTTED COAXIAL TRANSMISSION LINE

The first measurement to test the functionality of the SWR meter was made with an oscilloscope, where the input and the output voltages are observed to set the desired gain to 1, 10, 100, and 1000 with trimmer resistors. The effective value of input voltage is set so that the output can be easily visible on the oscilloscope for a given measurement, but also to prevent the operational amplifiers from entering the saturation. The gain was then fine-tuned to the wanted values with trimmer resistors.

After setting the gains to the desired values, measurements on the TL were done. The used TL is a slotted coaxial TL having $Z_c = 50 \Omega$ characteristic impedance with a probe that could be moved longitudinally along TL's axis. This way the effective value of VSW is measured along TL's axis. The slotted TL we are using has a ruler along its axis, so we will use this ruler for measuring distance along TL's axis. The probe position is controlled with a mechanical knob. The line was excited with a sine wave at 1.4 GHz, modulated with a sine at 900 Hz. This signal was generated by a

software-defined radio (SDR) device. The frequency of the envelope at 900 Hz was chosen because, due to the component tolerances, the central frequency of the filter was not exactly 1 kHz. Central frequency was determined by changing the envelope frequency and observing when the maximal gain occurs.

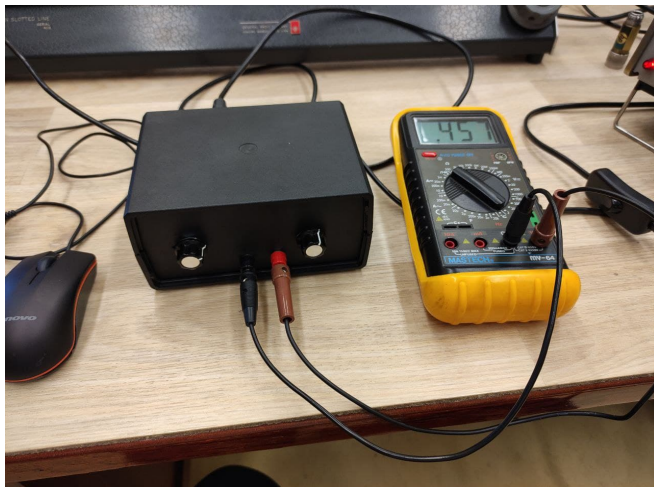


Fig. 4. The prototype of the SWR meter is enclosed in a box and connected to the voltmeter.

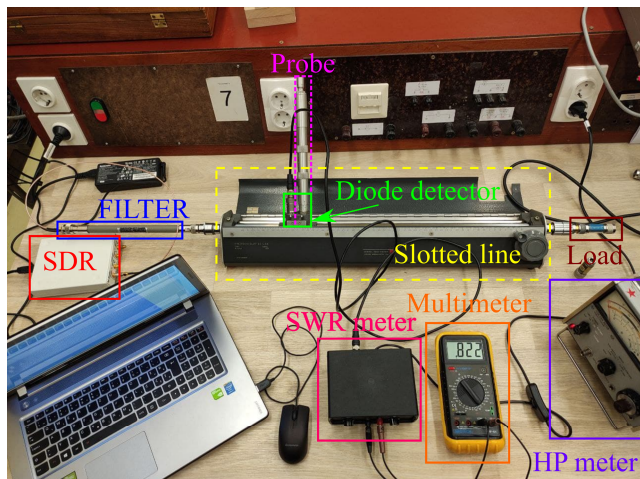


Fig. 5. Complete measurement setup.

To suppress any unwanted signal, at the input of the TL, a coaxial filter was placed, with a cut-off frequency at 2.2 GHz. The effective value of the output voltage of the realized SWR meter is measured with a multimeter, as shown in Figs. 4 and 5. The measurements were done by moving the probe in steps of 5 mm and measuring the VSW effective value in 81 data points. The measurements were done in the distance range from 15 cm to 55 cm at the TL ruler. The same procedure was done when TL was opened at its other end, and when it was terminated with the 6 dB and with the 10 dB loads. These loads are realized as coaxial (6 dB and 10 dB) attenuators, opened at their second end. The SWR meter gain for the measurements is set so that the peak of the VSW corresponds to the effective value of 1 V measured with the multimeter.

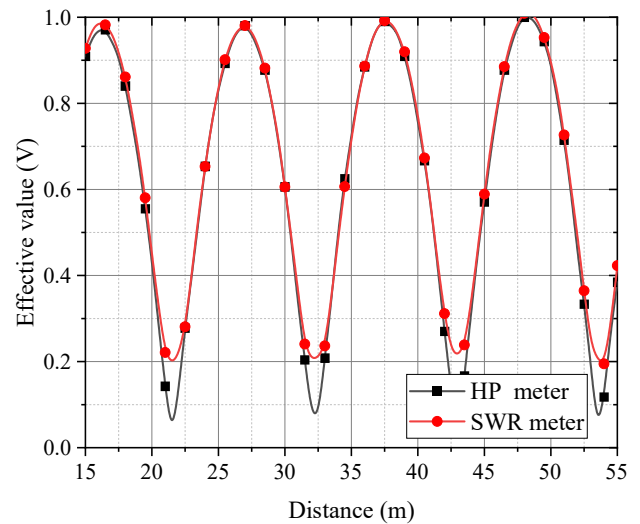


Fig. 6. Comparison of the VSW measurement obtained with designed and professional SWR meter for open-ended transmission line.

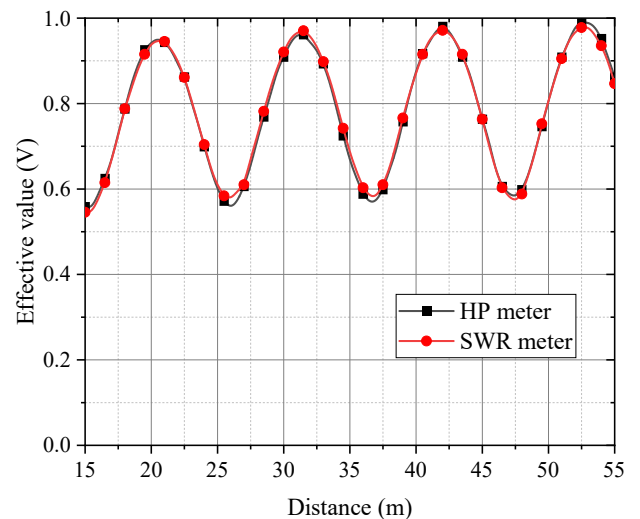


Fig. 7. Comparison of the VSW measurement obtained with designed and professional SWR meter when the transmission line is closed with the 6 dB load.

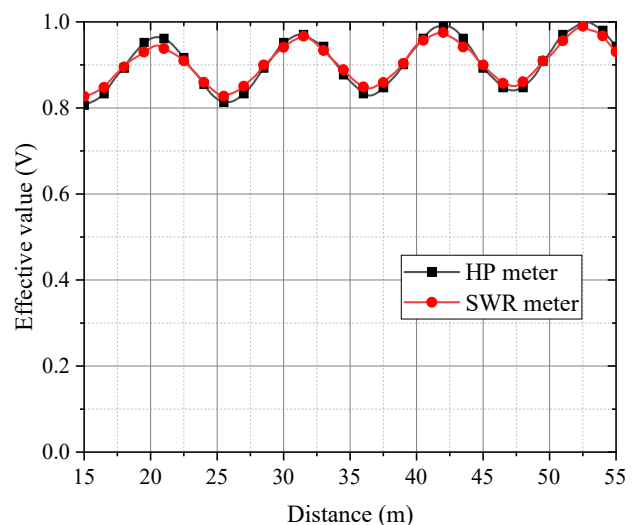


Fig. 8. Comparison of the VSW measurement obtained with designed and professional SWR meter when the transmission line is closed with the 10 dB load.

For the obtained results to be double-checked, the same set of measurements was done with the professional Hewlett-Packard 415E SWR meter. The entire measurement setup is shown in Fig. 5. The obtained VSW curves for the case of the unloaded TL are shown in Fig. 6, while the obtained curves for cases of 6 dB and 10 dB loads are shown in Figs. 7 and 8, respectively. In the case of the unloaded line, the proposed SWR meter does not have such deep minimums as the professional one. Additionally, for this case, VSW should be equal to zero at its minimum. This is not being the case in Fig. 6 due to, among other, finite number of measuring points along TL's axis. Nevertheless, these two sets of results are in good agreement, and even better when TL is closed with loads (Figs. 7 and 8).

VI. LOAD IMPEDANCE CALCULATION

The impedances of used loads (6 dB and 10 dB) are firstly estimated based on the fact that these loads are matched coaxial attenuators opened at their second end. Based on this, a simple model for the calculation of their input impedance is assembled in the AWR Design Environment, as shown in Fig. 9. The load which complex impedance we want to measure, labeled as "LOAD" at Fig. 5, is modeled as two short TLs with ideal (matched) attenuator between them. The same model is used for 10 dB load, with a loss parameter of the ATTEN element from Fig. 9 set to 10 dB. The length of used short TLs is estimated experimentally.

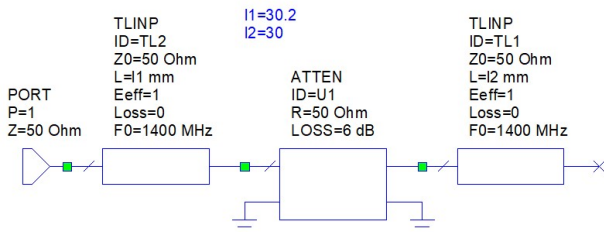


Fig. 9. The simple model of used loads made in the AWR Design Environment.

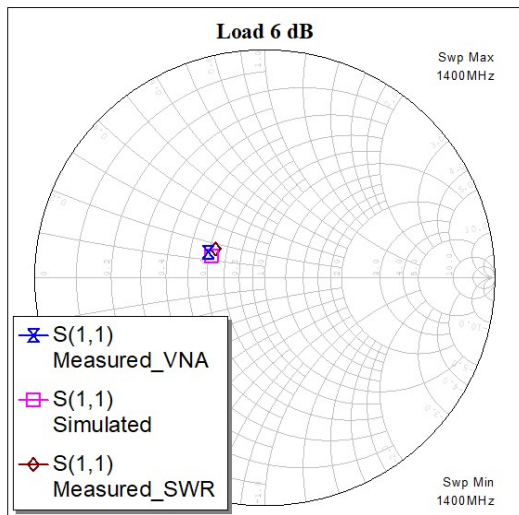


Fig. 10. Smith chart for the 6 dB load.

From the given SWR measurements, using the Smith diagram, load impedances are calculated as described in [5, 8]

and compared to the impedances of the loads obtained via simulation and via measurements done on the N5227a Agilent VNA. The results are shown in Figs. 10 and 11 for 6 dB and 10 dB loads, respectively. From these figures, it can be noticed that the obtained results of the load impedances are in excellent agreement for all three sets of results. Therefore, we conclude that the designed SWR meter can be used for the precise determination of unknown impedances.

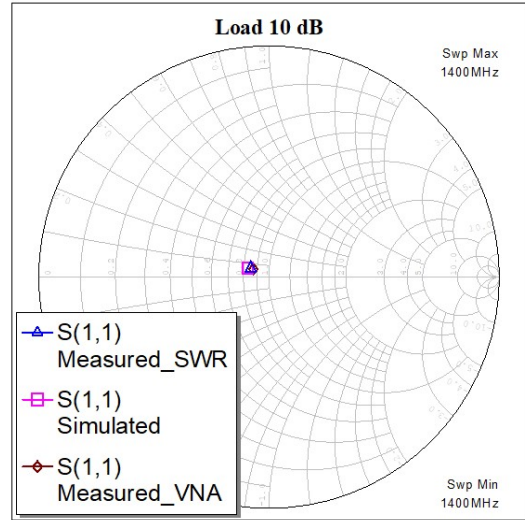


Fig. 11. Smith chart for the 10 dB load.

VII. CONCLUSION

A compact and affordable prototype for the SWR meter was proposed and realized. Simulation and measurement results are proven to fit well. The realized circuit acts as an active filter with four gain stages (1, 10, 100, and 1000), and the gain can also be fine-tuned to any value in these ranges.

Standing wave ratio measurements were done on a slotted coaxial transmission line for two different loads, and measurements obtained with the designed SWR meter are compared to those obtained with the professional HP SWR. These two sets of measurements are in good agreement. From the measured standing wave curves, load impedances are calculated and they are in excellent agreement with the results obtained with AWR Design Environment and professional VNA.

The realized device can be used to better understand and visualize the EM waves distribution on TLs but also could be a usable piece of equipment for microwave laboratories which is a good alternative to much more expensive professional equipment. Further improvements would include adding a tunable Q factor functionality to the device. This will be part of the authors' further efforts.

ACKNOWLEDGMENT

The authors acknowledge funding provided by the School of Electrical Engineering, University of Belgrade, through the grants by the Ministry of Education, Science, and Technological Development of the Republic of Serbia, and Vlatocom Institute, through project "The Development of Over-the-Horizon Radar in HF band HF-OTHR2".

REFERENCES

- [1] R. K. Amineh, "Applications of Electromagnetic Waves: Present and Future," *Electronics*, vol. 9, no. 5, pp. 808-811, May 2020.
- [2] R. E. Collin, *Field Theory of Guided Waves*, 2 ed. New York: Wiley-IEEE Press, 1991.
- [3] TINA Simulator v9.3. Texas Instruments, <https://www.ti.com/tool/TINA-TI>.
- [4] AWR Design Environment Cadence, https://www.cadence.com/en_US/home/tools/system-analysis/rf-microwave-design/awr-design-environment-platform.html.
- [5] A. R. Đorđević and D. V. Tošić, *Microwave Technique (in Serbian)*. Belgrade, Serbia: Academic Mind, 2010.
- [6] J. B. Hagen, *Radio-Frequency Electronics: Circuits and Applications*. New York, USA: Cambridge University Press, 2009.
- [7] A. Devices, "LT1814 datasheet," Available: <https://www.analog.com/en/products/lt1814.html>.
- [8] M. Golio and J. Golio, *RF and Microwave Circuits, Measurements, and Modeling*. Florida, USA: CRC Press, 2018.

Automatizacija određivanja nivoa EM polja radio-difuznih predajnika na osnovu ITU-R P.1546 metode za visine h_1 manje od 10 m

Miloš Radojković, Zlatica Marinković, *Senior Member, IEEE*

Apstrakt—U ovom radu predložen je metod za određivanje nivoa EM polja iz preporuke ITU R-1546 za očekivani nivo elektromagnetnog polja koji potiče od radiodifuznih predajnika i visine h_1 manje od 10 metara. Predloženi metod je baziran na primeni veštačkih neuronskih mreža i omogućava efikasno određivanje nivoa polja za frekvencije do 4000MHz i visine h_1 manje od 10 metara. Tačnost metoda prikazana je na primerima krivih koje se odnose na frekvencije i vrednosti h_1 koji nisu korišćene u procesu obučavanja neuronske mreže.

Ključne reči—ITU-R P.1546, nivo elektromagnetnog polja, radio-difuzni predajnik, veštačke neuronske mreže.

I. UVOD

Radiodifuzne komunikacije su komunikacije tipa tačka-oblast i njihova primena je veoma česta (radio i televizijski predajnici, bazne stanice mobilnih sistema i sl.). Jedan od nezaobilaznih koraka prilikom projektovanja radiodifuznog sistema jeste određivanje zone pokrivanja. Zona pokrivanja predstavlja oblast u kojoj je nivo elektromagnetnog (EM) polja veći od vrednosti definisane zahtevima razmatranog sistema i određen je daljinom od predajnika na kojoj je nivo EM polja veći od zadate vrednosti.

Zona pokrivanja je određena u nekoliko pravaca – azimuta (obično 36 pravaca sa korakom od po 10° ili 120 pravaca sa korakom od po 3° , što zavisi od jačine predajnika). Postoje različite metode za određivanje zone pokrivanja. Najčešće se koristi statistički metod definisan u preporuci ITU-R P.1546 [1]. Preporuka ITU-R P.1546 daje postupak određivanja nivoa polja za zemaljske radio-difuzne servise u frekvencijskom opsegu od 30 MHz do 4000 MHz. Preporuka se bazira na empirijskim krivama (dostupnih i tabelarno) za zavisnost očekivanog nivoa polja od rastojanja za različite vrednosti parametra koji opisuje karakteristike terena. Imajući u vidu da je preporuka data za fiksne vrednosti frekvencija, visine h_1 i daljine d , ukoliko je potrebno izvršiti proračun EM polja za vrednosti koje nisu date u preporuci ITU-R P.1546 potrebno je izvršiti veliki broj interpolacija.

U ovom radu je predložen je metod za očitavanje krivih za očekivani nivo EM polja baziran na veštačkim neuronskim mrežama. Veštačke neuronske mreže su izabrane zahvaljujući njihovim odličnim interpolacionim sposobnostima, zbog čega su i široko primenjene u oblasti mikrotalasa [2]-[11]. Neuronske mreže su već primenjivane

za očitavanje krivih za očekivani nivo polja po pomenutoj preporuci i ranijim verzijama [2]-[6], a u ovom radu se po prvi put neuronske mreže primenjuju za očitavanje vrednosti nivoa EM polja za visine h_1 manje od 10 metara.

U Sekciji II najpre je kratko opisan postupak određivanja nivoa polja na osnovu preporuke ITU-R P-1546. Predloženi model za očitavanje krivih za vrednosti h_1 manje od 10 metara objašnjen je u Sekciji III. Dobijeni rezultati primenom razvijenog modela prikazani su u Sekciji IV. Izvedeni zaključci dati su u Sekciji V.

II. PREPORUKA ITU-R P-1546

Preporuka ITU-R P.1546 se zasniva na familiji krivih koje su date kao očekivane vrednosti intenziteta polja u dB μ V/m na visini 10m iznad tla (usvojena prosečna visina prijemne antene za radio-difuzni prijemnik), za signal emitovan predajnikom snage 1 kW izračen pomoću polutalasnog dipola (dobitak 0 dBd), u funkciji rastojanja.

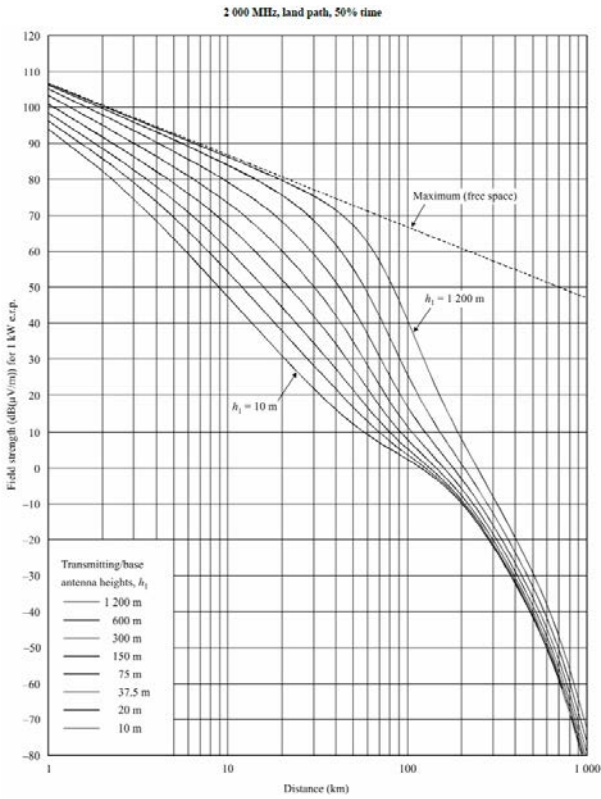
Krive su date posebno za kopno i posebno za more, a u preporuci je opisan i način proračuna u slučaju kombinovanog terena. Za oba tipa sredine date su krive očekivanog intenziteta polja za frekvencije 100 MHz, 600 MHz i 2000 MHz i to za 50%, 10% i 1% vremena i za 50% lokacija u oblasti površine 500 \times 500 m². Kao primer na Sl. 1 prikazane su krive za očekivani intenzitet polja na frekvenciji 2000 MHz za kopno. Parametar na krivama je vrednost EM polja u dB μ V/m za visine h_1 u rasponu od 10 do 1200 m (diskretne vrednosti 10 m, 20 m, 37.5 m, 75 m, 150 m, 300 m, 600 m i 1200 m) i daljine d do 1000 km. Parametar h_1 je za rastojanja od predajnika veća od 15 km jednak efektivnoj visini terena h_{eff} (visinska razlika između visine centra antene u odnosu na nivo mora i srednje nadmorske visine na rastojanju od 3 km do 15 km od predajnika). Za rastojanja d manja od 15 km, parametar h_1 predstavlja visinsku razliku između visine centra antene u odnosu na nivo mora i srednje nadmorske visine na rastojanju od $0.2d$ do d od predajnika. U slučaju da je poznata samo efektivna visina antene, a ne i detaljne informacije o terenu, za rastojanja do 3 km parametar h_1 je jednak visini antene iznad tla h_a . Za rastojanja veća od 3km za određivanje visine h_1 koristi se sledeći izraz:

$$h_1 = h_a + \frac{(h_{eff} - h_a)(d - 3)}{12} \quad (1)$$

Imajući u vidu da su krive date za diskretne vrednosti h_1 , prilikom proračuna neophodno je vršiti interpolaciju za konkretnu vrednost h_1 na sledeći način:

Miloš Radojković – Energoprojekt Entel, Bulevar Mihajla Pupina 12, Beograd 11070, Srbija (e-mail: milosradojkovic89@gmail.com).

Zlatica Marinković - Elektronski fakultet u Nišu, Univerzitet u Nišu, Aleksandra Medvedeva 14, 18000 Niš, Srbija (e-mail: zlatica.marinkovic@elfak.ni.ac.rs).



Sl. 1. Krive za očekivani intenzitet polja na 2000 MHz za kopno po preporuci ITU-R P-1456.

$$E_o = E_{inf} + (E_{sup} - E_{inf}) \frac{\log(h_1 / h_{inf})}{\log(h_{sup} / h_{inf})} \quad (2)$$

gde je: E_{inf} nivo polja za zadato rastojanje očitano sa krive koja se odnosi na prvu manju tabelarnu vrednost visine h_1 , h_{inf} , a E_{sup} nivo polja za zadato rastojanje očitano sa krive koja se odnosi na prvu veću tabelarnu vrednost visine h_1 , h_{sup} .

Za određivanje nivoa polja na proizvoljnom rastojanju d , (u opsegu od 1km do 1000km) koristi se sledeći izraz

$$E_o = E_{inf} + (E_{sup} - E_{inf}) \frac{\log(d / d_{inf})}{\log(d_{sup} / d_{inf})} \quad (3)$$

gde je E_{inf} očitana vrednost polja za d_{inf} , prvu tabuliranu vrednost rastojanja manju od d , E_{sup} očitana vrednost polja za d_{sup} , prvu tabuliranu vrednost rastojanja veću od d .

Dalje, ukoliko se frekvencija za koju se vrši proračun ne poklapa sa jednom od vrednosti 100 MHz, 600 MHz i 2000 MHz, potrebno je izvršiti interpolaciju:

$$E_o = E_{inf} + (E_{sup} - E_{inf}) \frac{\log(f / f_{inf})}{\log(f_{sup} / f_{inf})} \quad (4)$$

gde su: f_{inf} prva tabulirana vrednost frekvencije manje od f (100 MHz ako je $f < 600$ MHz, u ostalim slučajevima 600 MHz), f_{sup} prva tabulirana vrednost frekvencije veće od f (600 MHz ako je $f < 600$ MHz, u ostalim slučajevima 2000 MHz), E_{inf} očitana vrednost polja za f_{inf} i E_{sup} očitana vrednost polja za f_{sup} .

Kao što se može primetiti sa Sl.1, minimalna vrednost h_1 za koje su date vrednosti EM polja je 10 m. Vrednosti EM polja za visine između 0 m i 10 m nisu tabulirane i jednačina (2) se ne može koristiti za proračun nivoa EM polja. Za proračun nivoa EM polja za vrednosti h_1 u opsegu od 0 do 10 m koristi se sledeći izraz:

$$E[dB\mu V/m] = E_{zero} + 0.1h_1(E_{10} - E_{zero}) \quad (5)$$

gde su:

$$E_{zero}[dB\mu V/m] = E_{10} + 0.5(C_{1020} + C_{h1neg10}), \quad (5a)$$

$$C_{1020}[dB] = E_{10} + E_{20} \text{ dB} \quad (5b)$$

$C_{h1neg10}$ je korekcija C_{h1} u dB izračunata koršćenjem sledećeg izraza:

$$C_{h1} = 6.03 - J(v) \text{ dB} \quad (6)$$

gde je

$$J(v) = \left[6.9 + 20 \log \left(\sqrt{(v-0.1)^2 + 1} + v - 0.1 \right) \right], v > -0.7806 \quad (6a)$$

$$v = K_v \Theta_{eff}^2 \quad (6b)$$

$$\Theta_{eff}^2 = \arctan(-h_1 / 9000) \quad (6c)$$

a K_v konstanta koja ima sledeće vrednosti:

$$K_v = 1.35 \text{ za } 100 \text{ MHz,}$$

$$K_v = 3.31 \text{ za } 600 \text{ MHz,}$$

$$K_v = 6.00 \text{ za } 2000 \text{ MHz.}$$

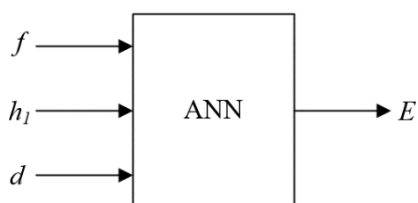
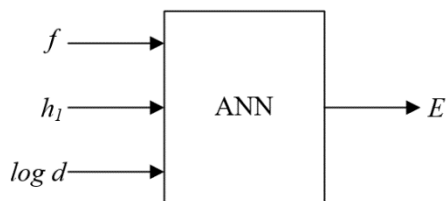
$E_{10} + E_{20}$ je jačina polja u $dB\mu V/m$ izračunata prema jednačini (2) za traženu daljinu d i visine $h_1 = 10$ m i $h_2 = 20$ m.

Preporuka ITU-R P.1546 se može koristiti za sisteme koji rade u opsegu od 30 MHz do 4000 MHz i gde visina h_1 ne prelazi 3000 m.

U realnim primerima se u najvećem broju slučajeva, sve tri veličine (parametar h_1 , rastojanje i frekvencija) razlikuju od tabuliranih vrednosti, pa je potrebno vršiti višestruke interpolacije, posebno ako je visina h_1 manja od 10 metara. U sledećoj sekciji je predložen efikasni metod zasnovan na primeni veštačkih neuronskih mreža koji omogućava određivanje EM polja za zadatu daljinu i vrednosti h_1 u opsegu $0 \leq h_1 \leq 10$ m.

III. PREDLOŽENI METOD

U ovom radu predložena su dva metoda za određivanje nivoa EM polja za visine h_1 manje od 10 metara primenom veštačkih neuronskih mreža. Na Sl. 2 prikazan je neuronski model kojim se na osnovu frekvencije f , visine h_1 i daljine d određuje nivo polja, odnosno koji modeluje zavisnost $E=f(f, h_1, d)$. Kako je na krivama za očekivani nivo polja u preporuci ITU-R P.1546 rastojanje prikazano na logaritamskoj skali razmatran je i model prikazan na Sl. 3, koji kao ulaze ima frekvenciju f , visinu h_1 i daljinu u d predstavljenu u logaritamskom formatu i nivo polja kao izlaz $E=f(f, h_1, \log d)$.

Sl. 2. Neuronski model za određivanje nivoa EM polja $E=f(f, h_1, d)$ Sl. 3. Neuronski model za određivanje nivoa EM polja sa $\log d$ na ulazu $E=f(f, h_1, \log d)$

Modeli predstavljaju višeslojne neuronske mreže, koje se sastoje od osnovnih jedinica, neurona, grupisanih u slojeve (ulazni sloj, jedan ili više skrivenih slojeva i izlazni sloj). Broj ulaznih neurona je određen brojem ulaznih parametara, u konkretnom slučaju tri, a broj izlaznih neurona odgovara broju izlaznih parametara, u konkretnom slučaju jedan. Broj neurona u skrivenim slojevima nije moguće unapred odrediti, već se taj broj određuje u postupku učenja mreže. Neuronska mreža uči zavisnost između ulazno-izlaznih parametara primenom optimizacionih procedura, kojima se vrši optimizacija parametara mreže (težine veza između neurona i pragovi aktivacionih funkcija neurona), sa ciljem da odziv mreže bude što je moguće bliži željenoj zavisnosti između ulazno-izlaznih parametara.

Uspješno obučena mreža sposobna je da da korektan odziv ne samo za kombinacije ulaznih veličina koje su korišćene tokom procesa učenja mreže, već i za bilo koje vrednosti ulaznih veličina koje nisu korišćene tokom učenja ali su u opsegu veličina u kome su i trening vrednosti. Treba napomenuti da je model razvijen za ceo skup frekvencija na koje se može primeniti preporuka ITU-R P.1546, tj. frekvencije u opsegu od 30 MHz od 4000MHz.

IV. REZULTATI

Podaci za obučavanje neuronskih mreža prikazanih na Sl.2 i Sl.3 se odnose na 40 različitih frekvencija u opsegu od 100 MHz do 4000 MHz i korakom frekvencije od 100 MHz. U cilju provere da li broj i distribucija trening uzoraka u pogledu izabranih vrednosti h_1 utiče bitno na tačnost mreže razmatrana su dva dva skupa podataka koji se odnose na $h_1=\{1, 3, 5, 7, 9 \text{ i } 10\}$ m (trening skup 1) i $h_1=\{1, 3, 6, 9, 10\}$ m (trening skup 2). Svi podaci potrebni za obučavanje i testiranje mreže generisani su korišćenjem izraza (3), (4), (5-5b) i (6-6c). Tokom razvoja modela, veći broj mreža sa jednim ulaznim slojem, dva skrivena sloja i jednim izlaznim slojem je obučeno i testirano. U skrivenom sloju, korišćen je različit broj neurona kako bi se pronašao model sa što boljom tačnošću.

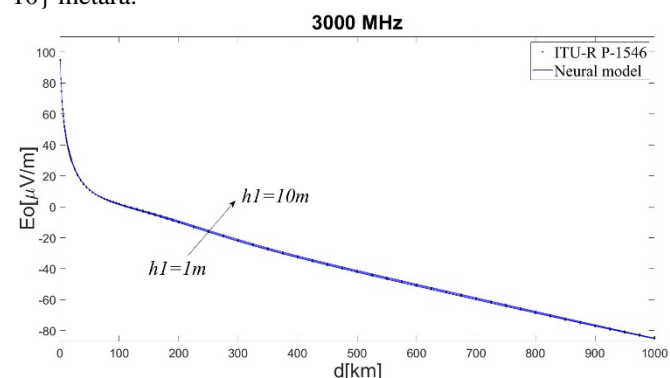
U ovom slučaju korišćene su neuronske mreže kod kojih skriveni neuroni imaju sigmoidnu transfer funkciju, a izlazni neuroni linearnu transfer funkciju. Ulazni neuroni imaju bafersku funkciju, pa je njihova funkcija jedinična linearna funkcija. Za obučavanje mreža primenjen je *Levenberg-*

Maquardt algoritam [2]. Tačnost odziva mreže testirana je poređenjem odziva mreže i referentnih vrednosti. Takođe, vođeno je računa da ne dođe do preučavanja mreže van referentnih tačaka, tj. da mreža ima dobru generalizaciju. Generalizacija se može proveravati testiranjem mreže za ulazne vrednosti koje nisu korišćene u toku učenja. Kako je u cilju što boljeg učenja mreže iskorišćen ceo skup referentnih podataka iz preporuke, provera da li je došlo do preučavanja vršena je vizuelno, tj. proverom odziva mreže kada su ulazne veličine menjane sa korakom koji je manji od koraka promene referentnih vrednosti kao i proračunom srednje greške (ATE - *Average Test Error*), maksimalne greške (WTE - *Worst Case Error*) i korelacionog koeficijenta r . Mreža je obučena i generisana u programskom paketu Matlab.

Nakon testiranja razvijenih modela, izabrani su najbolji modeli za oba predložena modela u slučaju obučavanja sa dva izabrana trening skupa. Za testiranje generalizacije korišćen je test skup koji se odnosi na vrednosti koje nisu korišćenje tokom obuke, a odnosi se na vrednosti frekvencije i visine koje su u opsegu veličina kao i vrednosti korišćene tokom obučavanja ($f=150\text{MHz}$, $h_1=2\text{m}$; $f=450\text{MHz}$, $h_1=4\text{m}$; $f=850\text{MHz}$, $h_1=6\text{m}$; $f=1450\text{MHz}$, $h_1=8\text{m}$; $f=1850\text{MHz}$, $h_1=2\text{m}$; $f=2350\text{MHz}$, $h_1=4\text{m}$; $f=3350\text{MHz}$, $h_1=6\text{m}$; $f=3850\text{MHz}$, $h_1=8\text{m}$).

Rezultati testiranja najboljih modela prikazani su u Tabeli I. Može se uočiti da su srednje greške u svim razmatranim slučajevima manje od 0.15%, dok je maksimalna greška manja od 1.5%. Korelacioni koeficijent je veoma blizu jedinici, što takođe potvrđuje visoku tačnost modelovanja.

Kao najbolji model za određivanje rastojanja za zadati nivo EM polja izabrana je mreža prikazana na Sl. 3 - $E=f(f, h_1, \log d)$, sa dva skrivena sloja (10 neurona u prvom sloju i 12 neurona u drugom sloju) i za koju su korišćeni podaci za obučavanje koji se odnose na visine $\{1, 3, 5, 7, 9, 10\}$ metara.



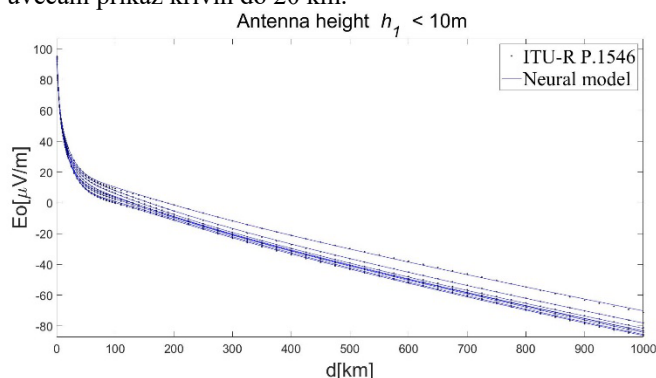
Sl. 4. Poređenje vrednosti EM polja generisanih pomoću razvijenog neuronskog modela i referentnih vrednosti iz preporuke ITU-R P1546.

Na Sl. 4 se može videti tačnost modela. Prikazane su krive za nivo polja generisane pomoću neuronske mreže (linije) za parametar visine $h_1=\{1, 3, 5, 7, 9, 10\}$ metara i referentne vrednosti određene preporukom (prikazane simbolima).

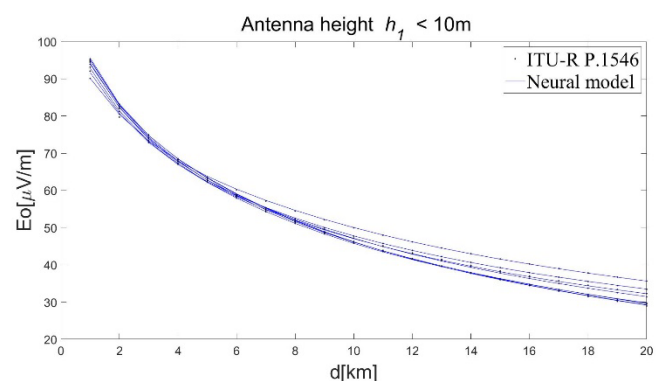
Može se uočiti da odziv mreže tj. vrednosti generisane pomoću neuronskog modela veoma dobro prate referentne vrednosti što potvrđuje da je postignuta zadovoljavajuća tačnost modelovanja.

Kao dodatna ilustracija tačnosti modela $E=f(f, h_1, \log d)$, na Sl. 5 prikazane su krive koje se odnose na test skup. Sa

Sl.5 se može primetiti da su vrednosti generisane pomoću neuronskog modela veoma blizu referentnim vrednostima prema preporuci ITU-R P1546. Kako bi se bolje prikazali rezultati krive za daljine do 20 km, na Sl. 6 se može videti uvećani prikaz krivih do 20 km.



Sl. 5. Poređenje vrednosti EM polja generisanih pomoću razvijenog neuronskog modela i referentnih vrednosti iz preporuke ITU-R P1546 za vrednosti koje nisu korišćene u obučavanju mreže



Sl. 6. Poređenje vrednosti EM polja generisanih pomoću razvijenog neuronskog modela i referentnih vrednosti iz preporuke ITU-R P1546 za vrednosti koje nisu korišćene u obučavanju mreže (daljina do 20 km)

TABELA I
TEST STATISTIKA ZA TRENING I TEST SKUP

	ATE[%]	WCE [%]	r
$E=f(f, h_1, d)$; trening skup 1 $h_1=\{1,3,5,7,9,10\}$ m			
treninig skup 1	0.10	1.47	0.999979
test skup	0.10	0.79	0.99998
$E=f(f, h_1, d)$; trening skup 2 $h_1=\{1,3,6,9,10\}$ m			
treninig skup 2	0.10	1.03	0.99998
test skup	0.11	0.89	0.999976
$E=f(f, h_1, \log d)$; trening skup 1 $h_1=\{1,3,5,7,9,10\}$ m			
treninig skup 1	0.11	1.39	0.999978
test skup	0.11	0.55	0.999981
$E=f(f, h_1, \log d)$; trening skup 2 $h_1=\{1,3,6,9,10\}$ m			
treninig skup 2	0.11	0.94	0.999982
test skup	0.14	0.65	0.999971

V. ZAKLJUČAK

Kao što se može videti u Sekciji II, ukoliko se određuje nivo EM polja za vrednosti parametara h_1 , f i d , potrebno je izvršiti veliki broj interpolacija. Predloženi metod baziran na neuronskoj mreži omogućava automatizaciju procesa interpolacija i trenutnog izračunavanja EM polja nalaženjem odziva neuronske mreže. Kako se svaka neuronska mreža može opisati pomoću skupa jednačina baziranih na linearnim

i eksponencijalnim funkcijama, izračunavanje EM polja pomoću razvijene neuronske mreže nije kompleksno, a može se vršiti u bilo kom programskom okruženju.

Prikazani metod određivanja EM polja može biti korišćen kao efikasan alat za određivanje zone pokrivanja predajnika korišćenjem statističke metode definisane preporukom ITU-R P.1546. Cilj budućih istraživanja je da se razvije neuronski model za inverzno očitavanje krivih za visine h_1 manje od 10 m.

ZAHVALNICA

Istraživanja prikazana u ovom radu podržana su od strane Ministarstva prosvete, nauke i tehnološkog razvoja.

LITERATURA

- [1] P.1546-5: Method for point-to-area predictions for terrestrial services in the frequency range 30 MHz to 3 000 MHz, ITU, 08/2019.
- [2] M.Radojković, Z. Marinković, A. Atanasković, "Inverzno očitavanje ITU-R P,1546 krivih za nivo EM polja radio-difuznih predajnika" 62. konferencija ETRAN, Palić, Jun. 2018.
- [3] M.Radojković, O. Pronić-Rančić, Z. Marinković, "Inverse Reading of ITU-R P.1546 Propagation Curves for the Broadcast Transmitter EM Field Level" iCEST 2020, pp. 220-223, 10-12 Sep. 2020.
- [4] Q. J. Zhang and K. C. Gupta, *Neural Networks for RF and Microwave Design*. Boston, MA: Artech House, 2000.
- [5] C. Christodoulou and M. Gerogiopoulos, *Applications of Neural Networks in Electromagnetics*, Artech House, Inc. Norwood, MA, USA, 2000.
- [6] Z. Stanković, N. Vasić, "Neural Approach in Modeling of the Propagation Curves from Recommendation ITU-R P.370-7", XLVII Konferencija za ETRAN, Herceg Novi, , pp.269-272, 8-13 jun 2003.
- [7] J. E. Rayas-Sanchez, "EM-based optimization of microwave circuits using artificial neural networks: The state-of-the-art," *IEEE Trans. Microw. Theory Tech.*, vol. 52, no. 1, pp. 420-435, Jan. 2004.
- [8] B. Milovanović, Z. Stanković, M. Ostojić, M. Miličić, "Predikcija nivoa elektromagnetnog polja korišćenjem neuronskog modela zasnovanog na ITU-R P.1546 preporuci", 51. konferencija ETRAN 2007, Herceg Novi - Igalo, Crna Gora, pp. MT1.3.1-4, 4-8. jun 2007.
- [9] H. Kabir, L. Zhang, M. Yu, P. Aaen, J. Wood, and Q. J. Zhang "Smart modelling of microwave devices", *IEEE Microw. Mag.*, vol. 11, pp.105-108, May 2010.
- [10] Z. Marinković, V. Marković, A. Caddemi, "Artificial Neural Networks in Small-Signal and Noise Modelling of Microwave Transistors," Chapter 6 in *Artificial Neural Networks*. Edited by Seoyun J. Kwon, Nova Science Publishers Inc., pp. 219-236, 2011.
- [11] Z. Marinković, T. Kim, V. Marković, M. Miličić, O. Pronić-Rančić, L. Vietzoreck, "Artificial Neural network based design of RF MEMS capacitive shunt switches", *Applied Computational Electromagnetics Society Journal*, vol. 31 no. 7, pp. 756-764, July 2016.

ABSTRACT

In this paper a method for determination of EM field level, according to ITU-R P.1546 recommendation for EM field level originated from broadcast transmitters with height h_1 less than 10 meters is proposed. Proposed method is based on the applications of artificial neural networks and enables efficient determination EM field level for frequencies up to 4000 MHz and height h_1 less than 10 meters. Accuracy of the method is illustrated by an example of curves related to several frequencies and h_1 not used for the training of neural network.

Automatization of calculation the EM field strength according to the ITU-R P.1546 method for height parameter h_1 smaller than 10 meters

Miloš Radojković, Zlatica Marinković

TLM modelovanje deformacija savijanja antene u biomedicinskim aplikacijama

Jugoslav Joković, *Member, IEEE*, Tijana Dimitrijević, *Member, IEEE*, Aleksandar Atanasković, *Member, IEEE*, and Nebojša Donšov, *Senior Member, IEEE*

Sadržaj — Prikazane su mogućnosti cilindričnog TLM numeričkog modela za analizu uticaja deformacije savijanja na parametre antene postavljene na ljudsko telo, koja se koristi u biomedicinskim aplikacijama. Kreiran je model pravougaone patch antene omotane oko dela cilindra koji može da se koristi za predstavljanje ljudskog tela (torzo, noga ili ruka) i istovremeno za modelovanje dielektričnih svojstava slojeva ljudskog tela. Ilustrovani su problemi u pogledu tačnosti i ograničenja kada se deformacija antene modeluje korišćenjem numeričkih metoda zasnovanih na pravougaonoj mreži. Prednosti cilindričnog TLM metoda kao tačne i efikasne alternative u odnosu na pravougaoni TLM pristup istaknute su kroz analizu uticaja deformacije savijanja na rezonantnu frekvenciju antene.

Ključne reči—Deformacije antene, tekstilne antene, TLM metod.

I. UVOD

Brojne tehnike rešavanja problema biomedicinskog inženjeringa (*Biomedical Engineering, BME*) našle su korisne primene u biologiji i medicini što je dovelo do razvoja mnogih naprednih BME uređaja, koji se generalno mogu klasifikovati kao uređaji za dijagnostiku ili tretman [1,2]. Jedna od ključnih komponenti mnogih BME uređaja je antena koja se može postaviti blizu, unutar ili na ljudskom telu [3] ili ugraditi u ljudsko telo direktno ili kroz kapsulu koja putuje kroz telo [4]. Postavljanjem antene na odeću ili direktno preko torza formira se bežični sistem za detekciju i komunikaciju za veze prenosa na telu ili van tela [5]. Tako postavljena jedna ili više antena koristi se npr. za dijagnostiku pomoću magnetne rezonantne slike (*Magnetic Resonance Imaging, MRI*) i mikrotalasne slike (*Microwave Imaging, MI*) [2,6] ili za lečenje hipertermijom [7]. Dizajn većine ovih antena suočava se sa fizičkim ograničenjima kao što su veličina, snaga i bezbednosna ograničenja, što sveukupno može uticati na efikasnost samog BME uređaja.

Za antene postavljene na različite delove ljudskog tela, bilo na ljudsku kožu ili odeću (npr. tekstilne antene), postoje i drugi izazovi u njihovom dizajnu, kao što je neposredna blizina ljudskog tela koja, zavisno od tipa antene, može dovesti do razdešavanja parametara antene, odnosno promene impedanse i smanjenja pojačanja i efikasnosti antene [8,9].

Jugoslav Joković, Tijana Dimitrijević, Aleksandar Atanasković, Nebojša Donšov – Elektronski fakultet, Univerzitet u Nišu, Aleksandra Medvedeva 14, 18000 Niš, Srbija (e-mail: jugoslav.jokovic@elfak.ni.ac.rs, tijana.dimitrijevic@elfak.ni.ac.rs, aleksandar.atanaskovic@elfak.ni.ac.rs, nebojsa.doncov@elfak.ni.ac.rs).

Takođe, promene držanja i pokreti ljudskog tela u svakodnevnim aktivnostima izazivaju brojne deformacije kao što su istezanje, uvijanje, savijanje, gužvanje ili češće kombinacija dve ili više ovih deformacija. Kao rezultat deformisane geometrije, mnogi parametri antene se takođe menjaju kao što su rezonantna frekvencija, pojačanje, dijagram zračenja i polarizacija [9].

U literaturi dominantno je razmatran uticaj deformacije cilindričnog savijanja na performanse uglavnom štampanih tekstilnih antena, kako numerički tako i eksperimentalno [10]. Takođe, treba uzeti u obzir da je ljudsko telo neplanarna struktura i da je za rad na različitim delovima tela potrebna antena različitih oblika. Da bi se odgovorilo na ove izazove, različite vrste anatomskih modela ljudskog tela ili njegovih delova se obično koriste u eksperimentalnim merenjima kako bi se uračunalo prisustvo telesnih tkiva. Mogu biti različite geometrijske složenosti uključujući jednoslojne i višeslojne strukture kao što je troslojni fantomski model (koža, masno tkivo, mišići) napravljen korišćenjem gelova i/ili tečnosti. Ipak, da bi se obezbedio potpuno konforman BME uređaj koji se može neprimetno i neinvazivno integrisati sa ljudskim telom koje karakterišu krivolinijske površine i dinamički pokreti, elektromagnetni (EM) kompjuterski alati za simulaciju igraju vitalnu ulogu u celokupnom dizajnu antene za BME aplikacije. Ovi alati, obično zasnovani na nekim od dostupnih diferencijalnih ili integralnih numeričkih tehnika punog talasa, kao što su FDTD [11], MoM [12], FEM [13], TLM [14], itd, treba da budu u stanju da precizno uzmu u obzir disperziju, gubitke i u nekim slučajevima anizotropna tkiva ljudskog tela. Istovremeno, trebalo bi da budu u stanju da precizno generišu geometrijske modele antena koje su ili deformisane usled držanja i kretanja odeće na telu ili su jednostavno konformne sa nekim zakrivljenim delovima ljudskog tela kao što su ruke i noge. Većina ovih alata je zasnovana na konstruktivnoj geometriji čvrstog materijala (npr. korišćenje *Boole*-ovih geometrijskih operacija) i diskretizaciji pravougaone mreže, odnosno modelovanog prostora, što znači da su u stanju da realizuju jednostavnije deformacije i/ili da koriste veoma finu stepeničastu aproksimaciju za predstavljanje takve deformisane geometrije antene odnosno geometriju antene koja prati krivolinijski oblik dela tela. U slučaju diferencijalnih numeričkih tehnika u vremenskom domenu ovaj pristup može dovesti do veoma malog vremenskog koraka i prekomernog vremena rada, a takođe u nekim slučajevima može proizvesti tzv. parazitne efekte koji su štetni za EM simulacije.

Kada EM problemi uključuju mnogo složenije geometrije, onda bi se upotreba tetraedarske mreže mogla pojaviti kao optimalnije rešenje. Kompjuterski grafički metodi (npr. *Green coordinates* [15]) nedavno su predloženi da bi se prevazišla ograničenja klasičnih komercijalnih EM alata zasnovanih na *Boole*-ovoj geometriji [16,17]. Ovi geometrijski generatori mogu omogućiti manipulaciju oblika antene pod proizvoljnom deformacijom u kombinaciji sa odgovarajućom numeričkom metodom i tetraedarskom mrežom da bi se minimizirale greške diskretizacije i predstavljaju moćan alat za konformni dizajn BME uređaja. Alternativa ovom naprednom rešenju u pogledu predstavljanja geometrije, ali i dalje skupom u pogledu memorije i vremena rada, može biti implementacija odabrane numeričke tehnike u koordinatnom sistemu koji je u skladu sa razmatranom deformisanom geometrijom antene. U slučaju savijanja antene, cilindrična diskretna mreža je savršeno prikladna da precizno opiše ovu deformaciju i da eliminiše greške diskretizacije koje dovode do mnogo brže i efikasnije simulacije u poređenju sa bilo kojom od pravougaonih ili tetraedarskih mreža. Pored toga, svaka promena ugla savijanja jednostavno se može implementirati u istoj cilindričnoj mreži omogućavajući da se isključi uticaj različitih veličina mreže (a samim tim i drugačije postavljenih napajanja i izlaznih tačaka zbog podešavanja mreže). Na taj način omogućena je konzistentna analiza uticaja različitih uglova savijanja antene na performanse.

U ovom radu, cilindrični TLM pristup je primenjen na modelovanje deformacije savijanja antene postavljene na ljudsko telo. Ilustrovane su prednosti ovog pristupa, koji istovremeno obezbeđuje precizno modelovanje geometrije antene i dielektričnih slojeva tela i efikasnu analizu efekta savijanja pod različitim uglovima, u odnosu na slučaj kada se koristi pravougaona TLM metoda. Postizanje tačnosti fizičkog modela antene omogućilo je analizu uticaja savijanja na performanse antene u prisustvu mišićnog tkiva. Objasnjeno je TLM metod sa kompaktnim modelom žice u cilindričnom koordinatnom sistemu kroz definisanje TLM žičanog čvora duž radijalnog pravca, koji je potreban za modelovanje koaksijalnog napajanja, kao i postupak modifikacije granica u radijalnom i ugaonom pravcu koji omogućava veću efikasnost simulatora u konkretnom slučaju. Glavna pitanja za realizaciju TLM modela antene odnose se na opis EM svojstava medijuma sa radijalno postavljenim slojevima zajedno sa proširenjem modelovane oblasti, pružajući mogućnost definisanja spoljnih granica u ugaonom i radijalnom pravcu. Simulirani rezultati dobijeni TLM modelima savijanja antene u prisustvu tkiva i numeričke analize dati su za različite uglove savijanja antene.

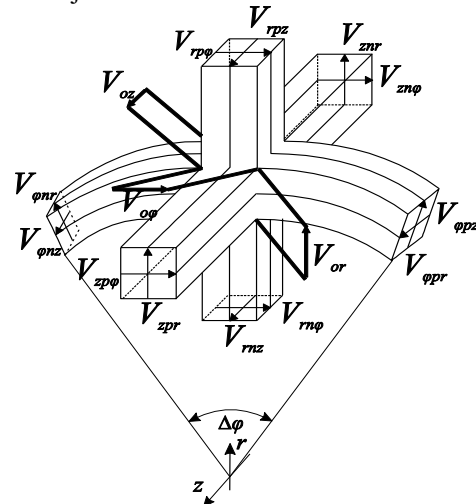
II. TLM METODOLOGIJA

TLM predstavlja numerički metod koji pripada grupi diferencijalnih metoda pogodnih za rešavanje EM problema u vremenskom domenu [14]. Zasnovan je na ekvivalencijama između Maksvelovih jednačina i prostiranja napona i struja duž vodova. Mreža međusobno povezanih čvorova koristi se za modelovanje prostiranja EM talasa uzimajući u obzir

diskontinuitete i interakciju sa različitim svojstvima materijala. Tradicionalno, TLM metod je razvijen u Dekartovom koordinatnom sistemu, ali za strukture koje sadrže samo kružne/cilindrične površine, pogodniji je i efikasniji TLM metod zasnovan na cilindričnoj mreži. Hibridni simetrični kondenzovani čvor (*Hybrid Symmetrical Condensed Node*, HSCN) koji predstavlja ćeliju u ortogonalnoj polarnoj mreži predstavljen je na Sl.1.a. Takva mreža ćelija se koristi za opisivanje EM osobina medijuma, preko odgovarajućih karakterističnih impedansi i admitansi povezanih vodova i stabova [18]. Iterativni postupak TLM algoritma sastoji se od dve glavne procedure poznate kao rasejanje i povezivanje [14]. Prilagođene su ortogonalnoj polarnoj mreži i dodatno modifikovane da bi se uzela u obzir pobuda, granice i nehomogena sredina i gubici [18,19].

Adaptacija i implementacija kompaktnog žičanog modela na cilindričnu mrežu [18] omogućila je modelovanje žičanih segmenata postavljenih duž radijalnog pravca. S obzirom da su za susedne čvorove razlikuju impedanse vodova i stabova ugrađenih u postojeću mrežu ćelija da bi se uzela u obzir žica, razvijen je i implementiran u postojeći softver baziran na TLM-u u cilindričnoj mreži dodatni postupak povezivanja za segmente žice u radijalnom pravcu [18, 19].

Pored relevantnog prikaza geometrije i EM svojstava nehomogenog medijuma, u slučaju takozvanih otvorenih problema kao što je *patch* antena, potrebno je dodati i odgovarajuće proširenje modelovane strukture, kako bi se uključila okoline antena. Primena cilindrične mreže je u ranijim radovima pretpostavljala da je okolina razmatrane strukture, koja čini modelovani prostor sa definisanim spoljnim granicama, potpuno cilindričnog oblika. Dakle, simulacije su zahtevale definisanje granica bez ikakvih graničnih uslova definisanih duž ugaonom pravca, gde je razmena impulsa obezbeđena povezivanjem poslednjeg i prvog čvora u ugaonom pravcu. Kada je ugao savijanja mali što se najčešće dešava u praksi prilikom razmatranja deformacija, modelovana *patch* antena je smeštena daleko od centra cilindričnog koordinatnog sistema, pa u tom slučaju upotreba celog cilindra kao modelovanog prostora koristi veliku memoriju i računarske resurse.



Sl. 1. Hibridni simetrični kondenzovani čvor (HSCN) u cilindričnoj mreži

Iz tog razloga, TLM algoritam je prilagođen da omogućiti postavljanje graničnih uslova duž ugaonih pravaca. Dodatna poboljšanja se postižu omogućavanjem mogućnosti definisanja graničnog stanja na unutrašnjoj površini modelovanog prostora duž radijalnog pravca, umesto definisanja centralnog čvora. Ortogonalna polarna mreža u tom slučaju je bazirana na diskretizaciji prostora predstavljenu unutar isečka cilindra.

Generalno, TLM metod omogućava da se opiše tri tipa granica: električni zid, magnetni zid i zid koji apsorbuje. U slučaju modelovanja antene, električni zid se koristi za modelovanje metalne podloge i zračće površine, dok su spoljašnje granice proširenog regiona opisane kao apsorbujuće sa koeficijentom refleksije voda na kraju prostora ρ_{ij} [22]:

$$\rho_{ij} = \frac{(1 + \rho_w) - \tilde{Z}_{ij}(1 - \rho_w)}{(1 + \rho_w) + \tilde{Z}_{ij}(1 - \rho_w)} \quad (1)$$

gdje je ρ_w koeficijent refleksije zida, a Z_{ij} je normalizovana impedansa odgovarajuće linije.

Kao rezultat definisanja modelovanog prostora kao dela cilindra zajedno sa graničnim uslovima, značajno je smanjen potreban broj TLM ćelija što dovodi do veće efikasnosti i uštede vremena i memorije. Prednosti ovog pristupa bile bi posebno uočljive u slučajevima kada je zakrivljenost odnosno savijanje mala, kada se zahteva veliki poluprečnik cilindrične površine, a samim tim i znatno veći broj ćelija ako se modelovana oblast predstavlja kao ceo cilindar. Dodatno, na ovaj način, uz dovoljno velike vrednosti poluprečnika cilindra u odnosu na dimenzije antene, moguće je modelovati pravougaone strukture u cilindričnoj mreži. Promenom samo poluprečnika cilindra moguće je kreirati modele sa različitim uglovima savijanja, koristeći mrežu iste rezolucije, i analizirati uticaj deformacije savijanja na performanse antene, nezavisno od drugih parametara modela koji se menjaju kada se primenjuje aproksimacija, kao što su površina zračće površine, debljina supstrata, položaj napajanja itd.

III. REZULTATI I ANALIZA

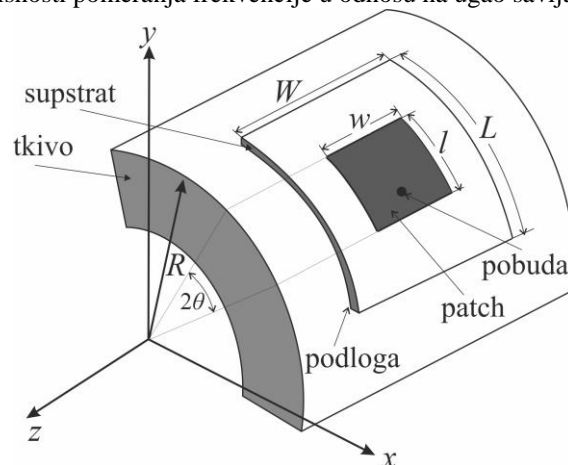
TLM solver je korišćen za analizu uticaja savijanja na performanse *patch* antene kada se postavi na ljudsko telo. U razmatranom slučaju, deo mišićnog tkiva se nalazi ispod antene. *Patch* antena dimenzija $w \times l = (50 \times 39.5) \text{mm}^2$, postavljena na podlogu i uzemljenu ravan dimenzija $W \times L = (100 \times 100) \text{mm}^2$ i savijena preko dela cilindra koji predstavlja mišićno tkivo, šematski je prikazana na Sl.2. Antena je realizovana na podlozi debljine $h = 2 \text{mm}$ sa supstratom relativne permitivnosti $\epsilon_r^s = 2.1$, dok je sloj mišićnog tkiva debljine $d = 35 \text{mm}$ predstavljen relativnom permitivnošću $\epsilon_r^m = 52.67 - j13$ [23]. U TLM modelu, zračeni *patch* i uzemljena ravan su predstavljeni kao savršeni električni provodnici, a antena se napaja preko koaksijalnog napajanja koji povezuje uzemljenu ravan i *patch*, što je opisano preko kompaktne žičanog modela. Položaj koaksijalne pobude je optimizovan za postizanje prilagođenja impedanse između generatora i antene, tako da se nalazi se na $l = 11.5 \text{mm}$ od ivice *patch-a*. Radna frekvencija dizajnirane antene iznosi $f = 2.45 \text{GHz}$.

Opisivanje problema sa odgovarajućom mrežom, u smislu veličine ćelije i sinhrinacije, veoma je važno kako bi se

obebedila konvergencija rezultata. Za razliku od stepeničaste aproksimacije koja se mora koristiti u pravougaonoj TLM mreži za opisivanje zakrivljenih granica, tačno modelovanje kružnih granica je jednostavno u cilindričnoj TLM mreži, sa dimenzijama ćelija određenim maksimalnom frekvencijom od interesa [14]. Kao rezultat, zakrivljene granice se mogu precizno modelovati pomoću cilindrične mreže bez obzira na rezoluciju mreže, dok pravougaona mreža mora biti dovoljno fina da bi se postigla bolja tačnost. Da bi se ovo dokazalo, razmatrani model antene je kreiran i korišćenjem pravougaonog TLM rešavača. Izvedene su simulacije za ravnu antenu, ali i za savijenu antenu da bi se ispitalo uticaj deformacije savijanja na rezonantnu frekvenciju antene. Razmatrana su dva ugla savijanja, $2\theta = 25$ i 50 stepeni. Simulirani rezultati, koji predstavljaju koeficijent refleksije, kada se veličina TLM ćelije od 1.0mm primeni za modelovanje antene, dobijeni cilindričnim i pravougaonim modelom, respektivno, prikazani su na Sl.3. i 4.

Kod modelovanja ravne antene može se uočiti slaganje rezultata dobijenih primenom cilindrične mreže rezolucije 1.0mm sa odgovarajućim rezultatima primene pravougaone mreže (crna linija na Sl. 3. i 4). Praktično, u slučaju modela antene u cilindričnoj mreži, ravna antena je modelovana primenom veoma malog ugla savijanja, $2\theta = 0.1$ stepen, što je ekvivalentno poluprečniku cilindra koji zadovoljava uslov da je mnogo veći od dimenzija antene $R \gg l$ (oko 500 puta), pa se može smatrati ravnom. Primenljivost cilindrične mreže na modelovane strukture bez zakrivljenosti potvrđena je dobijenom vrednošću rezonantne frekvencije od 2.444MHz , sa odstupanjem od 1% u odnosu na vrednost od 2.473MHz dobijenu primenom pravougaone mreže.

Sa druge strane, rezultati dobijeni pomoću cilindričnog TLM-a i pravougaonog TLM-a, sa veličinom ćelije od 1.0mm primenjenom za modelovanje antene, pokazuju značajnu razliku u pomeranju frekvencije usled savijanja antene postavljene na mišićno tkivo. Praktično, modelovanjem cilindričnim pristupom se može primetiti da veći ugao savijanja dovodi do pomeranja rezonantne frekvencije ka višim vrednostima, dok istovremeno rezultati modelovanja pravougaonom mrežom pokazuju smanjenje frekvencije u odnosu na ravan slučaj, zajedno sa nedoslednošću u pogledu zavisnosti pomeranja frekvencije u odnosu na ugao savijanja.



Sl.2. Pravougaona antena savijena preko dela tkiva

Nekonzistentnost rezultata dobijenih primenom pravougaonog modela može se objasniti činjenicom da pravougaona mreža rezolucije od 1.0mm model u slučaju savijene antene uvodi grubu aproksimaciju zakrivljene površine zračenja koja utiče na njenu rezonantnu frekvenciju. Shodno tome, neophodno je koristiti finiju mrežu koja bi smanjila grešku stepeničaste aproksimacije i obezbedila tačne rezultate. Da bi se ilustrovao uticaj rezolucije mreže pravougaoni TLM model antene je definisan mrežom veličine ćelije 0.1mm. Simulirana rezonantna frekvencija dobijena ovom pravougaonom mrežom, prikazana na Sl.5, pokazuje da se, sa povećanjem ugla savijanja, povećava i rezonantna frekvencija, slično kao što je slučaj kada se koristi cilindrična TLM mreža.

Dakle, kada se ista veličina ćelije koristi u pravougaonoj i cilindričnoj mreži (1.0mm) ponašanje rezonantne frekvencije je drugačije. Iz tog razloga, potrebna je finija pravougaona mreža (0.1mm) koja obezbeđuje konzistentnost rezultata u pogledu pomeranja frekvencije, slično onima koje daje cilindrična mreža (1.0mm). Parametri cilindrične TLM mreže – veličina ćelije i broj ćelija, prikazani su u Tabeli 1. Rezolucija mreže je podešena da ispuni zahteve vremenske sinhronizacije [14].

Prikazani rezultati dobijeni na osnovu mreže od 1.0mm potvrdili su da se cilindrični model može koristiti u analizi deformacija savijanja, dok pravougaona mreža te rezolucije nije adekvatna, odnosno da se zahteva finija rezolucija. Međutim, kada se koristi pravougaona mreža od 0.1mm koja obezbeđuje konvergenciju rezultata, povećanje broja ćelija iznosi oko 1000 puta, što dokazuje jake prednosti cilindrične mreže u ovom slučaju.

IV. ZAKLJUČAK

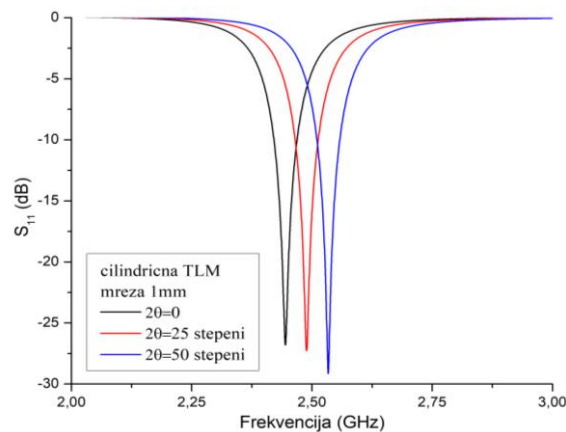
U ovom radu je TLM metod prilagođen ortogonalnoj polarnoj mreži korišćen za analizu deformacije savijanja *patch* antene postavljene na ljudsko telo - podešavanjem dimenzija modela, rezolucije mreže, odgovarajućeg proširenja regiona modelovanja i optimizacije položaja koaksijalnog napajanja, obezbeđeno je da efekat deformacije na parametre antene bude nezavisan od numeričkih grešaka.

Pristup je modifikovan kako bi se omogućilo korišćenje graničnih uslova duž radijalnog i ugaonog pravca koji dovode do značajnog smanjenja modelovane oblasti, a time i do smanjenja korišćenja memorije i vremena potrebnog za simulaciju. Prikazani rezultati pokazuju prednosti modela kreiranog u cilindričnoj TLM mreži, koja istovremeno obezbeđuje precizno modelovanje geometrije antene i dielektričnih svojstava supstrata i tkiva.

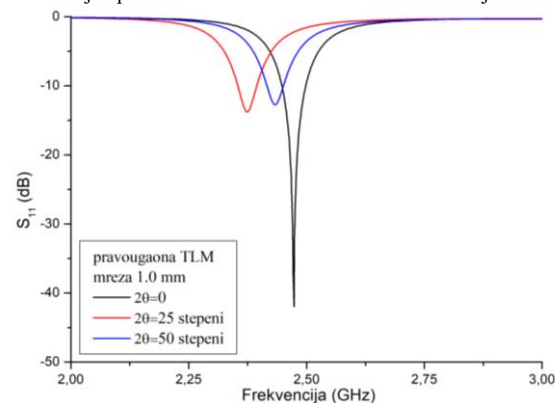
Prikazani numerički rezultati su pokazali da je TLM metod zasnovan na cilindričnoj mreži pogodniji i precizniji za modelovanje antene koja je deformisana savijanjem, u odnosu na pravougaoni TLM model. Glavne prednosti cilindričnog TLM metode su konformno modelovanje zakrivljenih površina, sa preciznošću koja se postiže manjim brojem ćelija, i dodatno fleksibilnost modelovanja realnog savijanja za različite uglove, bez promene parametara mreže.

TABELA I
PARAMETRI CILINDRIČNE MREŽE

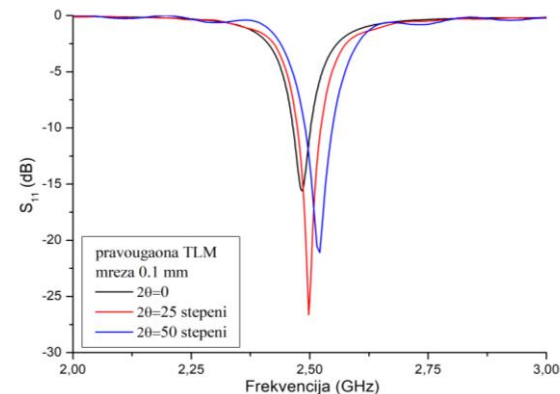
Osa	Medijum	Rezolucija	Broj ćvorova
r-	tkivo	~0.2 mm	205
	supstrat	1.0mm	
	vazduh	1.449 mm	
φ-	vazduh	1.449 / r (mm)	155
	supstrat	~1/ r (mm)	
	vazduh	1.449 / r (mm)	
z-	vazduh	1.449 mm	155
	supstrat	~1.0mm	
	vazduh	1.449 mm	



Sl.3. Zavisnost S_{11} parametra antene na mišićnom tkivu od ugla savijanja dobijen primenom cilindrične TLM mreže rezolucije 1.0mm



Sl.4. Zavisnost S_{11} parametra antene na mišićnom tkivu od ugla savijanja dobijen primenom pravougaone TLM mreže rezolucije 1.0mm



Sl.5. Zavisnost S_{11} parametra antene na mišićnom tkivu od ugla savijanja dobijen primenom pravougaone TLM mreže rezolucije 0.1mm

Mogućnosti definisanja različitih dielektričnih slojeva u radijalnom pravcu takođe omogućavaju precizno modelovanje antene omotane oko cilindra kako bi se oponašalo ljudsko tkivo predstavljeno u simulacijama kao standardni višeslojni model (koža, masno tkivo, mišićno tkivo i kosti). Iz navedenih razloga, TLM cilindrični solver se može efikasno koristiti za sprovođenje parametarske studije za karakterizaciju deformacije savijanja antene u režimu rada na telu koji se odnosi na promenu rezonantne frekvencije, širinu opsega i promenu tzv. povratnih gubitaka, odnosno S_{11} parametra.

ZAHVALNICA

Ovaj rad podržali su Ministarstvo prosvete, nauke i tehnološkog razvoja Republike Srbije (br. 451-03-9/2022-14/200102) i Fond za nauku Republike Srbije (br. 6394135).

LITERATURA

- [1] Enderle J., Bronzino J., *Introduction to Biomedical Engineering, Third Edition*, Academic Press, (2011)
- [2] Wang L., *Electromagnetic Waves and Antenas for Biomedical Applications*, IET (2021)
- [3] Kaur G., Kaur A., Kaur Toor G., Dhaliwal B.S., and Pattnaik S.S., "Antenas for Biomedical Applications", *Biomedical Engineering Letters* Vol. 5, No. 3, pp. 203-212, (2015)
- [4] Kiourti A., and Nikita K.S., "A Review of Implantable Patch Antenas for Biomedical Telemetry: Challenges and Solutions", *IEEE Antenas and Propagation Magazine*, Vol. 54, No. 3, pp. 210-228, (2012)
- [5] Yang H., and Liu X., "Wearable Dual-Band and Dual-Polarized Textile Antena for On- and Off-Body Communications", *IEEE Antenas and Wireless Propagation Letters*, Vol. 19, No. 12, pp. 2324-2328, (2020)
- [6] Solomakha G., Svejda J. T., Van Leeuwen C., Rennings A., Raaijmakers A. J., Glybovski S., and Erni D., "A self-matched leaky-wave antenna for ultrahigh-field magnetic resonance imaging with low specific absorption rate", *Nature Communications*, 12, 455 (2021)
- [7] Choi W.C., Lim S., Yoon Y.J., "Evaluation of Transmit-Array Lens Antena for Deep-Seated Hyperthermia Tumor Treatment", *IEEE Antenas and Wireless Propagation Letters*, Vol. 19, No. 5, pp. 866 – 870, (2020)
- [8] Rahman N.H.A., Yamada Y., and Nordin M.S.A., "Analysis on the Effects of the Human Body on the Performance of Electro-Textile Antenas for Wearable Monitoring and Tracking Application", *Materials*, 12, 1636, (2019)
- [9] Aun N.F.M., Soh P.J., Al-Hadi A.A., Jamlos M.F., Vandenbosch Guy A.E., and Schreurs D., "Revolutionizing wearables for 5G: 5G technologies: Recent developments and future perspectives for wearable devices and antenas", *IEEE Microwave Magazine*, IEEE, vol. 18, no. 3, pp. 108–124, (2017)
- [10] Song L., and Rahmat-Samii Y., "A Systematic Investigation of Rectangular Patch Antena Bending Effects for Wearable Applications", *IEEE Transactions on Antenas and Propagation*, vol. 66, no. 5, pp. 2219-2228, (2018)
- [11] K. S. Kunz and R. J. Luebbers, *The Finite Difference Time Domain Method for Electromagnetics*, CRC Press, Boca Raton, FL, (1993)
- [12] Gibson W.C., *The Method of Moments in Electromagnetics*, Chapman and Hall/CRC, (2021)
- [13] Thomas J.R. Hughes: *The Finite Element Method: Linear Static and Dynamic Finite Element Analysis*, Prentice-Hall (1987)
- [14] Christopoulos, C., *The Transmission-Line Modelling Method: TLM*, Institute of Electrical and Electronics Engineers, (1995)
- [15] Lipman Y., Levin D., and Cohen-Or D., "Green Coordinates", *ACM Trans. Graph.*, 27 (3), 1-10, (2008)
- [16] Sewell P., Benson T. M., Christopoulos C., Thomas D. W. P., Vukovic A., Wykes J. G., "Transmission-line modeling (TLM) based upon unstructured tetrahedral meshes", *IEEE Trans. Microw. Theory Tech.* 53(6), 1919-1928, (2005)
- [17] Altinozen E., Harrison I., Vukovic A., Sewel P.D., "Green Coordinates for Generation of Conformal Antena Geometries", *14th European Conference on Antenas and Propagation – EuCAP*, (2020)
- [18] Dimitrijević T., Joković J., Milovanović B. Doncov N., "TLM modeling of a probe-coupled cylindrical cavity based on compact wire model in the cylindrical mesh", *Int. J. RF Microw. Comput-Aided Eng.* 22(2) 184-192 (2012)
- [19] Jokovic J., Dimitrijevic T., Doncov N., "Efficient integral cylindrical transmission-line matrix modeling of a coaxially loaded probe-coupled cavity", *IET Microw. Antena & Propag.*, 9(8), 788-794, (2015)
- [20] Trenkic V., Wlodarczyk A.J., Scaramuzza R.A., "Modeling of coupling between transient electromagnetic field and complex wire structures", *Int. J. Numer. Model. Electron. Netw. Devices Fields.*, 12(4), 257-273, (1999)
- [21] Joković, J., Dimitrijević, T., Dončov, N., "Computational Analysis and Validation of the Cylindrical TLM Approach on IMCP Antenas", *Wireless Person. Comm.*, 106, 1573–1589, (2019)
- [22] Dimitrijevic T., Jokovic J., Doncov N., "Efficient Modeling of a Circular Patch-Ring Antena Using the Cylindrical TLM Approach", *IEEE Ant and Wireless Propag. Lett.*, 16, 2070-2073, (2017)
- [23] Chun-Xu Mao, Vital D., Werner D. H., Yuhao Wu, Bhardwaj S., "Dual-Polarized Embroidered Textile Armband Antena Array with Omnidirectional Radiation for On-/Off-Body Wearable Applications", *IEEE Trans. Ant. Prop.*, 68(4), 2575-2584, (2020).

ABSTRACT

The possibilities of the cylindrical TLM numerical model used for the analysis of the influence of bending deformation on the parameters of the antenna placed on the human body, which is used in biomedical applications, are presented. A model of a rectangular patch antenna wrapped around a part of a cylinder was created in order to represent the human body (torso, leg or arm) and at the same time to model the dielectric properties of the layers of the human body. The problems in terms of accuracy and limitations when antenna deformation is modeled using numerical methods based on a rectangular grid are illustrated. The advantages of the cylindrical TLM method as an accurate and efficient alternative in relation to the rectangular TLM approach are highlighted through the analysis of the influence of bending deformation on the resonant frequency of the antenna.

TLM modeling of antenna bending deformations in biomedical applications

Jugoslav Jokovic, Tijana Dimitrijevic, Aleksandar Atanaskovic and Nebojsa Doncov